# The 7th International Workshop on Chemical Exchange Saturation Transfer Imaging

# 第七届化学交换饱和转移成像国际专题研讨会



# PROCEEDINGS

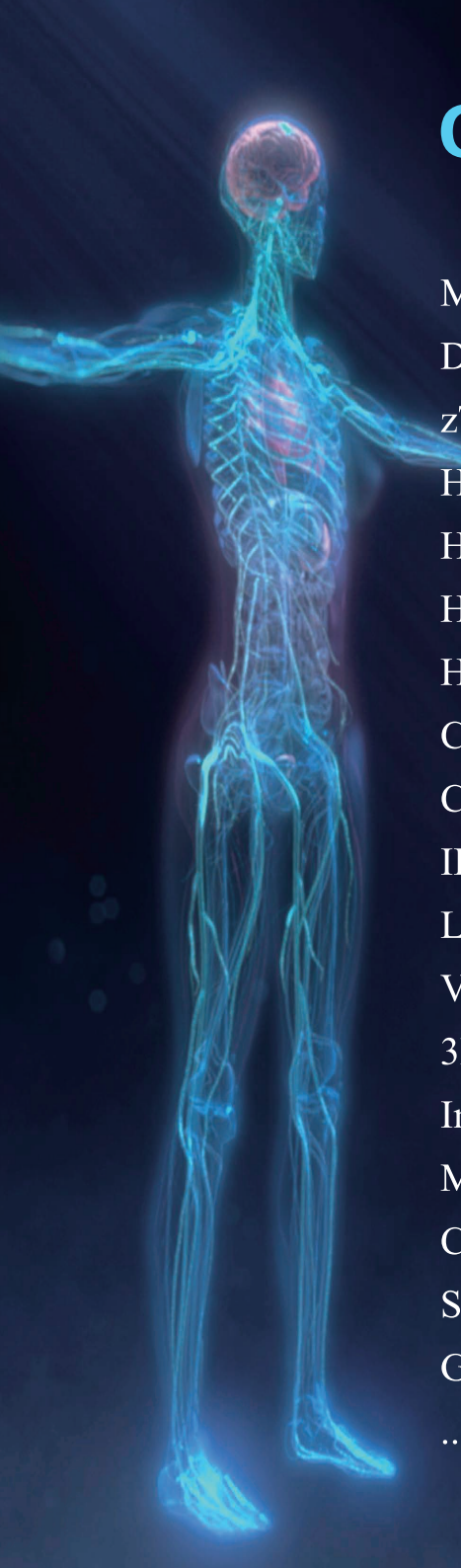
# 会议资料

November 12th–15th, 2018 Beijing, China

2018年11月12-15日 | 中国 • 北京

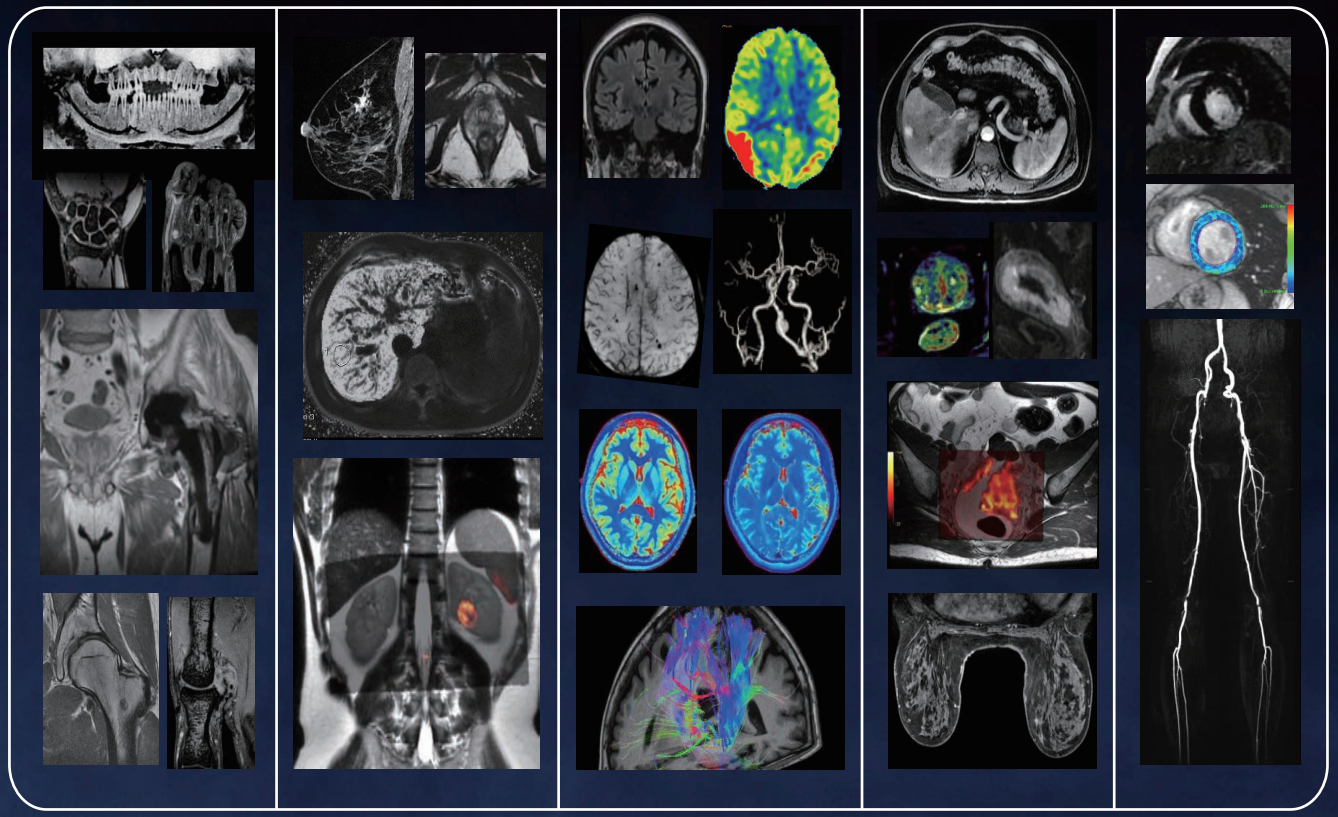
# GE医疗磁共振高端3.0T顶级临床科研平台

# SIGNA™ Works



- MAGiC
- DISCO
- zTE
- Hyper Focus
- Hyper Sense
- Hyper Cube
- Hyper band
- CUBE DIR
- Caridic mapping
- IDEAL IQ
- LAVA Flex
- Vibrant
- 3D ASL
- Inhance
- Mavric-SL
- Cartigram
- SWAN
- Gen IQ
- .....

| SIGNA Ortho Works 肌骨 | SIGNA Body Works 体部 | SIGNA Neuro Works 神经 | SIGNA Onco Works 肿瘤 | SIGNA CV Works 心血管 |
|---|---|---|---|---|

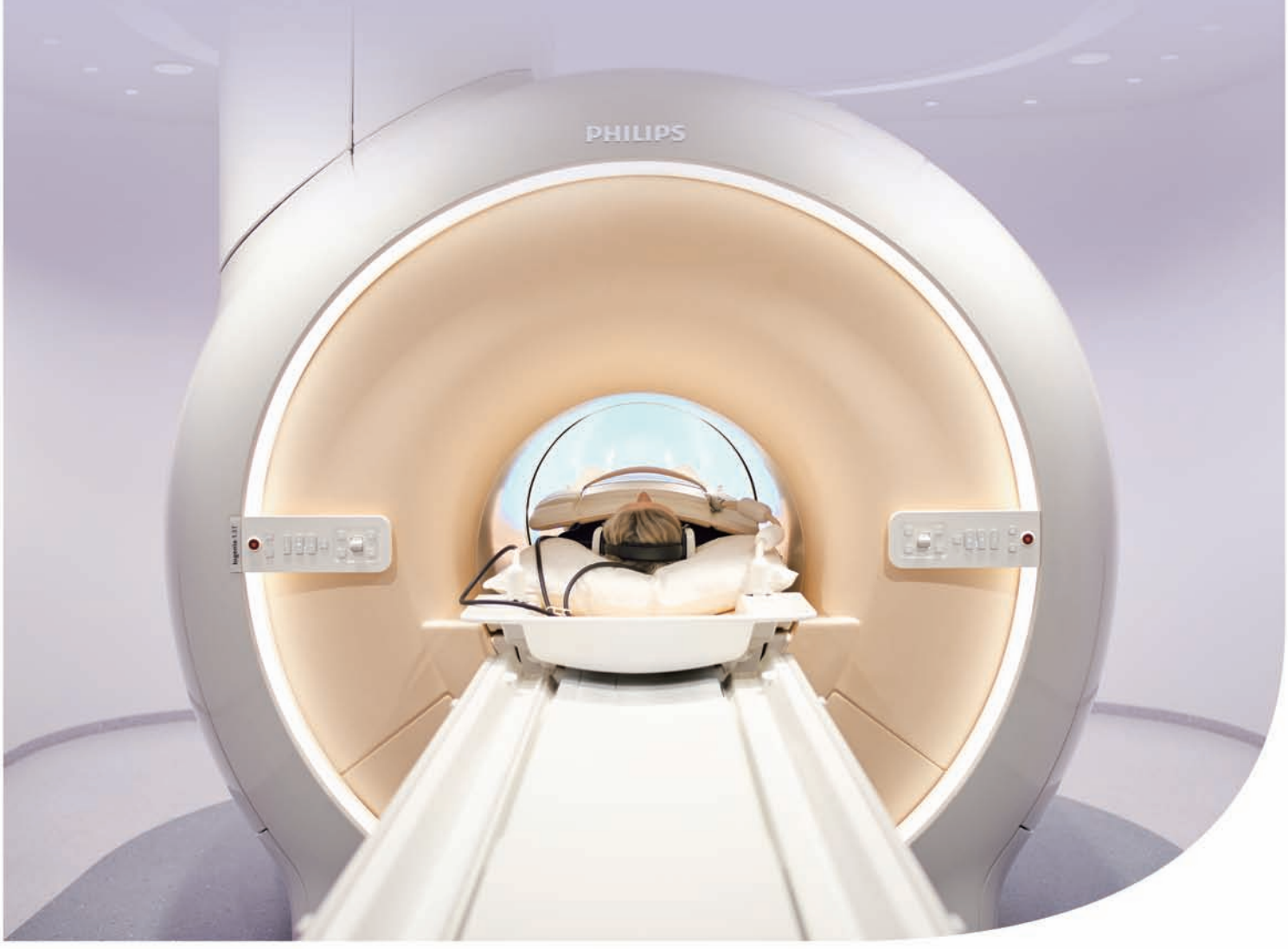


# Ingenia 3.0T CX磁共振

## 一款具备全身压缩感知成像的高端3.0T磁共振

- Smartselect和dstream线圈有助于提高图像质量
- T1 mapping心脏弛豫时间定量成像
- 多时相ASL动态动脉自旋标记成像
- 提供高分辨率冠状动脉成像

创新为你




医用磁共振成像系统Ingenia 3.0T CX

Philips Medical Systems Nederland B.V.
沪医械广审（文）第2018062174号　　国械注进20173285269
禁忌内容或注意事项详见说明书




# MAGNETOM Prisma
## 磁共振成像系统

MAGNETOM Prisma 3T 磁共振成像系统，可用于全身多部位磁共振检查。

- Prisma 高均匀3T磁体、80/200同时达到的梯度，可以帮助您在快速发展的3T科研领域始终处于前沿，在具挑战性的科研项目中更具优势。
- TimTX TrueShape 并行发射技术，选择性激发可以使ZOOMit 成像应用于特定的检查部位，提高图像质量。
- Prisma 可以显示解剖细节，揭示有价值的功能信息。根据您的科研需求，开发您自己的应用和序列。其始终如一的一致性和可重复性的结果将助力您的科研。

注：禁忌内容或者注意事项详见说明书。

MAGNETOM Prisma
磁共振成像系统
国食药监械（进）字 2014 第 3282943 号
生产厂商：Siemens Healthcare GmbH
沪医械广审（文）第 2018082873 号



SIEMENS Healthineers

# Welcome Message

Dear Esteemed Colleagues:

Welcome to Beijing CEST 2018-The 7th International Workshop on Chemical Exchange Saturation Transfer (CEST) imaging and the first one in this workshop series to be organized in Asia. CEST imaging is an important molecular MR imaging technique, originally proposed by Robert S. Balaban and his group at the National Institutes of Health (USA) in 2000. CEST imaging has been steadily advancing since then and rapidly expanding on many fronts in recent years.

The CEST Imaging workshop series started in 2010, and six workshops have been held at universities in USA and Europe: University of Torino, Italy (January 2010, 1st workshop), University of Texas at Dallas, USA (June 2011, 2nd workshop), Johns Hopkins University, USA (October CEST, October 2012, 3rd workshop ), University of Torino, Italy (May 2014, 4th workshop), University of Pennsylvania, USA (Penn-CEST, October 2015, 5th workshop), and Vanderbilt University, USA (Music City CEST, August 2017, 6th workshop). Beijing CEST 2018 will continue the tradition of presenting the latest developments in this exciting and rapidly advancing field.

Beijing CEST 2018 will focus on the technical development of CEST imaging and clinical applications in a broad spectrum of diseases. The goal is to bring together researchers from varying backgrounds and clinicians from related disciplines, and to provide a forum for communication among these multi-disciplinary groups. Additionally, this workshop will engage the Chinese and Asian community in CEST imaging studies to foster potential collaborations.

The workshop will feature a blend of invited scientific presentations, proffered papers, power-pitch poster presentations, and panel discussions on hot topics. The meeting will give everyone an opportunity to present and learn emerging clinical applications of CEST imaging. Young Investigator and International Travel Awards will be presented to students, post-doctoral fellows, and clinical residents who will be selected based on their abstract presentations.

On behalf of the organizing committee, we cordially invite you to Beijing to join us for this exciting learning opportunity!





## Basic Information

Venue:Jin Yun Ballroom, 2nd Floor, Capital Hotel, Beijing, China

Workshop check-in: November 12, Hotel Lobby, 1st Floor

November 13, Jin Yun Ballroom Lobby, 2nd Floor

Dates: November 13-15, 2018

Website: http://cest2018.medmeeting.org

## Organization

International Health Exchange and Cooperation Center, National Health Commission of P.R. China

In affiliation with
Peking Union Medical College Hospital, Beijing, China
Beijing Hospital
The Chinese Society of MRI, Chinese Society of Radiology

This workshop has been endorsed by the International Society for Magnetic Resonance in Medicine (ISMRM):

## CEST 2018 Secretariat

Contact Person:

Ms. Chunmei LI (Beijing Hospital)

Ms. Taylor XIN (International Health Exchange and Cooperation Center)

Tel: +86-10-88393883

Fax: +86-10-88393924

Email: cest2018@ihecc.org

# Organization

## Presidents

| | |
|---|---|
| Zhengyu Jin, MD | Peking Union Medical College Hospital, Beijing, China |
| Peter van Zijl, PhD | Johns Hopkins University, Baltimore, MD, USA |

## Executive Presidents

| | |
|---|---|
| Min Chen, MD, PhD | Beijing Hospital, Beijing, China |
| Jinyuan Zhou, PhD | Johns Hopkins University, Baltimore, MD, USA |

## Organizing Committee

| | |
|---|---|
| Silvio Aime, PhD | University of Torino, Torino, Italy |
| Nan Hong, MD | Peking University People's Hospital, Beijing, China |
| Alexej Jerschow, PhD | New York University, New York, NY, USA |
| Seong-Gi Kim, PhD | Sungkyunkwan University, Suwon, Korea |
| Linda Knutsson, PhD | Lund University, Lund, Sweden |
| Chunmei Li, MD | Beijing Hospital, Beijing, China |
| Marty Pagel, PhD | MD Anderson Cancer Center, Houston, TX, USA |
| Ravinder Reddy, PhD | University of Pennsylvania, Philadelphia, PA, USA |
| Dean Sherry, PhD | University of Texas Southwestern Medical Center, Dallas, TX, USA |
| Bin Song, MD | Huaxi Hospital, Chengdu, Sichuan, China |
| Wei Song, MD, PhD | Peking Union Medical College Hospital, Beijing, China |
| Phillip Zhe Sun, PhD | Emory University, Atlanta, GA, USA |
| Moriel Vandsburger, PhD | University of California at Berkeley, Berkeley, CA, USA |
| Elena Vinogradov, PhD | University of Texas Southwestern Medical Center, Dallas, TX, USA |
| Yining Wang, MD, PhD | Peking Union Medical College Hospital, Beijing, China |
| Yi-Xiang Wang, PhD | The Chinese University of Hong Kong, Hong Kong, China |
| Ed X. Wu, PhD | University of Hong Kong, Hong Kong, China |
| Huadan Xue, MD | Peking Union Medical College Hospital, Beijing, China |
| Fuhua Yan, MD, PhD | Ruijin Hospital, Shanghai, China |
| Yi Zhang, PhD | Zhejiang University, Hangzhou, China |

## Abstract Reviewers

Sung Soo Ahn, Kejia Cai, Kannie Chan, Christian Farrar, Rachel High, Shanshan Jiang, Tao Jin, Osamu Togao, Guanshu Liu, Dario Longo, Moriel Vandsburger, Elena Vinogradov, Xiang Xu, Moritz Zaiss, Yi Zhang, Zhengwei Zhou, Peter van Zijl, Zhongliang Zu

## Young Investigator Award Recipients

| | |
|---|---|
| Fabian Tobias Gutjahr | University of Würzburg |
| Jianpan Huang | City University of Hong Kong |
| Xunan Huang | Xidian University |
| Yue Lin | Beijing Hospital |
| Helen Sporkin | University of Virginia |
| Hao Yu | Zhujiang Hospital |
| Lu Yu | Beijing Hospital |
| Ferdinand Zimmermann | German Cancer Research Center (DKFZ) |

## International Travel Award Recipients

| | |
|---|---|
| Johannes Breitling | German Cancer Research Center (DKFZ) |
| Fabian Tobias Gutjahr | University of Würzburg |
| Or Perlman | Massachusetts General Hospital |
| Gizeaddis Simegn | University of Cape Town |
| Helen Sporkin | University of Virginia |
| Ferdinand Zimmermann | German Cancer Research Center (DKFZ) |

## The Beijing CEST 2018 are sponsored by

GE Healthcare
Philips Healthcare
Siemens Healthineers
Bayer Healthcare Company Limited

# Agenda

## Day 0 (November 12, 2018)

09:00-18:00 Workshop check-in (Hotel Lobby, 1st Floor)
18:00-21:00 Welcome Reception （Four Seasons, 1st Floor）

## Day 1 (November 13, 2018)

08:30 – 09:00 Welcome and introductory remarks
Chair: Min Chen

08:30 Welcome remarks
Zhengyu Jin, Peking Union Medical College Hospital, Beijing, China
08:35 Welcome remarks
Peter van Zijl, Johns Hopkins University, Baltimore, MD, USA
08:40 Introduction of Chinese Society of Radiology (CSR)
Zhengyu Jin, Peking Union Medical College Hospital, Beijing, China
08:50 Introduction of Beijing CEST 2018
Jinyuan Zhou, Johns Hopkins University, Baltimore, MD, USA

## SESSION I. Overview of CEST Imaging

09:00 – 10:30
Session Chairs: Marty Pagel, Fuhua Yan, Bin zhao

09:00 CEST basics: Understanding the Z-spectrum (Keynote)
Peter van Zijl, Johns Hopkins University, Baltimore, MD, USA
09:30 paraCEST agents: Opportunities and limitations (Keynote)
Dean Sherry, University of Texas Southwestern Medical Center, Dallas, TX, USA
10:00 CEST MRI analysis methods (Keynote)
Marty Pagel, MD Anderson Cancer Center, Houston, TX, USA

**10:30 GROUP PHOTO**
**10:45 COFFEE BREAK**

## SESSION II. Sugars and CEST

11:00 – 13:00
Session Chairs: Xavier Golay, Linda Knutsson, Qiyong Gong

11:00 CEST and spin-Lock MRI signals of glucose and glucose analogs
Tao Jin, University of Pittsburgh, Pittsburgh, PA, USA
11:23 Dynamic glucose enhanced MRI in animals and humans
Xiang Xu, Johns Hopkins University, Baltimore, MD, USA
11:45 GlucoCEST of glucose analogs
Gil Navon, Tel Aviv University, Tel Aviv, Israel
12:08 Glucose-enhanced MRI: Applications in humans
Daniel Paech, German Cancer Research Center, Heidelberg, Germany
12:30 Will GlucoCEST MRI be able to visualize cancer in humans? (Keynote)
Xavier Golay, University College London, London, United Kingdom

**13:00 – 14:00 LUNCH**

13:00 – 14:00 Satellite Meetings
13:00 Philips Healthcare
13:30 GE Healthcare

## SESSION III. POWER PITCH SESSION I

14:00 – 16:00
Session Chairs: Yi Zhang, Zhongliang Zu

14:00 Power pitches
14:00 Reproducibility study of CEST MRI using real-time motion and shim navigated CEST sequence Gizeaddis Simegn, University of Cape Town, Cape Town, South Africa
14:04 Creatine and phosphocreatine mapping of mouse skeletal muscle by a polynomial and Lorentzian line-shape fitting CEST method
Lin Chen, F.M. Kirby Research Center for Functional Brain Imaging, Kennedy Krieger Research Institute, Baltimore, MD, United States
14:08 In vivo proton exchange rate of healthy human brains quantified with omega plot
Mehran Shaghaghi, University of Illinois at Chicago, Chicago, IL, United States
14:12 Optimized dualCEST-MRI for imaging of endogenous bulk mobile proteins in the human brain
Johannes Breitling, German Cancer Research Center (DKFZ), Heidelberg, Germany
14:16 Improved Fat-Water Separation Using Multipeak Reconstruction for Suppression of Lipid Artifacts in Chemical Exchange Saturation Transfer (CEST) Imaging
Yu Zhao, East China Normal University, Shanghai, China
14:20 FullHD CEST imaging in the human brain at 7T
Jan-Eric Meissner, German Cancer Research Center (DKFZ), Heidelberg, Germany
14:24 Comparison of Different CEST Metrics for Brain Tumor Grading
Ruibin Liu, Zhejiang University, Hangzhou, Zhejiang, China
14:28 Chemical Exchange Saturation Transfer (CEST) Imaging of Phosphocreatine in the Muscle at 15.2T
Julius Chung, Center for Neuroscience Imaging Research, Suwon, Korea
14:32 Proton Exchange Rate, Volume Fraction, T1, and T2 MR Fingerprinting using an Optimized Acquisition Schedule and a Deep RecOnstruction NEtwork (DRONE)
Or Perlman, Massachusetts General Hospital and Harvard Medical School, Charlestown, MA, United States
14:36 Ultrafast multi-slice Chemical Exchange Saturation Transfer Imaging
Jizhou Cai, Xiamen University, Xiamen, Fujian, China
14:40 Multicolor metabolic quantitative CEST (mmqCEST): high resolution imaging of brain metabolites
Vitaliy Khlebnikov, University Medical Center Utrecht, Utrecht, the Netherlands
14:44 Temperature mapping of fat tissues by Z-Spectrum Imaging
Alessandro Scotti, University of Illinois at Chicago, Chicago, IL, United States
14:48 Monitoring the Degradation of Implanted Hydrogels using CEST MRI
Wei Zhu, Johns Hopkins University, Baltimore, MD, United States
14:52 CEST MRI of brain inflammation using an aspirin metabolite as contrast agent
Xiaolei Song, Johns Hopkins University, Baltimore, MD, United States
14:56 Acidosis imaging of skeletal muscles by chemical exchange saturation transfer (CEST) imaging
Dennis Hwang, Academia Sincia, Taipei, Chinese Taipei
15:00 Combining GlucoCEST and pH imaging for an improved characterization of tumor metabolism
Dario Longo, University of Torino, Torino, Italy

**15:04 Poster presentation & Coffee**

## SESSION IV. CEST in Neurology

16:00 – 18:00
Session Chairs: Ravinder Reddy, Moritz Zaiss, Wanshi Zhang

16:00 GluCEST MRI and glutamatergic system dysregulation (Keynote)
Ravinder Reddy, University of Pennsylvania, Philadelphia, PA, USA
16:30 Machine learning with protein-based MRI for predicting IDH1/2 mutation status in diffuse gliomas
Shanshan Jiang, Johns Hopkins University, Baltimore, MD, USA
16:53 CEST imaging of Parkinson's disease
Chunmei Li, Beijing Hospital, Beijing, China
17:15 CrCEST in the study of creatine metabolism kinetics in Peripheral Arterial Disease (Proffered paper)
Helen Sporkin, University of Virginia, Charlottesville, Virginia, USA
17:38 Dynamic glucose-enhanced imaging of mouse brain with Alzheimer's disease at 3T MRI (Proffered paper)
Jianpan Huang, City University of Hong Kong, Hong Kong, China

**18:00 – 20:00 DINNER（Zi Yun Grand Ballroom, 2nd Floor）**

## Day 2 (November 14, 2018)

08:15 – 08:30 Award Announcement
Zhengyu Jin, Min Chen, Dairong Cao, Jingliang Cheng, Wen Shen, Meiyun Wang, Yongqiang Yu

## SESSION V. CEST in Oncology

08:30 – 10:30
Session Chairs: Osamu Togao, Zhibo Wen, Xuening Zhang

08:30 APTw imaging in cancer clinical practice
Osamu Togao, Kyushu University, Fukuoka, Japan
08:50 Predicting response to antiangiogenic treatment for recurrent GBM using APTw MR imaging: Initial experience
Zhibo Wen, Zhujiang Hospital, Guangzhou, China
09:10 APTw imaging of brain tumors: Added value
Sung Soo Ahn, Yonsei University College of Medicine, Seoul, Korea
09:30 NOE(-1.6ppm) imaging in brain tumor
Zhongliang Zu, Vanderbilt University, Nashville, TN, USA
09:50 APTw MRI for predicting histological grade of hepatocellular carcinoma: Comparison with diffusion-weighted imaging (Proffered paper)
Yue Lin, Beijing Hospital, Beijing, China
10:10 Z-spectral modeling for CEST-MRI of bladder cancer (Proffered paper)
Xunan Huang, Xidian University, Xi'an, Shannxi, China

**10:30 COFFEE BREAK**

## SESSION VI. Responsive CEST contrast agents

10:50 – 13:00
Session Chairs: Silvio Aime, Jeff Bulte, Huadan Xue

10:50 Lipo-/cell-CEST: Enhanced sensitivity for new applications (Keynote)
Silvio Aime, University of Torino, Torino, Italy
11:20 Highly sensitive CEST MR molecular imaging using natural dextrans
Guanshu Liu, Johns Hopkins University, Baltimore, MD, USA
11:40 Evaluations of tumor models with acidoCEST MRI
Rachel High, University of Arizona, Tucson, AZ, USA, USA
12:00 CEST imaging of hydrogel-based therapy
Kannie Chan, City University of Hong Kong, Hong Kong, China
12:20 Hyper-CEST for molecular imaging and lung MRI
Xin Zhou, Wuhan Institute of Physics and Mathematics, Chinese Academy of Sciences, Wuhan, Hubei, China
12:40 A positive contrast chemical exchange experiment using refocused acquisition of chemical exchange transferred excitation (RACETE) (Proffered paper)
Fabian Tobias Gutjahr, University of Würzburg, Würzburg, Germany

13:00 – 14:00 LUNCH
13:00 – 14:00 Satellite Meetings
13:00 Siemens Healthineers
13:30 Bayer Healthcare Company Limited

## SESSION VII. POWER-PITCH SESSION II

14:00 – 16:00
Session Chairs: Kejia Cai, Shanshan Jiang

**14:00 Power pitches**
14:00 APT weighted MRI as an effective imaging protocol to predict clinical outcome after acute ischemic stroke
Guisen Lin, Medical College of Shantou University, Shantou, Guangdong, China
14:04 Progressive Registration for Dynamic Salicylate Enhancement (DSE) Image in Chemical Exchange Saturation Transfer (CEST) MRI
Chongxue Bie, Northwest University, Xi'an, Shannxi, China
14:08 Quantitative assessment of CEST effect using a Gaussian-Lorentzian hybrid algorithm (GLHA) for Z spectra-fitting
Lihong Zhang, Northwest University, Xi'an, Shannxi, China
14:12 Development of Myo-Inositol and Lactate Chemical Exchange Saturation Transfer (MILAC-CEST) MRI for Glioma Grading
Laurie J. Rich, University of Pennsylvania, Philadelphia, PA, United States
14:16 Assessing Response to Therapy Using Simultaneous PET/MRI in Preclinical Model of Pancreatic Cancer
Joshua M. Goldenberg, UT MD Anderson Cancer Center, Houston, TX, United States
14:20 CEST MRI as new imaging biomarker for acute kidney injury
Jing Liu, Guizhou Medical University, Guiyang, Guizhou, China

14:24 Studies of Chemical Exchange Saturation Transfer on 1.5 T Clinical MRI Scanner
Yonggui Yang, The Second Affiliated Hospital of Xiamen Medical College, Xiamen, Fujian, China

14:28 Amide proton transfer imaging in amyotrophic lateral sclerosis patients
Zhuozhi Dai, Medical College of Shantou University, Shantou, Guangdong, China

14:32 Amide Proton Transfer-Weighted MRI Signal as a Surrogate Biomarker of Ischemic Stroke Recovery in Patients with Supportive Treatment
Lu Yu, Beijing Hospital, Beijing, China

14:36 Chemical Exchange Saturation Transfer MR Imaging of Malignant and Benign Head and Neck Tumors at 3.0T
Lu Yu, Beijing Hospital, Beijing, China

14:40 Artifacts in dynamic CEST MRI due to motion and field shifts
Moritz Zaiss, Max-Planck Institute of biological cybernetics, Tübingen, Germany

14:44 Investigation of Anterior Cingulate Cortex APT values in patients with obsessive-compulsive disorder
Yan Li, Ruijin Hospital, Shanghai Jiao Tong University School of Medicine, Shanghai, China

14:48 Prediction Grades and association with Ki-67 proliferation status in meningioma using Amide proton transfer-weighted MRI
Hao Yu, Zhujiang Hospital of Southern Medical University, Guangzhou, Guangdong, China

14:52 The Histogram Analysis of Amide Proton Transfer-Weighted (APTw) Imaging for Differential Diagnosis of Prostate Cancer
Yue Lin, Beijing Hospital, National Center of Gerontology, Beijing, China

14:56 Amide Proton Transfer Imaging of the Recurrent Malignant Gliomas: Possible Feasibility Assessing Chemotherapy Response
Qihong Rui, Zhujiang Hospital of Southern Medical University, Guangzhou, Guangdong, China

**15:00 Poster presentation & Coffee**

## SESSION VIII. CEST Standardization

16:00 – 18:00
Session Chairs: Peter van Zijl, Dean Sherry, Jinyuan Zhou

16:00 An overview of CEST sequences on GE MR platform
Bing Wu, GE Healthcare, Waukesha, USA

16:30 A review on APTw pulse sequences and experimental results on Philips MRI scanners
Jochen Keupp, Philips Research Europe, Hamburg, Germany

17:00 A review on CEST pulse sequences and experimental results on Siemens MRI scanners
Yi Zhang, Zhejiang University, Hangzhou, China

17:30 Clinical APTw MRI at 3T: Technique review and recommendations
Jinyuan Zhou, Johns Hopkins University, Baltimore, MD, USA

## Day 3 (November 15, 2018)

### SESSION IX. Novel CEST Applications

08:30 – 10:30
Session Chairs: Moriel Vandsburger, Yi-Xiang Wang, Yining Wang

08:30 Addressing the unmet needs of non-ischemic heart disease patients using cardiac CEST as an all-in-one tool
Moriel Vandsburger, University of California at Berkeley, Berkeley, CA, USA
08:50 CEST imaging of liver and intervertebral disc: looking into the future
Yi-Xiang Wang, The Chinese University of Hong Kong, Hong Kong, China
09:10 Using pH and perfusion imaging to detect progression in renal disease
Mike McMahon, Johns Hopkins University, Baltimore, MD, USA
09:30 Functional renal imaging with MRI-CEST
Dario Longo, University of Torino, Torino, Italy
09:50 Recent advances in the study of non-invasive MR pH imaging using chemical exchange
Renhua Wu, Shantou University, Guangdong, China
10:10 Furin-mediated intracellular self-assembly of olsalazine nanoparticles enhances MR imaging and tumor therapy (Proffered paper)
Yue Yuan, Johns Hopkins University, Baltimore, MD, USA

**10:30 COFFEE BREAK**

### SESSION X. Novel CEST Methods

11:00 – 13:00
Session Chairs: Christian Farrar, Hye-Young Heo, Phillip Zhe Sun

11:00 Clinical CEST MRI studies at ultra-high $B_0$ field (7T and 9.4T)
Moritz Zaiss, Max Planck Institute for Biological Cybernetics, Tubingen, Germany
11:20 Rapid and quantitative CEST imaging with MR fingerprinting
Christian Farrar, Massachusetts General Hospital, Charlestown, MA, USA
11:40 CEST MR Fingerprinting by subgrouping proton exchange models
Hye-Young Heo, Johns Hopkins University, Baltimore, MD, USA
12:00 Quantitative tissue pH MRI in an experimental model of acute ischemic stroke
Phillip Zhe Sun, Emory University, Atlanta, GA, USA
12:20 Fat corrected APT-CEST in the human breast (Proffered paper)
Ferdinand Zimmermann, German Cancer Research Center, Heidelberg, Germany

### 12:40 – 12:45 Closing remarks

**12:45 – 13:30 LUNCH**

# CEST basics; Understanding the Z-spectrum

Peter C. M. van Zijl[1,2*]
[1] *Russell H. Morgan Department of Radiology and Radiological Science, The Johns Hopkins University School of Medicine, Baltimore, MD, USA*
[2] *F.M. Kirby Research Center for Functional Brain Imaging, Kennedy Krieger Institute, Baltimore, MD, USA*

Chemical Exchange Saturation Transfer (CEST) combines principles of MR spectroscopy (MRS, specificity for low concentration metabolites) and MRI (imaging of water protons with high sensitivity). It is based on magnetization transfer, exploiting the interaction of the exchangeable protons of these metabolites with the water protons to achieve large sensitivity enhancements (several orders of magnitude). This then allows the imaging of molecular information with MRI sensitivity. This information is generally obtained by measuring the water signal saturation as a function of frequency in the proton spectrum, which generates a so-called Z-spectrum.

An introduction of the basic principles of CEST MRI and Z-spectroscopy will be given. However, in order to get insight into the type of molecules that can be studied and the specificity of detection, it is important to realize that, in addition to the exchange-based saturation transfer process of metabolites (CEST), many other types magnetization transfer effects contribute to the in vivo Z-spectrum. These are effects from (i) direct water saturation, (ii) semi-solid protons (conventional magnetization transfer contrast or MTC), and (iii) relayed nuclear Overhauser enhancements (rNOEs) in mobile macromolecules, e.g. proteins and peptides and lipids. To make matters worse, the relative contributions of these four major components depends on the magnetic field strength (B0) and pulse sequence parameters such as B1 strength, pulse shape and length, and interpulse delay. This presents a major problem for quantification and reproducibility of MTC and CEST effects and often leads to confusion and contradiction in the interpretation of results. On the other hand, this provides an opportunity to separate out some overlapping signals.

The use of higher B0 can provide higher detection sensitivity (signal-to-noise ratio, SNR), with both MTC and CEST studies benefitting from longer water T1. Compared to MRI, CEST imaging provides an increase in chemical specificity, but contrary to MRS, exchange-effected saturation line shapes are measured, which are inherently broad. However, CEST specificity is expected to increase at higher B0 because of a larger chemical shift dispersion of the resonances of interest (similar to MRS). In addition, shifting to a slower exchange regime at higher B0 facilitates improved detection of for instance the guanidinium protons of creatine. Unfortunately, the very fast exchanging amine protons in glutamate and the hydroxyl protons in myoinositol, glycogen, and glucosaminoglycans are still coalesced with the water signal at tissue pH. Some examples will be used to illustrate the different magnetization transfer contributions and how to increase specificity.

**References (some recent reviews):**

1) van Zijl PCM, Lam WW, Xu J, Knutsson L, Stanisz GJ. Magnetization Transfer Contrast and Chemical Exchange Saturation Transfer MRI. Features and analysis of the field-dependent saturation spectrum. 2018 Mar;168:222-241.
2) van Zijl PC, Sehgal AA. Proton Chemical Exchange Saturation Transfer (CEST) MRS and MRI. eMagRes, 2016, Vol 5: 1307–1332. DOI 10.1002/9780470034590.emrstm1482
3) van Zijl PC, Yadav NN. Chemical exchange saturation transfer (CEST): what is in a name and what isn't? Magn Reson Med. 2011 Apr;65(4):927-48
4) Knutsson L, Xu J, Ahlgren A, van Zijl PCM. CEST, ASL, and magnetization transfer contrast: How similar pulse sequences detect different phenomena. Magn Reson Med. 2018 Oct;80(4):1320-1340.

**Acknowledgements:** NIH Grants P41EB015909, RO1EB019934 and RO1015032 provide financial support

## paraCEST agents: Opportunities and limitations

A. Dean Sherry, PhD

*Advanced Imaging Research Center, University of Texas Southwestern Medical Center, Dallas, Texas, USA.*
*Department of Chemistry, University of Texas at Dallas, Richardson, Texas, USA.* [5]*Vitalquan*
*Department of Radiology, University of Texas Southwestern Medical Center, Dallas, Texas, USA.*

The idea of using a paramagnetic lanthanide ion complex as a CEST agent evolved from years of study of the chemical properties of gadolinium complexes as MRI contrast agents. One of the key features of $Gd^{3+}$ chemistry was learning how to optimize water exchange rates so when it was discovered that converting a single carboxyl group in DOTA to an amide dramatically slowed water exchange in the LnDOTA-type complexes,[1,2] this led to the discovery that water exchange in EuDOTA-tetraamides is so slow that a separate $^1$H NMR signal can be seen for a single water molecule bound to the inner-sphere of $Eu^{3+}$ and the first report of a paraCEST agent.[3] In the intervening years, many new paraCEST agents have been reported that respond to changes in pH, temperature, various enzyme activities, the presence of biologically important metal ions, tissue redox, and metabolites such as glucose and lactate. This demonstrates that unlike Gd-based agents, it is relatively easy to create responsive paraCEST agents. Yet, despite these many successes, only a few paraCEST agents have been applied *in vivo*. Why is this? Where are the limitations? One concern of course is that they must be injected so will require substantial safety testing and regulatory approval. This presents a huge barrier for academic or small company-based scientists even if a paraCEST agent is discovered that adds valuable new clinical information about a disease that cannot be obtained otherwise. A second limitation is that most papers on new paraCEST agents report CEST properties *in vitro* but rarely *in vivo*. This likely reflects limited access to preclinical imaging by many scientists but this lack of testing *in vivo* ultimately becomes a limitation for the entire field. Without even preliminary testing *in vivo*, our understanding of how these agents perform *in vivo* will always be limited. Like other types of MRI contrast agents, CEST contrast from both endogenous and exogenous molecules depends upon concentration, proton exchange rates, and the relaxation rate of tissue water protons so there are many reasons to remain optimistic about paraCEST agents, especially at higher imaging fields. CEST is governed by the exchange condition, $k_{ex} < \Delta\omega$, so if $\Delta\omega$ is large, then faster exchanging systems can be used to initiate CEST contrast. This is a substantial advantage of paraCEST over diaCEST agents. It is relatively easy to modify $\Delta\omega$ in paramagnetic complexes but manipulating $k_{ex}$ is generally more difficult. This is especially problematical *in vivo* where a multitude of other exchanging proton species can significantly impact the intensity of the paraCEST signal itself. Once these limitations are well-understood, agent structures can be modified to accommodate the *in vivo* environment. Given the recent reports of paraCEST designs that provide a direct readout of biological indices such as pH by a change in frequency rather than intensity, there are reasons to remain optimistic about the ultimate impact of these agents in the medical community. I believe that many exciting opportunities remain for chemists and engineers to design newer types of paraCEST agents that are safe, work well *in vivo*, and provide unique information to clinicians that simply cannot be done using other imaging methods.

1. "Lanthanide-DOTA-bis(amide) Complexes: Direct NMR Evidence for Differences in Water Molecule Exchange Rates for Coordination Isomers", S Zhang, Z Kovacs, S Burgess, S Aime, E Terreno & AD Sherry, Chem. Eur. J., **7**, 288-296 (2001).
2. "$^1$H and $^{17}$O NMR Detection of A Lanthanide-bound Water Molecule at Ambient Temperatures in Pure Water as Solvent", S Zhang, K Wu, MC Biewer, and AD Sherry, Inorg. Chem., **40**, 4284-4290 (2001).
3. "A Novel Europium(III)-Based MR Contrast Agent", S Zhang, PA Winter, K Wu & AD Sherry, J. Amer. Chem. Soc. **123**, 1517-1518 (2001).

**CEST MRI analysis methods**

Mark D. Pagel, University of Texas MD Anderson Cancer Center, Houston, TX USA

INTRODUCTION: The development of improved CEST MRI acquisition methods has revealed that Z-spectra contain a rich content of information, and are also influenced by conditions other than chemical exchange & saturation (e.g., T1 relaxation). A variety of analysis methods have been developed to extract information from CEST MRI studies, and to mitigate or eliminate the effects of other conditions. To date, no consensus has been reached regarding one method or a subset of methods that are best for CEST MRI analysis.

METHODS: This introductory presentation will review the underlying mechanisms of a variety of methods that analyze Z-spectra, while also comparing and contrasting the advantages and disadvantages of various analysis methods. Examples will be derived from a variety of previously reported studies.

RESULTS: As with most other imaging methodologies, the analysis of Z-spectra obtained from CEST MRI depends on the quantity and quality of experimental information to be analyzed, and the desired information to be gained. Therefore, no consensus *should* be reached regarding a single method that is best for analyzing Z-spectra. Instead, an analysis method should be selected that is appropriate for the CEST MRI acquisition method and the biomedical application. Importantly, each CEST MRI study should acknowledge the advantages and disadvantages of the analysis method used for the study, so that the conclusions of the study can be properly assessed.

DISCUSSION: This presentation is intended to provide an introduction that can aid discussions about subsequent presentations at the Beijing CEST 2018 meeting. More importantly, this presentation is intended to stimulate further discussion at the meeting.

ACKNOWLEDGEMENTS: This presentation is indebted to many colleagues within the CEST MRI research community who have developed an impressive variety of methods for analyzing Z-spectra obtained with CEST MRI.

## CEST and Spin-Lock MRI signals of glucose and glucose analogs

Tao Jin[1] and Seong-Gi Kim[2]

*[1]Department of Radiology, University of Pittsburgh, USA*
*[2]Center for Neuroscience Imaging Research, Institute for Basic Science, Korea; Department of Biomedical Engineering, Sungkyunkwan University, Korea*

**Introduction**: Unlabeled glucose (Glc) and glucose analogs can be detected indirectly by MRI through a change of water signal via chemical exchange saturation transfer (CEST) or chemical exchange-sensitive spin lock (CESL). These approaches have been used in animals and humans to characterize brain tumors [1-3], but it is still unclear whether the CEST/CESL signal with Glc injection mainly measures the intracellular pool indicating metabolism, or the extracellular pool indicating vascular permeability. Our first study is to examine the signal source of glucoCESL in tumor [4]. Recently, CEST and CESL MRI with injection of 3-O-Methyl-glucose (3OMG, a nonmetabolizable glucose analog) has been used to probe the glucose transport, but 3OMG is not an FDA-approved agent. Our second study is to measure the sensitivity and temporal characteristics of CESL with injection of D-xylose, which is also a nonmetabolizable glucose analog and has been approved by FDA for human malabsorption test.

**Methods:** 1) CESL MRI with intravenous injection of Glc, 2-deoxy-D-glucose (2DG) and non-transportable L-glucose were measured in rat brains with 9L tumors at 9.4 T, and compared with Gadolinium-based dynamic contrast-enhanced (DCE) MRI. 2) CESL MRI with injection of 1 g/kg of D-xylose were measured in normal rat brains (n=4). In each CESL study, images without and with T1rho-weighting (i.e., spin-lock time = 0 and 50 ms with 350-500 Hz spin lock power) were acquired in an interleaved manner, and a time series of R1rho maps were calculated [4,5].

**Results and Discussion**: The CESL R1rho with Glc injection has faster and larger changes in tumors than normal brain tissue. The CESL with 2DG injection in tumors has much larger and slower peak response than that with Glc due to the accumulation of 2DG and 2DG-6-phosphate in the intracellular compartment, while L-glucose, which cannot be transported intracellularly by glucose transporters, only induces a small and fast change. The early glucoCESL maps (<4 min) are similar to DCE images, and late maps have more widespread responses. The rise times of Glc-CESL and 2DG-CESL signals in the tumor are slower than those of DCE and L-glucose-CESL. Our data suggest that the initial CESL signal mainly reflects a passive increase of glucose content in the extracellular space of tumors due to a higher vascular permeability, while the later period (>4 min) may have a significant contribution from the uptake and/or metabolism of glucose in the intracellular compartment. In healthy rat brain, the CESL R1rho after the xylose injection reaches a peak at ~15 min, and decreases to about half of the peak magnitude at 60 min post injection. Compared to the R1rho change of 3OMG for the same dose [5], the peak magnitude of xylose-CESL is ~20% higher, but the decay of R1rho change is faster.

**Conclusions:** Our results show that glucoCESL MRI has both extracellular and intracellular contributions (4), and can be a useful tool for measurements of both vascular permeability and glucose uptake in tumors. Our results also show that xylose has higher peak sensitivity for CESL MRI than 3OMG, and can be used for future CEST or CESL study of glucose transport in both animal and human.

**References:**

1. Chan KWY, et al., Magn Reson Med 2012;68(6):1764-1773.
2. Walker-Samuel S, et al., Nat Med 2013;19(8):1067-1072.
3. Schuenke P, et al., Sci Rep 2017;7:42093.
4. Jin T, et al., Magn Reson Med 2018;80:488–495.
5. Jin T, et al., JCBFM 2017; 38:869-880.

# Dynamic Glucose Enhanced MRI in Animals and Humans

Xiang Xu[1,2]

*[1]Russell H. Morgan Department of Radiology and Radiological Science, Johns Hopkins University, Baltimore, MD, United States. [2]F. M. Kirby Research Center for Functional Brain Imaging, Kennedy Krieger Research Institute, Baltimore, MD, United States.*

**INTRODUCTION:** D-glucose can be used as a biocompatible contrast agent for cancer detection by employing its hydroxyl protons as a natural label for chemical exchange saturation transfer (glucoCEST)[1-4], spin Lock (glucoCESL)[5-7] or T2 relaxation[8,9]. When D-glucose enters the tumor, it diffuses into the extravascular extracellular space (EES) due to disruption of the blood brain barrier (BBB). Unlike gadolinium-based contrast agents, glucose can also be actively taken up in the cells via facilitated transport and metabolized. Recent progress will be shown for animals studies, where an on-resonance variable delay multi-pulse (onVDMP) method[10] was optimized to detect fast-exchanging protons hydroxyl protons in D-glucose and applied to study glucoCEST on a mouse model with a tumor. In the human study, continuous wave CEST (CW-CEST) method was used to study glucose uptake in human brain tumors.

**METHODS:** Animal study on 11.7T small animal scanner: Dynamic glucose enhanced (DGE) images were acquired using both onVDMP and CW-CEST for comparison. 32 binomial pulses (3ms, 15.6μT) with 10 ms mixing time between pulse pairs were applied.

Human study on 3T Philips MRI scanner: DGE images were acquired using two RF transmit channels afternatingly[11,12]. Each RF channel pulses for 50 ms alternatingly for a total of 1.0 s with $B1_{rms}$ of 1.6 μT.

**RESULTS and DISCUSSION:**

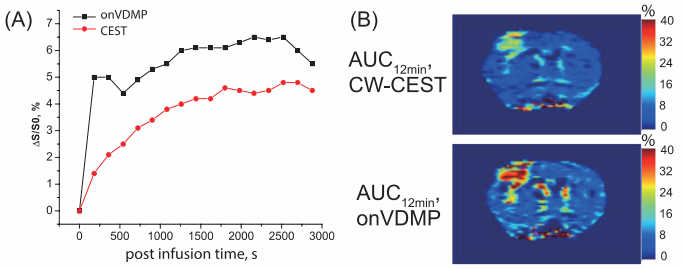



Figure 1. (A) glucoCEST signal detected by onVDMP and CW-CEST in the tumor region as a function of post infusion time. (B) The area under curve (AUC) images of onVDMP and CW-CEST over a period of 12 min post glucose infusion from the same mouse.

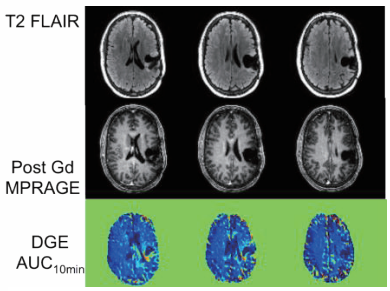



Figure 2. The T2 FLAIR, post Gd MPRAGE and DGE AUC image of a post surgery brain tumor patient.

Animal: The onVDMP method yields in average 1.8 times more signal than the CW-CEST method.

Human: DGE AUC images show signal enhancement in the area adjacent to the surgical cavity. Enhancement is also observed in an area inside the cavity, which also shows slight enhancement with Gd. The rest of brain shows negative signal possibly caused by a shift in the saturation frequency during the dynamic scan or water content in the tissue. For studies at 3T effects are about three times smaller than at 7T and motion may affect results.

**CONCLUSION:** In vivo human DGE imaging is possible at 3T. With more method developments, for example illustrated above on pre-clinical mice model, the sensitivity of glucoCEST can be further improved. However motion during dynamic scanning can lead to substantial imaging artifacts and has to be addressed for DGE imaging.

**ACKNOWLEDGMENTS:** NIH R01EB019934, P50CA103175, R01EB015032, and K99EB026312.

**REFERENCES:** 1.Chan KW, et al. Magn Reson Med. 2012; 68(6):1764-73. 2.Walker-Samuel S, et al. Nat Med. 2013; 19(8):1067-72. 3.Xu X, et al. Magn Reson Med. 2015; 74(6):1556-63. 4. Xu X, et al. Tomography. 2015; 1(2):105-14. 5. Jin T, et al Cereb. Blood Flow and Metab. 2014;34(8):1402-1410. 6. Zu Z, et al Magn. Reson Imag. 2014;32(9):1078-1084. 7. Paech D, et al. Radiology 2017 Jun 16:162351 8. Gore JC, et al. Magn Reson Med. 1986;3(3):463-466. 9. Yadav NN, et al. Magn Reson Med. 2014;72(3):823-828. 10. Xu J, Magn Reson Med. 2017; 77(2): 730-739. 11. Keupp J, et al. Proc Int Soc Magn Reson Med 2011;19(710). 12.Togao O et al. PLoS ONE 2016;11(5):e0155925.

**GlucoCEST of glucose analogs**

Michal Rivlin[1], Gil Navon[1]
*[1]School of Chemistry, Tel-Aviv University, Tel-Aviv, Israel*

**INTRODUCTION:**

CEST MRI of glucose has been proposed as a new molecular imaging approach for diagnosing tumors in view of its high sensitivity and the known enhanced glucose uptake by tumors [1]. However, the application of CEST-MRI of glucose is hampered by the facts that glucose is not accumulated in the tumors since it rapidly converted to lactic acid by glycolysis and by its dependence on the insulin secretion. 2-Deoxy D-glucose (2DG) and 2-fluoro-deoxy D-glucose (FDG) undergo phosphorylation without further metabolism and exhibit enhanced CEST signals in tumors [2,3], but due to their toxicity at high doses they cannot be used for humans. 3-O-Methyl-D-glucose (3OMG) is transported to cells by the glucose transporters without further metabolism and exhibits enhanced CEST and spin lock signals in breast tumors [4,5] and in brain tumors [6,7]. Although it is considered to be non-toxic its toxicity profile was not established. The amino glucose analogue glucosamine (GlcN), produce a significant CEST MRI signal in several murine and human breast cancer models [8]. Its potential for the clinical application is strengthened by its lack of toxicity as can be indicated from its wide use as food supplements [9]. The translation of GlcN CEST MRI method to clinical MRI scanner was examined, in order to evaluate the feasibility of the new reagent to obtain new class of images.

**METHODS:**

In vitro experiments were performed on phantoms consisted of GlcN solutions and were obtained with a 3T Siemens Prisma MRI scanner system. Images were acquired at room temperature using a 64-channel phased-array head coil for RF reception. The CEST protocol includes series of frequencies, using a train of 3-30 gauss saturation pulses with 50-100ms long, interpulse delay of 22-61 ms and 2 s pause between measurements, saturation attenuations were in the range of 1.0-3.0 μT. The images were acquired using a single-shot turbo gradient echo with cubic resolution of 3 $mm^3$.TR/TE/flip angle = 5.2 ms/2.7 ms/7$^o$

**RESULTS:**

The results of the in vitro studies clearly demonstrated that quantitative GlcN-CEST imaging is possible at a clinical 3T scanner. ~~We demonstrated that GlcN can be detected by CEST- MRI at a clinical scanner (3T)~~. The $MTR_{asym}$ of GlcN solution was significant in the hydroxyls regions over the entire saturation frequency offset range as well as over the range dominated by the amine protons transfer effect. Moreover, GlcN CEST signal showed dependence and sensitivity to the concentration and acidity of the solution.

**DISCUSSION:**

Initial phantom GlcN CEST MRI experiments at 3T have shown promising practical utility for evaluating cancer in clinical setting. GlcN generates a significant CEST MRI signal a few ppm far away from the water signal, arises from a mixture of GlcN hydroxyl protons groups and amine protons group. That gives as the hope that by using GlcN reagent it will be possible to eliminate spillover and direct effect arise from water signal. Additionally, in tumors, the signal is expected to be higher owing to the contribution of GlcN metabolic products that accumulate in the cells. Nevertheless, further investigation is needed to validate these results in vivo.

**CONCLUSION:**

This study showed that the CEST signal obtained with GlcN solution can be reliably detected at a clinical MRI scanner. These findings provide preliminary support for the potential use of GlcN as a new MRI contrast reagent for glucose uptake by tumors.

**REFERENCES:**

1. Chan K.W. *et al*. Magn Reson Med 2012; 68; 1764-1773.
2. Nasrallah F. A, *et al*. J Cereb Blood Flow Metab 2013; 33; 1270-1278.
3. Rivlin M, *et al*. Sci Rep 2013; 3: 3045, 1-7.
4. Rivlin M, *et al*. Magn Reson Med 2014; 72; 1375-1380.
5. Rivlin M, *et al*. Magn Reson Med 2018; 79; 1061-1069.
6. Zu Z, et al. Magn Reson Med 2018; 80; 1110-1117.
7. Sehgal A.A. *et al*. Magn Reson Med 2018; Early view
8. Rivlin M, *et al*. Sci Rep 2016; 6; 32648 1-7.
9. Anderson, J.W, *et al*. Food Chem Toxicol 2005; 43;187-201.

## Glucose-enhanced MRI: Applications in humans

Daniel Paech[1]

[1]*Department of Radiology, German Cancer Research Center, Heidelberg, Germany*

Medical imaging techniques greatly benefit from the application of contrast agents as they increase diagnostic accuracy. However, gadolinium based contrast agents are currently subject to criticism, since several studies reported accumulation of gadolinium in deep gray matter nuclei after serial application. Therefore, the development of novel MRI techniques using biodegradable contrast agents is highly desirable.

In this context, promising results have been reported using natural D-glucose as MRI contrast agent employing Chemical Exchange Saturation Transfer (CEST) and Chemical Exchange sensitive Spin-Lock (CESL) imaging approaches, both at ultra-high field strength. Recently, the feasibility of glucose-enhanced MRI for the detection of malignant brain tumors was proven in humans.[1-3] Studies indicate a major contribution of both blood brain barrier leakage and tissue perfusion to the signal enhancement in brain tumors.[4]

This talk will focus on human applications of dynamic glucose-enhanced (DGE) MRI at ultra-high field strength (7.0 - 9.4 Tesla) and discuss perspectives and current challenges of this novel technique.

DGE MRI may enable the detection of region specific glucose concentrations in tumors following intravenous glucose injection, with implications for biopsy targeting, patient therapy and response monitoring. However, the full diagnostic value of dynamic glucose enhanced MRI has to be evaluated in future studies with optimized protocols and in larger patient cohorts.

**REFERENCES:**

1. Xu X, Yadav NN, Knutsson L, et al. Dynamic Glucose-Enhanced (DGE) MRI: Translation to Human Scanning and First Results in Glioma Patients. Tomogr. J. Imaging Res. 2015;1:105–114. doi: 10.18383/j.tom.2015.00175.
2. Schuenke P, Koehler C, Korzowski A, et al. Adiabatically prepared spin-lock approach for T1ρ-based dynamic glucose enhanced MRI at ultrahigh fields. Magn. Reson. Med. 2016;78:215–225. doi: 10.1002/mrm.26370.
3. Paech D, Schuenke P, Koehler C, et al. T1ρ-weighted Dynamic Glucose-enhanced MR Imaging in the Human Brain. Radiology 2017;285:914–922. doi: 10.1148/radiol.2017162351.
4. Jin T, Iordanova B, Hitchens TK, Modo M, Wang P, Mehrens H, Kim S. Chemical exchange–sensitive spin-lock (CESL) MRI of glucose and analogs in brain tumors. Magn. Reson. Med. 2018 doi: 10.1002/mrm.27183.

**Will GlucoCEST MRI be able to visualise cancer in humans?**

Xavier Golay, University College London, on behalf of the GLINT consortium

Cancer accounts for 13% of all deaths worldwide and despite recent medical improvements remains one of the most deleterious diseases in the world.Tumour cells preferentially uptake glucose over normal cells, as they rely on enhanced aerobic glycolysis for their energy supply, which distinguishes them from normal tissue (the Warburg effect. This can be exploited to detect a glucose-based Chemical Exchange Saturation Transfer (GlucoCEST) signal, which should provide additional information over and above current medical *in vivo* imaging techniques in oncology (1,2). GlucoCEST has been shown to detect both native glucose and glucose (Glc) analogues such as 3-O-methyl-D-glucose (3OMG) uptake in tumour models. Based on these early experiments, we established the GLINT consortium (GlucoCEST Imaging of Neoplastic Tumours) to bring the combination of Glc and 3OMG as a combined exam to the clinics, thereby providing a wide-ranging new diagnostic tool for one of the most devastating diseases in the world.

Early experiments, both in humans and animal models at clinical field strengths show however that the GlucoCEST signal is very small in nature, and might be difficult to detect, let alone image at 3T. Both early experiments in head & neck and other body cancers, as well as in primary brain tumours have been undertaken in a 2-centre clinical trial so far (University College London and Max Planck Institute in Tuebingen). Test-retest, repeatability and reproducibility have been assessed, both theoretically and practically, and a preliminary assessment indicate that the technical difficulties linked to the measurements outside of the brains prohibit reliable detection of a signal, in our experiments. Reliable brain GlucoCEST signal has however been detected in both centres. This presentation will present the current state of this project.

Refs: 1) Chan et al, MRM, 68: 1764–1773 (2012); 2) Walker-Samuel et al, Nature Medicine, 19(8):1067-73 (2013)

Funding: European Union’s Horizon 2020 research and innovation programme (Grant Agreement No. 667510)

**Reproducibility study of CEST MRI using real-time motion and shim navigated CEST sequence**

Gizeaddis L. Simegn[1], Ali Alhamud[1,4], Andre J.W. Van der Kouwe[1,2,3], Ernesta Meintjes[1,4], and Frances Robertson[1,4]
*[1]UCT Medical Imaging Research Unit, Division of Biomedical Engineering, Department of Human Biology, University of Cape Town, Cape Town, South Africa, [2]Athinoula A. Martinos Center for Biomedical imaging/MGH, Charlestown, MA, United States, [3]Department of Radiology, Harvard Medical School, Boston, MA, United States, [4]Cape Universities Body Imaging Centre (CUBIC-UCT), Cape Town, South Africa*

**Introduction:** The effectiveness of CEST MRI for detecting macromolecules *in vivo* depends on several factors including body temperature, pH, the prepared static shimmed B0 and other experimental parameters. Repeated measurements on the same subject should produce similar results under the same environmental and experimental conditions. However, fluctuation in the static prepared B0 field, which may occur between measurements due to heating of the iron shim coils or subject motion, may alter CEST results and affect reproducibility. The aim of this study was to investigate how reproducible CEST MRI are during consecutive CEST acquisitions and to examine the feasibility of using a navigated CEST sequence with dynamic shim and motion correction.

**Methods:** Double volumetric navigators were inserted into a 2D EPI CEST sequence for real-time simultaneous motion and shim measurement and correction. The calf muscle of three healthy subjects was scanned using 18 channel knee coil. For every subject, ten CEST scans were acquired in two sessions (1) without shim correction applied (No ShimCo), and (2) with shim correction applied (ShimCo). In both sessions a 5-minute DTI sequence was run in between third and fourth CEST scans to introduce a dynamically changing field during the remaining scans subsequent to heating induced by the gradient-intensive diffusion scan and evaluate their effect on the reproducibility of CEST results. For all acquisitions, navigator parameters were: TR 13 ms, TE1/TE2 4.8 ms/7.0 ms, voxel size 8×8×8mm$^3$, bandwidth 4882 Hz/px and 2$^0$ flip-angle. CEST parameters were: TR 2 sec including the navigator time, TE 21 ms, 5 mm slice thickness, 43 frequency offsets (including two references, -3 to 3 ppm; step-size 0.15 ppm, targeting glycogen), rectangular RF pulse duration 1 sec and 1.5μT amplitude. All scans were performed on a Skyra 3T MRI scanner (Siemens, Erlangen, Germany) according to approved protocols. The MTRasym integral coefficient of variation (CoV) over 5 consecutive scans was calculated for each subject and compared between scans acquired with and without shim correction incorporated.

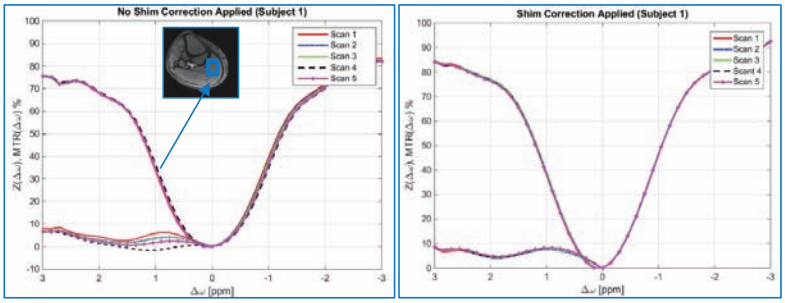



*Figure 1: CEST results for scans acquired without shim correction (left) and with shim correction applied (right).*

**Results:** Figure 1 shows the CEST and MTRasym curves for a single representative subject. The left figure shows CEST and MTRasym curves for scans acquired without applying shim correction (No ShimCo) while the right figure shows curves for scans acquired with shim correction applied (ShimCo). Figure 2 shows the MTRasym integral for consecutive scans, demonstrating more consistent values for scans acquired with shim correction than for those acquired without shim correction.

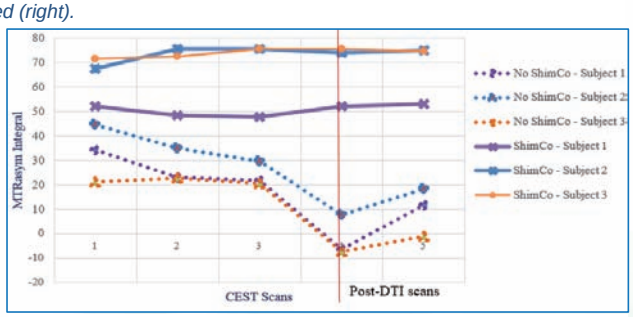



*Figure 2: MTRasym integral for consecutive scans during No ShimCo and ShimCo. Scans 4 and 5 are acquired post-DTI.*

**Discussion:** With shim correction**,** CEST spectra and MTRasym curves were reproducible in all subjects (maximum CoV of 4.74 %.), whereas without correction CEST and MTRasym curves were less consistent (minimum CoV of 90.74 %) (Fig. 1&2). In addition, a reduction in the MTRasym integral was observed for all post-DTI No ShimCo scans, whereas for the ShimCo scans, the MTRasym integral was relatively consistent (Fig. 2). This demonstrates that if not corrected, field inhomogeneity affects the CEST spectra misleading interpretation.

**Conclusion:** Our results demonstrate that the fluctuation in the B0 field will affect reproducibility of CEST data during consecutive scans and real-time prospective motion and shim corrected CEST sequence gives more reproducible measurements. This is important when conducting longitudinal studies or when using CEST MRI to assess treatment or physiological responses over time.

# Creatine and phosphocreatine mapping of mouse skeletal muscle by a polynomial and Lorentzian line-shape fitting CEST method

Lin Chen[1,2], Peter B. Barker[1,2], Robert G. Weiss[2,3], Peter C. M. van Zijl[1,2], Jiadi Xu[1,2,*]
1 F.M. Kirby Research Center for Functional Brain Imaging, Kennedy Krieger Research Institute, Baltimore, MD, USA
2 Russell H. Morgan Department of Radiology and Radiological Science, Johns Hopkins University School of Medicine, Baltimore, MD, USA
3 Division of Cardiology, Department of Medicine, Johns Hopkins University School of Medicine, Baltimore, MD, USA

**Introduction:** Creatine (Cr) and phosphocreatine (PCr) are the two primary components of the creatine kinase reaction, arguably the primary energy reserve reaction in muscle[1,2]. Previously, Haris et al. developed a CEST detection method to detect low concentrations of PCr and Cr in tissues[3,4]. Here, we extend our recently published polynomial and Lorentzian line-shape fitting (PLOF) method[5] to map the PCr and Cr concentrations simultaneously in mouse skeletal muscle.

**Methods:** Wild type (WT) mice and Guanidinoacetate N-Methyltransferase deficient (GAMT-/-) mice that have low Cr and PCr concentrations in muscle were used to assign the Cr and PCr peaks in the Z-spectrum at 11.7 T. A two-peak PLOF method was proposed to simultaneously extract and quantify the Cr and PCr by assuming a polynomial function for the background and two Lorentzian functions for the CEST peaks at 1.95 ppm and 2.5 ppm, respectively. All MR experiments were performed using a 11.7 T Bruker Biospec system. A CW-CEST sequence with RARE readout was used for the CEST MRI. In vivo MRS experiments were acquired using STEAM sequence (TE= 3 ms, TM=10 ms, TR=2.5 sec). Total image time was 8 mins.

**Results and Discussion:** The in vivo $^1$H MRS spectra in Fig 1A&B show that the tCr concentration of the GAMT-/- skeletal muscle (1.2 ± 0.8 mM, n=3) is significantly reduced compared to that of the WT mouse (38.8 ± 2.8 mM, n=3). Notably, the spectrum of GAMT -/- mice exhibits appreciable PGua signal at 3.78 ppm[6]. The Z-spectra of the 30 mM Cr and PCr phantoms at pH = 7.0 recorded with 1 μT saturation power are shown in Fig. 1C. There is one strong peak around 2.0 ppm present in the Cr CEST Z-spectrum, while two peaks around 2.0 ppm and 2.5 ppm are observed in the PCr CEST Z-spectrum. A comparison between the Z-spectra of GAMT -/- and WT mice with a saturation power of 1 μT are shown in Fig. 1D. The Z-spectrum of the WT mouse showed two clear peaks around 1.95 ppm and 2.5 ppm, while there was only one sharp peak around 2.2 ppm in the Z-spectrum of the GAMT-/- mice. Different from the previous brain study[5], mobile protein guanidium protons are not detected in skeletal muscle and the amide peak is small with a maximum amplitude of around 1.2% of water magnetization. The disappearance of the protein guanidinium peak and the reduction of the amide peaks from the proteins are favorable to the extraction of clean Cr and PCr CEST signal. The extracted true apparent relaxation rates $R_{1.95}^{max}$ and $R_{2.5}^{max}$ of WT mouse skeletal muscle at a saturation power of 1 μT are shown in Figs. 2B&C, respectively. The calibrated concentration maps of Cr and PCr are shown in Figs. 2D&E, respectively. The goodness of the PLOF fitting for each pixel is illustrated by the normalized mean square error (NMSE) map shown in Fig. 2F. The mean value and standard deviation of the NMSE map are 0.9922 and 0.0034, respectively. The averaged Cr and PCr concentrations of the WT mouse skeletal muscle were determined to be 11.3 ± 1.4 mM and 30.8 ± 2.8 mM, respectively, which are slightly higher than previously reported values (Cr 7.5 mM : PCr 22.5 mM) from spectroscopy[6,7]. The PCr and Cr maps are not following any pattern of muscle anatomy, which may be due to the relatively low resolution or small differences in concentrations between the different muscle types. Also, the edges of the PCr and Cr maps (transition from muscle to air) show strong concentration gradients due to the partial volume effects.

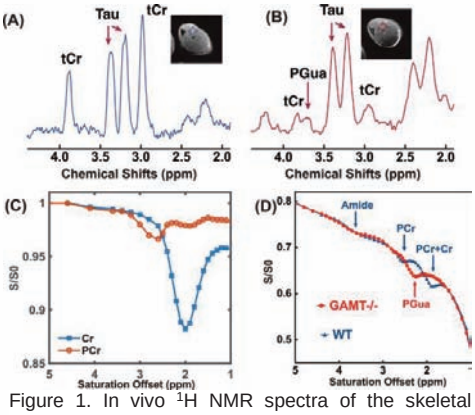



Figure 1. In vivo $^1$H NMR spectra of the skeletal muscle of (A) a WT mouse and (B) a GAMT-/- mouse. (C) The Z-spectra of 30 mM PCr (red) and Cr (blue) solutions recorded using CW-CEST with 1 μT saturation power and 3 s length. (D) The aligned averaged Z-spectra of GAMT -/- (n=3) and WT mice (n=3) collected with a saturation power of 1 μT (3 s length).

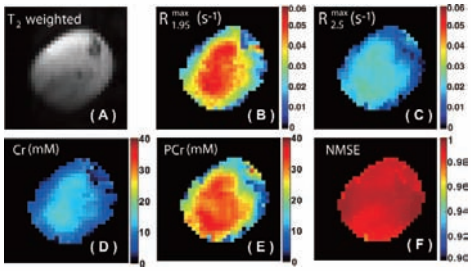



Figure 2. Creatine and phosphocreatine mapping of WT mouse skeletal muscle. (A) $T_2$ weighted image of the mouse hind leg used for anatomical guidance. The extracted maps of (B) $R_{1.95}^{max}$ and (C) $R_{2.5}^{max}$ determined by the PLOF method using the Z-spectrum recorded with a saturation power of 1 μT. (D) Cr concentrations map and (E) PCr concentration map calibrated by MRS. (F) NMSE map.

**Conclusion:** The PLOF method provides an efficient way to map Cr and PCr concentrations simultaneously in the skeletal muscle at high MRI field.

**Acknowledgment:** This work was supported by NIH R01EB015032, P41EB015909, R01HL63030 and R01HL61912.

**References:** [1] Wyss M, et al. Physiol Rev 2000;80:1107. [2] Andres RH, et al. Brain Res Bull 2008;76(4):329-343. [3] Haris M, et al. NMR Biomed 2012;25(11):1305-1309. [4] Haris M, et al. Nat Med 2014;20(2):209-214. [5] Chen L, et al. NMR Biomed 2017;30: e3834. [6] Renema WK, et al. Magn Reson Med 2003;50(5):936-943. [7] t Zandt Hi, et al. J Physiol 2003;548(3):847-858.

## *In vivo* proton exchange rate of healthy human brains quantified with omega plot

Mehran Shaghaghi[1],Weiwei Chen[2], Alessandro Scotti[1,3], Haiqi Ye[2], Yan Zhang[2], Wenzhen Zhu[2], *Kejia Cai[1,3,4]
[1]Department of Radiology, [3]Bioengieering, [4]Center for MR Research, University of Illinois at Chicago, Chicago, IL, USA 60612
[2]Department of Radiology, Tongji Hospital, Tongji Medical College, Huazhong University of Science & Technology, Wuhan, Hubei, China 430030

**Purpose:** Proton exchange is the fundamental mechanism underpinning CEST MRI contrast, and it has been reported that mapping of the proton exchange rate ($K_{ex}$) may help the clinic diagnosis of stroke and cancer [1, 2]. Omega plot has been used to calculate proton exchange rates of paraCEST agents [3], which labile protons resonate far off from water resonance and hence provide a contrast unperturbed by the direct saturation (DS) or spillover effect. Spillover-corrected omega plots have been successfully implemented for $K_{ex}$ mapping in solutions [4]. Here, we aim to map the proton exchange rate of *in vivo* human brains using omega plot and direct saturation removed Z-Spectral data.

**Introduction:** Proton MRI signals ($M_z$) acquired at different saturation power ($B_1$) are used to construct the "omega plots" [3] for measuring exchange rate directly from the X-intercept of the plot. However, the acquired MRI signal post saturation is not purely affected by proton exchange manipulated mechanisms, such as CEST, MT, and NOE effects. It is also affect by the dominant water DS (or spillover) effect particularly when the saturation offset is close to water central frequency. To remove the DS effect, Z-spectrum fitting with multiple Lorentzian functions was proposed [5] and have gained in popularity. In this study, we will compute proton exchange rate maps of healthy human brains with omega plot. Brain Z-spectrum data were collected and fitted to remove the DS component. $M_z$ free from direct saturation contribution is then used in the omega plot for computing $K_{ex}$ in the brain.

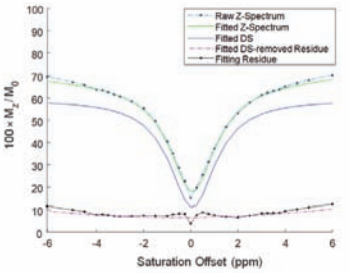



**Fig 1.** Representative Z-spectrum from a healthy brain with Lorentzian fittings to remove water DS. Saturation power = 1 μT.

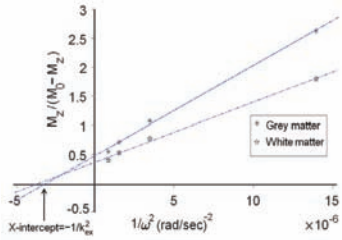



**Fig 2.** Typical omega plot $M_z/(M_0-M_z)$ vs. $1/\omega^2$ for gray (close stars) and white (open stars) matters in a healthy subject's brain.

**Methods:** Ten healthy human subjects were MRI scanned at a 3T GE MR750 scanner. Z-spectra of the brain were acquired at five increasing saturation power ($B_1$=1,2,3,4 & 5 μT), with saturation duration of 1.5 s, and frequency offsets ranging from -6 to +6 ppm, +15.6 & +39.1 ppm. Z-spectral raw data were fitted to a model including 2 Lorentzian functions, corresponding to DS, and the DS-removed residual spectrum (**Fig. 1**). DS fit was then subtracted from the raw Z-spectra and the $B_0$-corrected residual signals ($M_z$ at +3.5ppm) were used for further omega plot analysis (**Fig. 2**). The omega plot was constructed by computing $M_z/(M_0-M_z)$ as a linear function of $1/\omega^2$, where $M_0$ is taken from the signal at 39.1ppm and $\omega_1=\gamma B_1$ is in unit of rad/s. The pixel-wise exchange rate $K_{ex}$ is then calculated from the intercept on the X axis of the omega plot as shown in **Fig. 2**. Two-tailed paired Student's T-test was used to compare $K_{ex}$ in brain gray matter (GM) and white matter (WM), which were segmented based on MT contrast maps using MATLAB's routine 'Fuzzy C-Means Clustering' method. In order to validate this approach for proton exchange rate quantification, *in vitro* protein solution phantoms (20% BSA, n=3) at varied pH (6.2, 6.6, 7.0 & 7.4) were studied with the same protocols at a 9.4T preclinical Agilent MRI System.

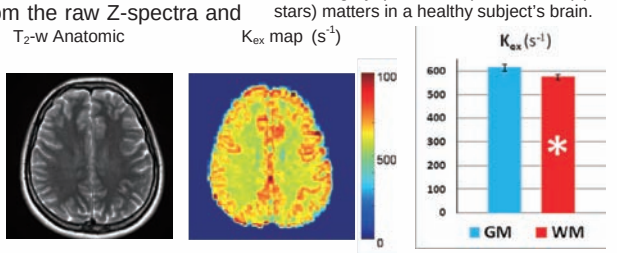



**Fig 3.** A) $T_2$-weighted anatomical image of a representative subject. B) The corresponding exchange rate map. C) Gray mater shows significant higher $K_{ex}$ than white matter (*p < 0.001).

**Results:** *In vivo* $K_{ex}$ mapping of human brains shows significant distinction between gray and white matter, with average value of 575±20 $s^{-1}$ for WM and 616±29 $s^{-1}$ for GM ($p < 0.001$) (**Fig. 3**). The constructed $K_{ex}$ maps are free from apparent imaging artifacts. In the phantom study (**Fig. 4**), exchange rate maps show increased $K_{ex}$ with increasing pH as expected [6].

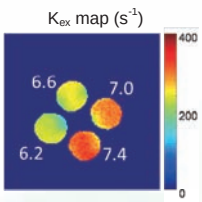



**Fig 4.** Exchange rate ($s^{-1}$) maps from the phantom study show proton exchange rate value increase with pH.

**Discussion and Conclusion:** In this study, we demonstrated the *in vivo* proton exchange rate mapping of human brain, delineating differences in gray and white matter. The fundamental mechanism at the origin of this difference is under investigation. Our analytic approach was validated with imaging phantoms. The imaging time can be greatly shortened with reduced number of Z-spectra, sparse data points, and fast imaging acquisition. In conclusion, this study shows great promise for *in vivo* proton exchange rate imaging and its clinical applications.

**References:** [1] Zhou, J. et al. MRM 50: 1120-1126. [2] Cai, K. et al. Nat. Med.18:302–306. [3] Dixon W.T. et al. MRM 63(3):625-32. [4] Sun, Z.S. et al. Contrast Media Mol. Imaging. 9(4):268–275. [5] Cai, K. et al. NMR Biomed. 28(1):1-8. [6] Jin T. et al. MRM 65(5):1448-60.

**Acknowledgment:** This study is supported by US NIH grant R21EB023516 and China NSF grant 81401390.

## Optimized dualCEST-MRI for imaging of endogenous bulk mobile proteins in the human brain

Johannes Breitling[1], Steffen Goerke[1], Moritz Zaiss[2], Yannick Soehngen[1], Anagha Deshmane[2], Kai Herz[2], Philip Boyd[1], Mark E. Ladd[1], and Peter Bachert[1]

[1]*German Cancer Research Center (DKFZ), Heidelberg, Germany*
[2]*Max-Planck-Institute for Biological Cybernetics, Tübingen, Germany*

**Introduction:** Recently we demonstrated that a selective detection of endogenous bulk mobile proteins in living tissue can be realized by the novel approach of dual-frequency irradiation CEST (dualCEST)-MRI[1] without contamination of saturation transfer effects of metabolites, lipids and semi-solids. For this approach, specificity is achieved by measuring the intramolecular magnetization transfer (i.e. saturation crosstalk T) between CEST signals resonating at two different frequency offsets $\Delta\omega$ and $\Delta\omega_c$ (Fig. 1a). Such a non-invasive imaging technique may be of particular interest for the detection of pathological alterations of protein expression, such as in neurodegenerative diseases or cancer. Until now, application in clinical trials was prevented by the inherently small signal-to-noise ratio (SNR) in comparison to conventional CEST approaches. Here, we present further developments in signal preparation, image acquisition and post-processing techniques enabling dualCEST examinations in a reasonable and clinically-relevant time frame.

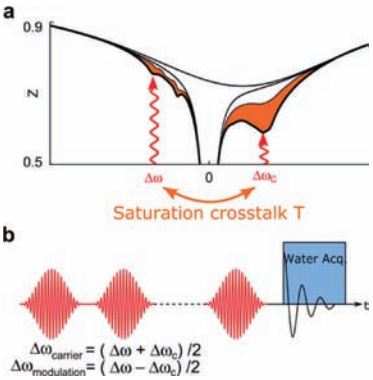



**Fig. 1: (a)** dualCEST detects the coupling of CEST signals, allowing the selective detection of bulk mobile proteins. **(b)** Scheme of the adapted pulse sequence with cosine-modulated Gaussian-shaped pulses.

**Methods:** The improvement in image quality was achieved by the following modifications: (i) The previously used pre-saturation scheme with an alternating irradiation at $\Delta\omega$ and $\Delta\omega_c$ was replaced by cosine-modulated Gaussian-shaped pulses[2] allowing a simultaneous saturation at the two frequency offsets (Fig. 1b), and thus, an effective doubling of the duty cycle. To avoid unintentional direct water saturation at the carrier frequency (Fig. 1b, equations) due to imperfections of the cosine modulation, slightly asymmetric frequency offsets (i.e. 3.5 and -5.5 ppm) were applied. (ii) Further improvement was achieved by adjusting the number of repetitions used for the averaging of the individual frequency offset combinations. The optimal allocation of measurements per frequency offset combination was determined by minimizing the error of the final contrast. (iii) In addition, the image readout was extended from a 2D to a 3D acquisition mode by implementing the snapshot-CEST approach[3] with parameters adapted from [4]. First of all, 3D readout intrinsically increased the image SNR, and secondly, allowed for retrospective motion correction and de-noising approaches. DualCEST-MRI (1.7×1.7×3 $mm^3$, 12 slices, total measurement time of 20 min including $T_1$-mapping and WASABI[5]) was performed on a 3 T whole-body scanner (Siemens Prisma) using the previously optimized pre-saturation parameters ($t_p$ = 20 ms, effective mean $B_1$ = 2 µT, $t_{sat}$ = 6 s, and DC = 85%)[1]. The isolated protein contrast $T_{protein}$ was calculated as defined in [1] and linearly corrected for $B_1$-inhomogeneities.

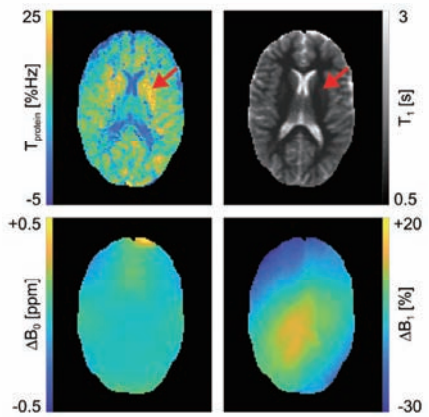



**Fig. 2:** DualCEST examination of a healthy volunteer (slice 2/12): $T_{protein}$, $T_1$-map and field maps displaying $B_1$- and $B_0$-inhomogeneities.

**Results & Discussion:** Correct functioning of the dualCEST measurement was confirmed by $T_{protein}$ values around zero in the cerebrospinal fluid (CSF) (Fig. 2), where negligible amounts of proteins are expected. In comparison to previous results a signal difference between grey and white matter was now observable by the improved image quality. Interestingly, a hyperintense region in the putamen (Fig. 2 red arrows) was consistently detected across all relevant slices. No image artefacts due to $B_0$- or $B_1$-inhomogeneities (Fig. 2 bottom row) were visible in the dualCEST contrast; even in basal brain regions (data not shown) where inhomogeneities are maximal.

**Conclusion:** The presented further developments enable a 3D dualCEST-MRI of the human brain in a reasonable and clinically-relevant time frame. With these prerequisites met, it will now be possible to investigate the diagnostic value of the dualCEST approach in clinical trials (e.g. Alzheimer's disease or cancer).

**References:** [1] Goerke S, et al. NMR Biomed 2018; 31:e3920. [2] Prevost VH, et al. NMR Biomed 2017; 30:e3706 [3] Zaiss M, et al. NMR Biomed 2018; 31:e3879. [4] Deshmane A, et al. ISMRM-ESMRMB 2018; #2249. [5] Schuenke P, et al. Magn Reson Med 2017; 77:571-580.

**Improved Fat-Water Separation Using Multipeak Reconstruction for Suppression of Lipid Artifacts In Chemical Exchange Saturation Transfer (CEST) Imaging**

Yu Zhao, Jianqi Li

*Shanghai Key Laboratory of Magnetic Resonance, East China Normal University, Shanghai 200062, China.*

**INTRODUCTION**: CEST has shown great application potentials in body in the assessment of tumor status and treatment response monitoring (1). However, the presence of strong lipid signals is a big challenge for body CEST imaging, because fat can lead to erroneous CEST contrast. The CEST-Dixon method has been proposed to remove the artifacts caused by the presence of lipid (2), which modeled fat as a single spectral peak at -3.4 ppm relative to water. Actually, multiple spectral peaks of fat exist. This inaccuracy in the signal model of fat results in incompletely water-fat separation and lipid artifacts (2).The aim of this study is to develop an accurate water-fat separation method for the CEST imaging.

**METHODS**: An agar-based fat-water phantom was constructed and included ε-Poly-L-lysine(5% w/w) and olive oil (40%w/w). Experiments were performed at 3 Tesla Siemens Prisma MRI scanner with a 20 channel head coil.The CEST preparation consisted of 8 Gaussian-shaped pulses, each 200 ms long, and the average $B_1$ =1.6 μT. The CEST images were acquired using 2-dimensional 6-point Dixon sequence with repetition time (TR)/echo time (TE1)/ΔTE = 20/2.3/1.7ms.A total of 61 offsets were acquired in the Z-spectrum from -6 ppm to 6 ppm. The CEST-PRESS sequence had the identical saturation scheme.

A multipeak fat model was proposed for water-fat separation. The resonance frequencies and relative amplitudes of these peaks were measured by the $^1$H-NMR spectrum and were taken as the priories for water-fat separation. In the water-fat separation, a nonlinear fitting was performed using Levenberg-Marquardt algorithm with the initial guess from T2 *-IDEAL algorithm. Finally, the CEST result was obtained after correction of field inhomogeneity using the B0 map simultaneously reconstructed in the water-fat separation. Using results from CEST-PRESS spectrum sequence as references, we compared our method with currently reported 3-point method (2).

**RESULTS**: In phantom experiment, the Z-spectra from the 3-point method shows an obvious dip in the vicinity of t -3.5 ppm(Fig. 1a), compared with results from CEST-PRESS. $MTR_{asym}$ result also shows a dip in the vicinity of 3.5 ppm(Fig. 1c).The results from the proposed method are consistent with the results from CEST-PRESS(Figs. 1b and 1d).

**DISCUSSION**:The Z-spectra calculated using the 3-point DIXON method shows a dip at -3.5 ppm, and this biased water-fat decomposition introduces additional asymmetries to the $MTR_{asym}$, at high fat-fraction. The single peak in the fat signal model used in the 3-point method may be the main reason of the biased water-fat decomposition and the overlook of R2* may be another reason. The proposed method is an accurate water–fat separation method and it is due to the accurate multipeak model for fat signal and hybrid fitting algorithm.

**CONCLUSION**: DIXON method with multiple fat peaks model removes lipid artifacts successfully and leads to significantly improved accuracy for CEST image, especially at high fat-fractions.

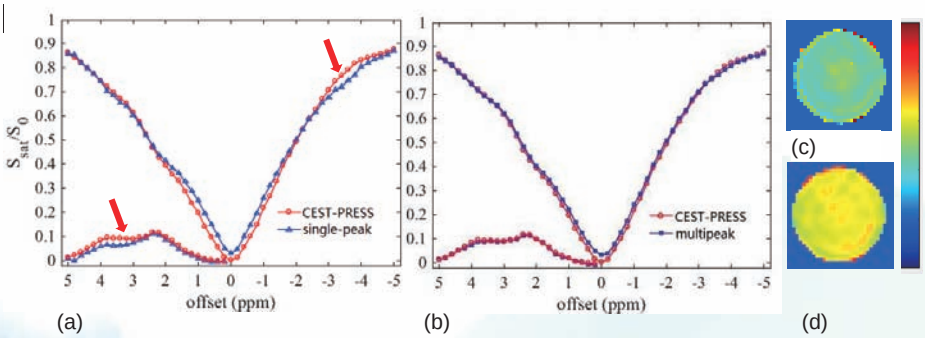



Figure 1. Comparison of two water-fat separation. (a) The Z-spectra from 3-point DIXON method shows a dip at -3.5 ppm and this biased water-fat decomposition introduces additional asymmetries to the $MTR_{asym}$ (marked by arrows). (b) With this artifact removed, the Z-spectra from DIXON method with multiple fat peaks model shows an appropriate estimation. (c) $MTR_{asym}$ (3.5ppm) maps are constructed using methods with single fat peak model (c) and multiple fat peaks model (d).

**REFERENCES:**

1. Dula, A.N., et al. Magn Reson Med, 2013. 70(1): 216-24.
2. Zhang, S., et al. Magn Reson Med, 2018. 80(3): 895-903

## FullHD CEST imaging in the human brain at 7T

Jan-Eric Meissner[1], Johannes Breitling[1], Ferdinand Zimmerman[1], Steffen Goerke[1], Andreas Korzowski[1], Moritz Zaiss[2], Mark E. Ladd[1], Peter Bachert[1]

*[1]German Cancer Research Center (DKFZ), Heidelberg, Baden-Wuerttemberg, Germany*
*[2]Max Planck Institute for Biological Cybernetics, Tuebingen, Germany*

**Introduction:** Spectral highly resolved Z-spectra *in vivo* are desirable for e.g. peak assignment in quantitative CEST, identification of CEST signal substructures, machine learning approaches or sequence parameter optimization. We showed that the acquisition of densely sampled Z-spectra is possible. By applying latest developments in 3D image acquisition and post-processing including motion correction, steady state compensation and spectral denoising, we overcame limitations in measurement time.

**Methods:** Imaging: Z-spectra were obtained using the Snap-shot sequence[1] (18 slices, resolution 1.72x1.72x3 $mm^3$) at 7T (Siemens MAGNETOM) using a 24-channel head coil. Presaturation was achieved by a train of Gaussian-shaped pulses ($t_{sat}$ = 1.875 s, $t_p$ = 100 ms, DC = 80%) for three saturation amplitudes of $B_1$ = 0.3, 0.6 and 0.9 µT. Each Z-spectrum was densely sampled employing 328 adapted frequency offsets. $T_1$–mapping was achieved by saturation recovery GRE. The WASABI sequence[2] yielded maps of $B_0$ and $B_1$ field inhomogeneities. An additional calibration measurement was performed to allow determining steady-state Z-spectra without the application of saturation in compliance with the steady-state criterion[3]. A total of 1080 3D volumes, i.e. FullHD, were acquired in about 90 min. Post processing: Images were corrected for motion using MITK[4]. After normalization the calibration measurement was used to retrospectively derive steady- state Z-spectra[3]. Finally, $B_0$-correction and denoising using principle component analysis were applied.

**Results and Discussion:**
Figure 1 shows the obtained Z-spectra of representable white and gray brain matter ROIs for saturation amplitudes $B_1$ = 0.3 and 0.6 µT. The highest $B_1$ amplitude was acquired for potential $B_1$-correction. Clearly visible are the known peaks at 3.5, 2.0 and -3.3 ppm attributed to the CEST signal of amides, amines and the rNOE, respectively. Especially for lower $B_1$ values additional peaks at 2.7 and -1.6 ppm could be suspected in accordance to the recently published highly resolved Z-spectra at 9.4 T[5]. The applied protocol provides a six fold increase in data acquisition per measurement time compared to our standard protocol. This could be used to investigate e.g. rNOE CEST signal substructures within a reasonable time frame *in vivo*.

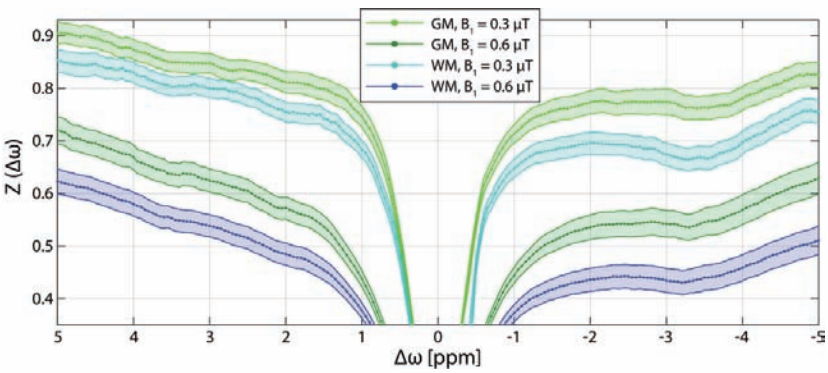



Figure 1: Region-of-interest (ROI) Z-spectra of white (WM, blue) and gray (GM, green) brain matter for different saturation amplitudes $B_1$. Error bars indicate standard deviation within ROIs.

**Conclusion:** We were able to acquire in vivo Z-spectra with considerable high spectral resolution and an extensive coverage of the brain. This was possible due to improved CEST image acquisition techniques, as e.g. the calculation of steady state Z-spectra from only shortly saturated images, and denoising. The outcome is ready for multi-pool relaxation corrections[6,7]. The FullHD CEST protocol could be used in the future as a ground truth measurement for machine learning approaches or to benchmark and optimize sequence or analysis parameters.

**Acknowledgments:** We kindly acknowledge the help of Ralf Floca implementing the image registration.

**References:** [1] Zaiss, M. et al. *NMR Biomed.* 31, 1-14 (2018) [2] Schuenke, P. et al. *Magn Reson Med.* 77, 571-580 (2016) [3] Breitling, J. et al. *Proc Intl Soc Mag Reson Med.* 26, 2240 (2018) [4] Nolden, M. et al. *Int J Comput Assist Radiol Surg.* 8, 607-620 (2013) [5] Schuppert, M. et al. *Proc Intl Soc Mag Reson Med.* 26, 558 (2018) [6] Windschuh, J. et al. *NMR Biomed.* 28, 529-37 (2015) [7] Zaiss, M. et al. *NMR Biomed.* 27, 240–252 (2014)

**Comparison of Different CEST Metrics for Brain Tumor Grading**

Ruibin Liu[1], Xianlong Wang[2], Zhibo Wen[2], Jinyuan Zhou[3], Yi Zhang[1,3]

[1]College of Biomedical Engineering & Instrument Science, Zhejiang University, Hangzhou, Zhejiang, China

[2]Department of Radiology, Zhujiang Hospital, Southern Medical University, Guangzhou, Guangdong, China

[3]Department of Radiology, Johns Hopkins University, Baltimore, Maryland, USA

**INTRODUCTION**: Chemical Exchange Saturation Transfer (CEST) imaging (1) has shown promising ability to detect various metabolites *in vivo*. Amide proton transfer (APT) imaging (2), one of the CEST imaging techniques, can detect endogenous mobile proteins / peptides and has been used for brain tumor grading (3). However, the APT signal can be complicated by the effects of direct water saturation (DS), semi-solid macromolecular magnetization transfer (MT) (4), and other exchanging pools. Several published studies have attempted to separate the pure APT effect from other competing effects by using various CEST metrics in conjunction with z-spectrum fitting (5). However, z-spectrum fitting typically requires a significant number of CEST saturation offset frequencies and is susceptible to local minima during numerical optimization, and thus may not be optimal in routine clinical applications. In this study, we aimed to compare the performance of three CEST metrics including CESTR, $\mathrm{CESTR^{nr}}$, $\mathrm{MTR_{rex}}$ at various frequency offsets without z-spectrum fitting for human brain tumor grading.

**METHODS**: All experiments were performed on a Philips 3T Achieva scanner. This study was approved by the local Institutional Review Board, and informed consent forms were obtained from all participants. We recruited 22 patients (11 males, 11 females; age range: 17-72 years), including 12 confirmed high-grade and 10 confirmed low-grade glioma patients. CEST imaging was performed using the following parameters: RF saturation power = 2 uT, TR/TE = 3000/11 ms, FOV = 230×230 $mm^2$, slice thickness = 6 mm, and scan duration = 3.2 min. CEST z-spectrum were acquired with 63 frequency offsets from 6 to -6ppm plus 15.6ppm. CESTR was calculated by subtracting the reference signal from the label signal (2) as follows, $CESTR = (S_{ref} - S_{lab})/S_0 = Z_{ref} - Z_{lab}$, where $S_{ref}$ is the reference signal, $S_{lab}$ is the label signal, $S_0$ is the unsaturated signal, and $Z_{ref}$ and $Z_{lab}$ are the corresponding normalized z-spectrum signal. We took the signal in the opposite frequency offset as the reference signal. Another CEST metric was obtained via normalizing CESTR by the reference signal $Z_{ref}$ as $CESTR^{nr} = (Z_{ref} - Z_{lab})/Z_{ref}$ (5). In addition, $\mathrm{MTR_{rex}}$ was calculated by subtraction of the inverse z-spectrum as $MTR_{rex} = 1/Z_{lab} - 1/Z_{ref}$ (6). The performance of the three aforementioned CEST metrics including CESTR, $\mathrm{CESTR^{nr}}$, $\mathrm{MTR_{rex}}$ was compared for grading brain gliomas at the frequency offsets of 3.5, 3, 2.5, 2,1.5, and 1 ppm, respectively. For each patient, a metric contrast was calculated as the difference between tumor and contralateral normal control regions. The Receiver Operating Characteristic (ROC) curve was used to evaluate the performance of different metrics in tumor grading.

**RESULTS**: From the comparison of different CEST metric maps at various frequency offsets, 3.5 ppm and 3 ppm generated more distinct contrast than the other frequency offsets (Fig.1). Furthermore, area under curve (AUC) of the ROC curve for the performance of three metric contrasts at various frequency offsets also attested that 3.5 ppm and 3 ppm were superior to the other frequency offsets in terms of grading tumors (Fig.2).

**CONCLUSION**: The results of this preliminary study indicate that CEST metrics including CESTR, $CESTR^{nr}$, $\mathrm{MTR_{rex}}$ at 3.5 ppm and 3 ppm were superior to 2.5 ppm, 2 ppm, 1.5 ppm and 1 ppm for grading human brain gliomas.

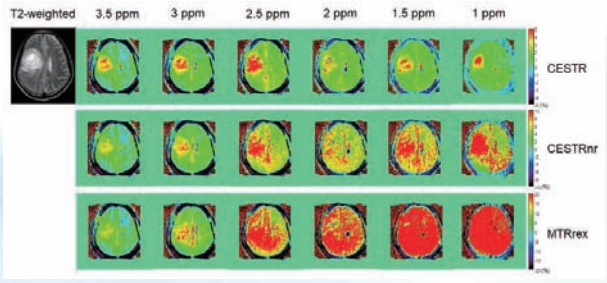



**Fig. 1.** Comparison of CESTR (top row), CESTRnr (middle row) and MTRrex (bottom row) maps at various frequency offsets.

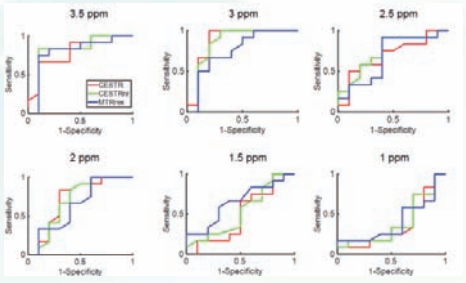



**Fig. 2.** Comparison of ROC curves from different CEST metric contrasts for tumor grading at various frequency offsets (ROI drawn in tumor and contralateral normal region).

**REFERENCE:** 1. Ward K, et al. J Magn Reson 2000;143:79-87. 2. Zhou J, et al. Nat Med 2003;9:1085-1090. 3. Zhou J, et al. Magn Reson Med: ISMRM 2008;60:842-849. 4. Sun P Z, et al. Magn Reson Med 2008;60:390-397. 5. Heo H Y, et al. Magn Reson Med 2017;77:1853-1865. 6. Zaiss M, et al. NMR Biomed 2014;27:240-252.

## Chemical Exchange Saturation Transfer (CEST) Imaging of Phosphocreatine in the Muscle at 15.2T

Julius Juhyun Chung[1,2], Tao Jin[3], Jung Hee Lee[1,2,4,5*], Seong-Gi Kim[1,2,4]

[1] Center for Neuroscience Imaging Research, Institute for Basic Science(IBS), Suwon 16419, Korea, [2]Samsung Advanced Institute for Health Sciences and Technology, Sungkyunkwan University, Seoul, Korea, [3]Department of Radiology, University of Pittsburgh, Pittsburgh, Pennsylvania, United States, [4]Department of Biomedical Engineering, Sungkyunkwan University, Suwon, Korea [5]Department of Radiology, Samsung Medical Center, Sungkyunkwan University School of Medicine, Seoul, Korea

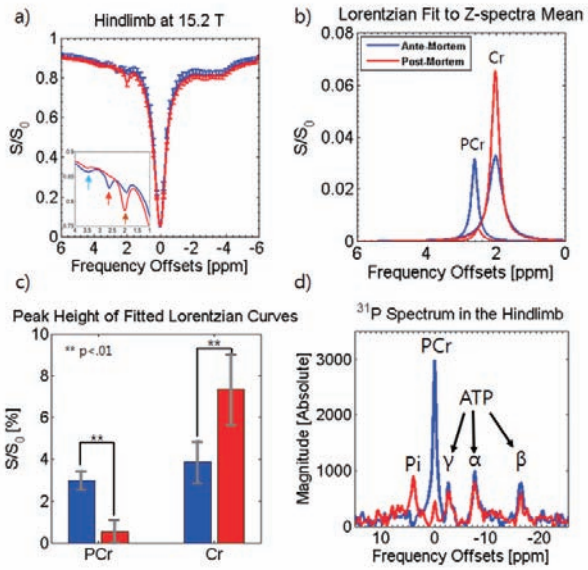
**Introduction**: Creatine dephosphorylation is a vital process involved in the metabolic upkeep of tissues with high energy expenditure such as the brain, muscles, and heart. An understanding of the metabolites involved with these procedures is highly beneficial to the understanding of metabolic well-being. Therefore, our goal was to characterize CEST signal of phosphocreatine (PCrCEST) in vivo in the muscle.

**Methods**: Z-spectra (n = 6) were analyzed using multi-pool Lorentzian fitting in the mouse hindlimb. Modulation of PCr signal in PCrCEST and $^{31}$P-MRS was observed in the mouse hindlimb before and after euthanasia.

**Results**: PCrCEST in the hindlimb was measured to be 2.98% ± .43 at 20 Hz power at 15.2 T. After euthanasia, PCrCEST signal dropped by 82.3% compared to an 85% decrease in PCr in $^{31}$P-MRS while CrCEST signal increased by 90.6%.

**Discussion**: PCrCEST shows signal sensitivity at a comparable level to APT* of the rat brain at 15.2 T (2.87% [1]). The drop in PCrCEST signal post-mortem reflected consumption of PCr to replenish ATP as well as a drop in pH.

**Conclusion**: PCrCEST is a technique with viable sensitivity in the muscle at high fields and shows promise for study of metabolic dysfunction and cardiac systems.




***In vivo* Z-spectra analysis of the hindlimb at 15.2 T and $^{31}$P-MRS at 9.4 T before and after euthanasia**. Z-spectra with error bars are shown before (blue) and after euthanasia (red) at 20 Hz with a 4 s duration at 15.2T (a) and expanded Z-spectra at a range of 1.0 to 4.0 ppm are shown inset. Error bars are only shown on one side of the curve for better visualization. PCr and Cr peaks obtained from multi-pool Lorentzian fitting are shown before and after euthanasia (b) and a statistical analysis of peak height show significant differences (c). $^{31}$P-MRS spectra at 9.4T are shown overlaid before and after euthanasia (d).

**References**:

1. Chung JJ, et al. NMR in Biomed 2017; 30(9). doi: 10.1002/nbm.3740.

**Proton Exchange Rate, Volume Fraction, $T_1$, and $T_2$ MR Fingerprinting using an Optimized Acquisition Schedule and a Deep RecOnstruction NEtwork (DRONE)**

*Or Perlman[1], Ouri Cohen[1], Shuning Huang[1], Inge Mulder[2], Cenk Ayata[2], Taylor W. Kimberly[2], Matthew S. Rosen[1], Christian T. Farrar[1]*

*[1]Athinoula A. Martinos Center for Biomedical Imaging, Department of Radiology, Massachusetts General Hospital and Harvard Medical School, Charlestown, MA, USA; [2]Department of Neurology, Massachusetts General Hospital and Harvard Medical School, Charlestown, MA, USA*

**Introduction:** Magnetic resonance fingerprinting (MRF) was recently expanded and designed for CEST imaging, providing quantitative chemical exchange rate and concentration maps with scan times of a few minutes (1). In previously published CEST-MRF protocols (1,2), the saturation power and/or time was varied, while all other scan parameters were kept fixed. Although such acquisition schedules may detect CEST-related contrast, their sensitivity in mapping the water $T_1$ and $T_2$ is limited. As water relaxation errors can induce more than 20% errors in mapping CEST parameters (1), and since significant $T_1$ and $T_2$ changes occur in many pathological scenarios (e.g., tumor progression and stroke-related edema), it is highly desirable to accurately take these properties under consideration. Here we present a CEST-MRF acquisition-reconstruction workflow, capable of mapping both water relaxation times and CEST chemical exchange properties. Moreover, we demonstrate that the dictionary matching time can be significantly shortened by utilizing a Deep RecOnstruction NEtwork (DRONE) (3).

**Methods:** To obtain the optimal protocol for mutually distinguishing CEST and water relaxation contrast, a simulation study was conducted, examining 100 pseudo-random MRF acquisition schedules. Two optimal acquisition schedules were identified. The first schedule varied the saturation power and time, saturation frequency offset, repetition time, and flip angle and provided optimal T1 and T2 discrimination. The second schedule varied only the B1 saturation power and provided optimal chemical exchange parameter discrimination. The two acquisition schedules were combined and their performance was examined in an MCAO rat stroke reperfusion model on a 4.7T MRI. The devised workflow was composed of a two-step procedure. First, the water T1, T2, and amide and MT proton exchange parameters were estimated using a 4-layer, fully-connected neural network (NN) trained with a dictionary that contained a wide range of water relaxation times and chemical exchange parameters. Next, the resulting T1 and T2 values were used as additional inputs to train a CEST only NN, which was used to reconstruct more accurate exchange parameter maps from the CEST-MRF data.

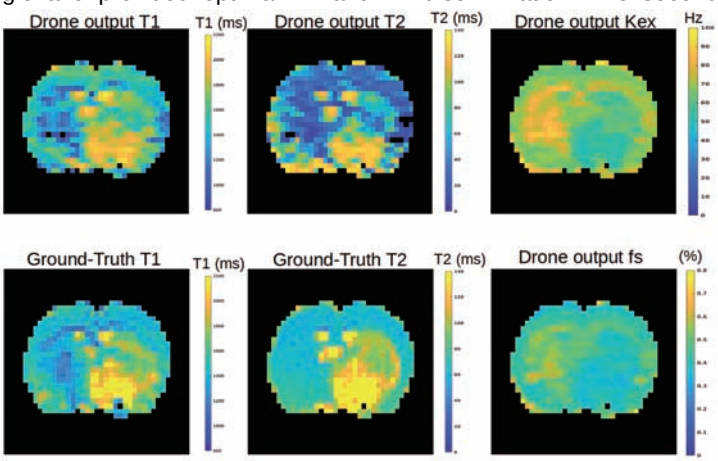



**Figure 1.** Quantitative CEST and water relaxivity parameter maps, reconstructed using the DRONE approach. The images were obtained 48h post-reperfusion, in an MCAO rat stroke model. Note the similarities between the reconstructed T1/T2 and the ground-truth maps. Decreased amide proton exchange rate and volume fraction were obtained in the ipsilesional (right-hand-side) region, as expected for this model.

**Results and Discussion:** The simulation studies showed that the combined optimal acquisition schedule for discriminating between different tissue types in terms of CEST and water relaxation data was varying saturation power and time, as well as flip angle, repetition time, and saturation frequency offsets. Shown in Figure 1, are exemplary DRONE reconstructed parameter maps of an MCAO rat stroke model, imaged 48h post-reperfusion. Decreased amide proton exchange rate ($k_{ex}$) was observed in the infarct region, consistent with decreased pH. Decreased amide proton volume fraction ($f_s$) was also observed at the same time, consistent with decreased protein/metabolite concentrations. The $T_1$ and $T_2$ maps were in good agreement with gold-standard $T_1$ and $T_2$ maps, acquired separately using saturation recovery and multi-echo protocols respectively. The total scan time for the combined acquisition schedule was 270 seconds, and the deep-neural-network based reconstruction of all 4 quantitative images took less than 100 ms.

**Conclusions:** Deep CEST fingerprinting reconstruction provides a fast method for quantitative mapping of both water proton relaxation rates as well as chemical exchange parameters for the labile proton pool of interest.

**References:**

1. Cohen O, *et al.* Magn Reson Med 2018; DOI:10.1002/mrm.27221
2. Zhou Z, et al. Magn Reson Med 2018; DOI: 10.1002/mrm.27363
3. Cohen O, Zhu B, and Rosen MS. Magn Reson Med 2018; DOI:10.1002/mrm.27198

**Ultrafast Multi-slice Chemical Exchange Saturation Transfer Imaging**

Jizhou Cai, Jian Wu, Shuhui Cai, Congbo Cai
*Department of Electronic Science, Xiamen University, Xiamen, China.*

## INTRODUCTION

Chemical exchange saturation transfer (CEST) Imaging is an important magnetic resonance molecular imaging technology. However, long acquisition time limits its clinical application, especially when 3D imaging is needed. Though single-shot EPI can be used to accelerate CEST, images may be obviously distorted under inhomogeneous fields. Spatiotemporal encoding has been utilized to surmount this problem.[1] In this work, we propose a new method called CEST-SeSPEN for ultrafast multi-slice CEST imaging based on segmented spatiotemporally encoded (SeSPEN) MRI.[2]

## METHOD

The CEST-SeSPEN sequence consists of continuous wave saturation pulse and SeSPEN acquisition module. The saturation pulse is used to produce steady CEST effect, and SeSPEN enables ultrafast and multi-slice acquisition by segmenting slice selection dimension. Experiments were performed on 7T animal MRI scanner. Different concentration creatine phantom was used and twenty slices were acquired.

## RESULTS

Typical experimental results are shown in Figure 1. It can be seen that even under a homogenous field, the CEST contrast results of all slices from CEST-EPI show more severe distortion (red arrow), while the results from CEST-SeSPEN reveal preferable shapes. Although signal loss often takes place in the fast CEST, CEST-SeSPEN effectively alleviates this situation. For CEST-EPI, the acquisition time for a single slice was 146 s, while for CEST-SeSPEN, the total acquisition time for 20 slices was 116 s.

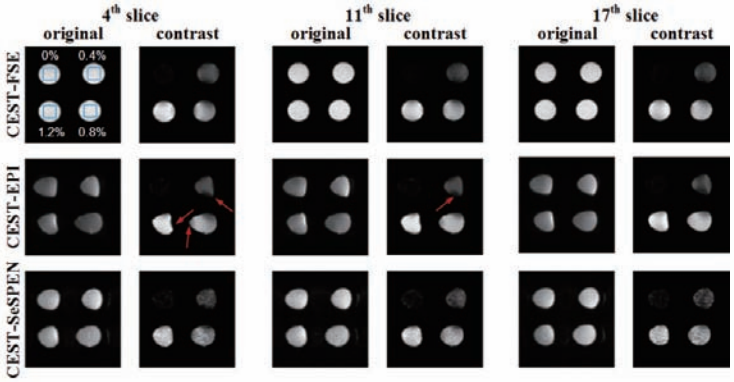



FIG. 1. Phantom images of different slices.

## DISCUSSION

The experimental results verify the feasibility of CEST-SeSPEN for ultrafast multi-slice CEST imaging. Since SeSPEN has high bandwidth in phase-encoding direction, our method is more robust to field inhomogeneity effect than CEST-EPI.

## CONCLUSION

CEST-SeSPEN can provide good CEST contrast images. It is much faster than other methods currently available. It can be used in challenging situation where high temporal resolution and robustness to field inhomogeneity are vital.

## ACKNOWLEDGMENTS

This work was supported by the National Natural Science Foundation of China under Grant 11775184.

## REFERENCES

1. Huang JP, *et al*. Magn Reson Med, 2017;77:1786-1796.
2. Zhang T, *et al*. J Magn Reson 2016;269:138-145.

## Multicolor metabolic quantitative CEST (mmqCEST): high resolution imaging of brain metabolites

Vitaliy Khlebnikov[1], Alex Bhogal[1], Mark Schuppert[2], Moritz Zaiss[2], Tobias Lindig[3], Benjamin Bender[3], Ulrike Ernemann[3], Klaus Scheffler[2,4], Peter Luijten[1], Hans Hoogduin[1], Dennis Klomp[1], and Jeanine Prompers[1]

[1]University Medical Center Utrecht, Utrecht, the Netherlands; [2]Max Planck Institute for Biological Cybernetics, Tübingen, Germany; [3]Department of Diagnostic and Interventional Neuroradiology, Eberhard-Karls University Tübingen, Tübingen, Germany; [4]Department of Biomedical Magnetic Resonance, Eberhard-Karls University Tübingen, Tübingen, Germany.

**Introduction**. The relatively low spatial resolution (ca. 250 $mm^3$) of $^1$H-MRS hinders its application towards probing heterogeneous diseased tissue, e.g. tumor tissue. Therefore, we present mmqCEST, a metabolic imaging technique based on the saturation transfer from RF-tagged metabolites to the bulk water [1]. mmqCEST decodes a frequency-dependent metabolite-weighted contrast in the Z-spectra into (multicolor) quantitative metabolic maps with a high spatial resolution (ca. 3.4 $mm^3$).

**Methods**. 3D CEST experiments were done on a 9.4T Siemens MRI platform in four healthy volunteers and one GBM (grade IV) patient. A CEST prepulse of 4.5s was repeated at four $B_1$ levels (0.6, 0,9, 1.2 and 1.6uT) for $B_1$ correction [2]. A FOV 220x180x32$mm^3$ with a voxel size of 1.5x1.5x1.8$mm^3$ was used. Other sequence details are in [3]. The patient study was approved by the local ethics committee and an informed consent was obtained from all participants. 3D $^1$H-MRS experiments were done a 7T Philips MRI platform with the following paramters: 5x5x10$mm^3$, 44x44 acq. matrix, TE/TR = 2.5/300ms, lipid suppression using external crusher coil, tailored CHESS water suppression, two slices acquired at the level of the ventricles and basal ganglia in 24 subjects. LC-model was used for quantification. CEST data were motion corrected. The calibration of Z-spectra against MRS metabolic ratios was done in the standard MNI space (1x1x1$mm^3$) by means of generalized neural networks.

**Results and Discussion**. mmqCEST has been validated in simulations, phantoms and in-vivo data. Some of the metabolic maps from healthy subjects and a GBM patient are shown in Fig. 1. In healthy subjects, $^1$H-MRS and mmqCEST demonstrate a similar contrast for all metabolites studied (Pearson correlation coefficient, R>0.95). In a GBM patient, mmqCEST revealed a hotspot in the tumor area (GPC&Cho/tCr and GSH/tCr), which is likely to be an aggressive metabolically active part of the tumor.

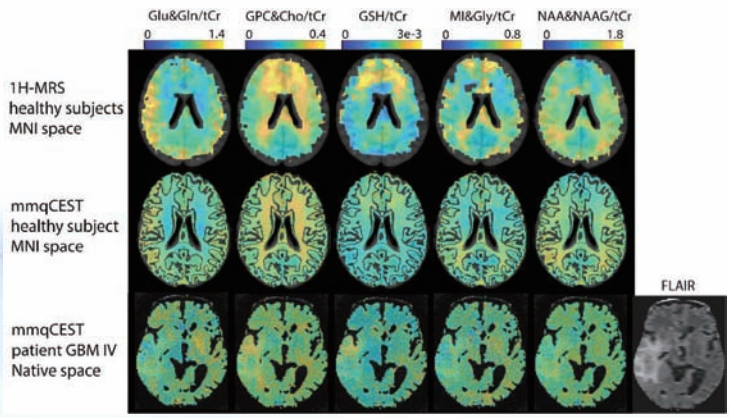



Fig. 1. Metabolic maps generated using $^1$H-MRS (1st row, averaged over 24 healthy subjects) and mmqCEST for a healthy subject (2nd row), and a GBM (grade IV) patient (3rd row). CSF was masked out.

**Conclusions**. To our knowledge, this proof-of-principle study is the first to demonstrate quantitative metabolic imaging with CEST. **References**. [1] van Zijl et al. MRM 2011; [2] Johannes J et al. NMR in Biomedicine 2015; [3] Zaiss M et al. NMR in Biomedicine. 2018.

## Temperature mapping of fat tissues by Z-Spectrum Imaging

Alessandro Scotti[1,2], Li Li[1,5], Fred Damen[1], Weiguo Li[3], Victoria Gil[4], Wenzhen Zhu[5], ChongWee Liew[4], Kejia Cai[1,2]
[1]Radiology Dept., [2]Bioengineering Dept., [3]Research Resources Center, [4]Physiology and Biophysics Dpt.; College of Medicine, University of Illinois at Chicago, IL, USA. [5]Radiology Dept., Tongji Medical College, Wuhan, Hubei, China.

**Introduction.** Temperature mapping is a fundamental need in biological research and noninvasive methods to reliably assess the variation in temperature due to pathology progression or treatment are highly required. In the MRI realm, the most widely used technique for temperature measurement is Proton Resonance Frequency (PRF), which relies on the change of water chemical shift triggered by a temperature-dependent modulation of the hydrogen's electronic shielding[1]. The measurement is often performed by tracking the change in the MR phase with respect to a reference temperature state. However, fat protons don't undergo the same change in chemical shift and the computation is therefore complicated in fatty tissues[2]. Z-spectrum imaging (ZSI) has been recently introduced as a method to quantify fat-water fraction (FWF) in brown adipose tissue, an organ with a mixed composition of lipid and water and with the capability of generating heat through cold-induced nonshivering thermogenesis[3,4]. Here we demonstrate that ZSI can also measure temperature in fatty tissues.

**Methods.** As a proof of principle, experiments were first carried out on a phantom containing heavy whipped cream having ~36% fat content. Temperature in the phantom was increased from 18 to 36 °C by regulating the warm air flow into the scanner bore. MRI was carried out at an Agilent Varian 9.4T preclinical scanner and included a CEST sequence used to acquire Z-Spectra with a 500 ms long square saturation pulse with amplitude 0.5 μT. Frequency offsets ranged dynamically from -5 to 5 ppm. The saturation pulses were followed by a single-slice fast spin echo (FSE) readout. Phase mapping was acquired for comparison by repeating a gradient echo sequence with TE=7ms and 2 averages. The reproducibility of the ZSI procedure was also tested *in vivo* on healthy male mice. Finally, the protocol was also tested on healthy subjects at a clinical 3T scanner. All Z-Spectral data were fitted to a multi-Lorentzian model including the direct saturation of water, of fat and the semi-solid MT component (**Fig.1**). Fat spectral profile was described by 5 peaks and used as internal reference for removing $B_0$-related shifts[5]. Curves amplitudes, widths and chemical shifts were loosely constrained in order to take into account inhomogeneous FWF and thermal shifting of the water resonance.

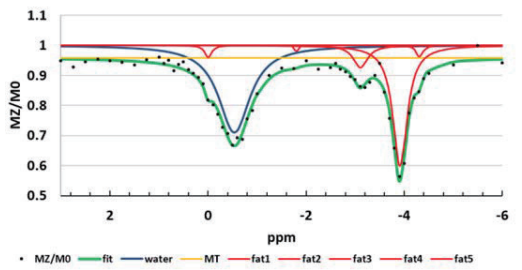



**Fig.1.** Z-spectrum from mouse brown adipose tissue. Data are fitted to a sum of Lorentzian curves representing the direct saturation of water(blue), the semi-solid MT (yellow) and fat (red).

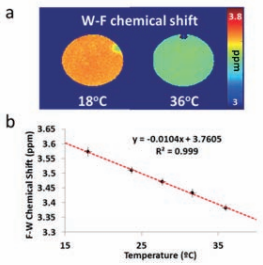



**Fig.2.** Fat-water chemical shift decrease linearly with temperature in a whipped cream phantom.

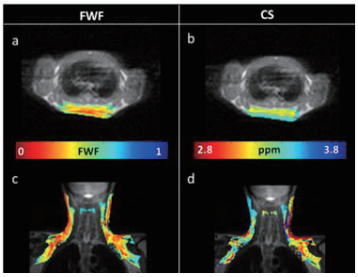



**Fig.3.** Fat-water fraction (**a,c**) and chemical shift (**b,d**) maps from interscapular and intraclavicular depots of brown adipose tissue in mice and men.

**Results.** The chemical shift detected from the cream phantom showed a homogeneous distribution throughout the phantom, independent from $B_0$ inhomogeneity (**Fig.2a**). The correlation between chemical shifts and temperature changes were assessed by a linear regression ($R^2$=0.99), with corresponding coefficient α = 0.01 (**Fig.2b**). The test-retest analysis in 5 ROIs on the mice study showed a coefficient of variation CV < 5%. Exemplary FWF and chemical shift maps from a mouse and a subject are shown in **Fig.3**.

**Conclusion.** Z-spectrum imaging can measure chemical shift and therefore temperature, exploiting the fat signal as an internal reference. Given its effectiveness in measuring also FWF, it can be an ideal technique for the study of fat metabolism, in particular the study of brown adipose tissue.

**References.** [1]Quesson, *JMRI*, 2000; [2]Soher, *MRM*, 2010; [3]Scotti, *JMRI*, 2018; [4]Liu, *NMR Biomed*, 2014; [5]Kijowski, *JMRI*, 2009.

**Acknowledgement:** This study is supported by US NIH grant R21EB023516 and China NSF grant 81401390.

**Monitoring the degradation of implanted hydrogels using CEST MRI**

Wei Zhu[1,2], Chengyan Chu[1,2], Shreyas Kuddannaya[1,2], Yue Yuan[1,2], Piotr Walczak[1,2], Anirudha Singh[3,4], Xiaolei Song[1,2], Jeff W.M. Bulte[1,2,4]

*[1]Russell H. Morgan Dept. of Radiology and Radiological Science, Division of MR Research, The Johns Hopkins University School of Medicine, Baltimore, MD, USA, [2]Cellular Imaging Section, Institute for Cell Engineering, The Johns Hopkins University School of Medicine, Baltimore, MD, USA, [3]Department of Urology, The James Buchanan Brady Urological Institute, The Johns Hopkins School of Medicine, Baltimore, MD, [4]Department of Chemical and Biomolecular Engineering, Johns Hopkins University, Baltimore, MD.*

**INTRODUCTION:** Stem cell therapy has garnered much attention for treatment of neurodegeneration. However, the harsh microenvironment at the site of damaged tissue often impairs the retention and survival of transplanted stem cells. Scaffolding cells with hydrogels is a promising strategy to overcome initial cell loss and manipulate cell function post-transplantation. While scaffold materials are essential for improving survival of cellular grafts, matrix degradation is a major requirement for functional graft integration from implanted biomaterials. [1]. Therefore, monitoring the degradation of hydrogels is essential for developing successful scaffolded stem cell therapies. We investigated whether CEST MRI can visualize implanted hydrogel scaffold degradation in mouse brain.

**METHODS:** A covalently cross-linked hydrogel composing of 20 mg/mL thiol-modified gelatin, 20 mg/mL thiol-modified hyaluronic acid (HA), and 20 mg/mL polyethylene (glycol) diacrylate (PEGDA) (crosslinker) was prepared. The ratio of gelatin to HA was varied in an effort to achieve the optimal formulation for CEST contrast. The amount of PEGDA equals 25% of the total volume of gelatin and HA. *In vitro* CEST MRI was carried out at 37 °C. For *in vivo* visualization, 3 µL hydrogel was injected into mouse striatum. CEST MRI was performed using a horizontal bore 11.7 T Bruker Avance spectrometer for up to 42 days. To validate the In vivo CEST MRI findings and identify the main decomposing component in the hydrogel, we gelatin and HA were labeled green and red near-infrared (NIR) dyes, respectively. The stained hydrogel was then visualized over time using a LI-COR optical *in vivo* imaging system.

**RESULTS AND DISCUSSION:** *In vitro* CEST MRI demonstrated a peak at 3.6 ppm for saturation field strengths from 1.2 to 7.2 µT. A value of 3.6 µT exhibited a comparable CEST signal with higher B1 values, but a less broad spectrum, and was therefore used for all further experiments. When we examined the three individual components of the hydrogel, we found that gelatin is the major contributor to the CEST signal at 3.6 ppm, in agreement with earlier studies [2]. We then increased the proportion of gelatin in the hydrogel. The increase of gelatin enhanced CEST contrast (**Fig. 1a**). When the hydrogel was injected into the brain of mice, it was clearly distinguished from the surrounding native tissue (**Fig. 1b**). This attenuation of CEST contrast indicates the feasibility of CEST MRI to monitor the degradation of hydrogel over time. The NIR signal of gelatin decrease gradually over 42 days, while the HA signal remained relatively stable (**Fig. 3c**). This suggests that gelatin, the main source of CEST signal at 3.6 ppm, is the main decomposing component in the hydrogel. An excellent correlation was found between the decay of CEST signal and gelatin NIR fluorescence signal ($R^2$=0.94, **Fig. 3d**).

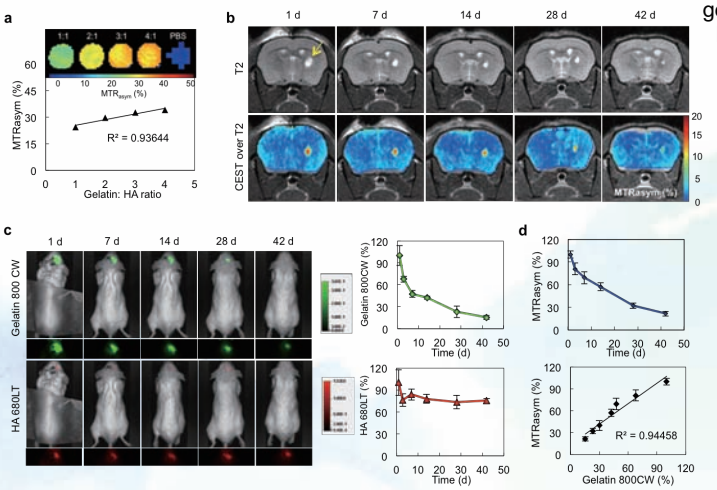



**Figure 1. (a)** CEST map of different hydrogels injected in the striatum obtained at 3.6 ppm for B1=3.6 µT. Ratios represent gelatin:HA. **(b)** T2-w CEST overlay images of 4:1 hydrogel measured at 3.6 ppm from day 1 to day 42. Arrow indicates hydrogel injection site. **(c)** Serial NIR optical images of the same mice shown in **b** and photon quantification (n=4). 800CW and 680LT correspond to labeled gelatin (green) and HA (red), respectively. (**d**) Correlation of *in vivo* CEST signal with NIR fluorescence intensity values shows an excellent correlation for gelatin ($R^2$=0.94), but not for HA ($R^2$=0.45, data not shown).

**CONCLUSION:** Hydrogel degradation can be visualized in a non-invasive and label-free manner. Gelatin was found to be the major contributor of CEST contrast and also the main degradation component in the hydrogel. This approach may be used further to develop hydrogels with optimal biodegradation properties for scaffolded stem cells.

**REFERENCES:** [1] Madl CM, *et al.* Nature Materials. 2017;16:1233. [2] Liang Y. et al. Biomaterials 2015;42:144.

## CEST MRI of brain inflammation using an aspirin metabolite as contrast agent

Xiaolei Song[1,2], Yanrong Chen[1,3], Chenwang Jin[1,2], Chengyan Chu[1,2], Irina Shats[1,2], Yuguo Li[1,2], Yue Yuan[1,2], Xiaowei He[1,3], Piotr Walczak[1,2], Jeff W.M. Bulte[1,2]

*[1]Russell H. Morgan Dept. of Radiology and Radiological Science, Division of MR Research, The Johns Hopkins University School of Medicine, [2]Cellular Imaging Section, Institute for Cell Engineering, The Johns Hopkins University School of Medicine, Baltimore, MD, USA, [3]Northwest University, Xi'an, Shaanxi 710049, China.*

**INTRODUCTION:** Sodium salicylate (NaSA), a nonsteroidal anti-inflammatory drug and main metabolite of aspirin, accumulates specifically in inflamed tissue [1], where exerts analgesic, antipyretic, and anti-inflammatory effects. We previously demonstrated that NaSA can accumulate *ex vivo* in lipopolysaccharide (LPS)-treated mouse organotypic brain slice cultures [2], and that NaSA can be detected with CEST-MRI at millimolar concentrations [3]. Here, we investigated the use of NaSA-enhanced CEST MRI for *in vivo* mapping of brain inflammation.

**METHODS:** Focal neuroinflammation was induced by a unilateral intrastriatal injection of 2 ul of 5 mg/ml lipopolysaccharide (LPS) in C57/Bl6 mice (n=8). For another group of sham mice, saline was injected instead of LPS using the same surgical procedure. 24-48 hours later, mice underwent MR scans on a 11.7 T horizontal scanner, before and after i.v. injection of 100 ul NaSA (100 mg/kg bw). A single-slice RARE sequence was used to acquire pre- and post-NaSA injection images, with a saturation frequency offset at 9.3 ppm (peak frequency for NaSA) and saturation $B_1$=5.9 uT and $T_{sat}$=2.5 sec. The dynamic NaSA-CEST signal at time-point *t* was quantified by [S(+9.3ppm, *t*)-S(+9.3ppm, 0)]/$S_0$. At the end of MRI, Gd-enhanced T1-w images were collected to verify the blood-brain-barrier (BBB) status. Post-mortem immunohistology was performed using H&E staining, microglia (anti-Iba1) staining, and anti-COX1 staining.

**RESULTS AND DISCUSSION:** For the group of inflamed mice, the dynamic NaSA-CEST images exhibit more enhancement on the LPS-injected ipsilateral sides compared to the non-injected contralateral side, with the signal increasing from ~10 min post-injection and gradually reaching a plateau after ~30-45 min (**Fig 1A, C**). While the T2w image showed signs of hemorrhage and edema and post-Gd T1w indicated areas of a disrupted BBB, the NaSA-CEST images fom 15 to 45 min were found to highlight regions similar to the distribution of Iba1$^+$ activated microglia (**Fig. 1A**). In contrast, sham mice showed much lower NaSA-CEST signal than those in the inflamed group, indicating no inflammation as validated by immunohistology (**Fig. 1B**). Dynamic NaSA-CEST signals for both groups showed an increased signal at the ipsilateral enhanced region, suggestin g the accumulation of NaSA at the inflammation sites (**Fig. 1C**). Z-spectra differences between pre-injection and ~40min post-injection of NaSA further validated the observed peaks at ~9.3-9.6 ppm (**Fig. 1D**). When comparing the NaSA-CEST signals with immunohistology for five different brain regions (enhanced region, cortex and striatum in the LPS-injected side and their mirrored contralateral regions), both COX1 and Iba1 intensity correlated to the NaSA-CEST signal, with the latter showing a higher $R^2$ (**Fig. 1E**).

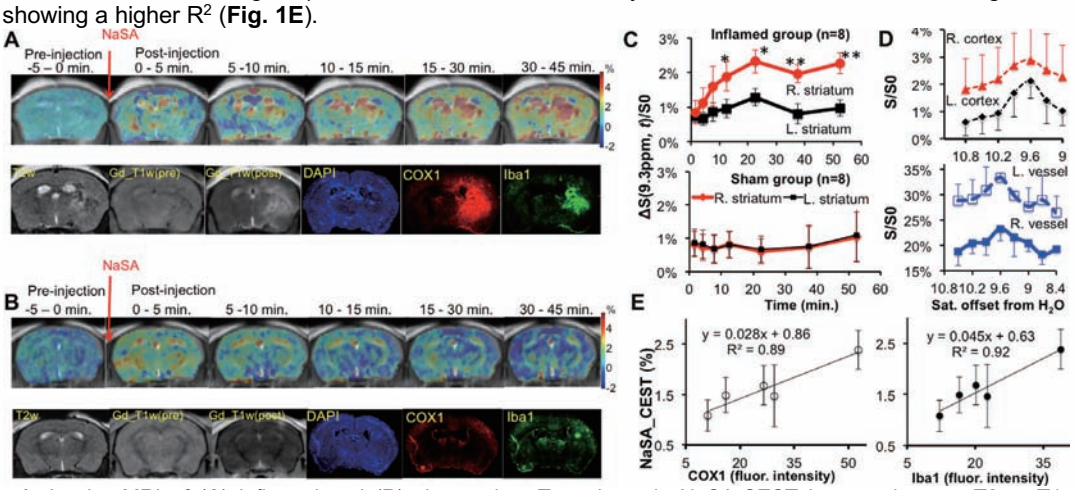



**Figure 1.** *In vivo* MRI of (**A**) inflamed and (**B**) sham mice. Top: dynamic NaSA-CEST images, bottom: T2-w, T1-w and histological images. (**C**) CEST signal as a function of time post-injection of NASA (mean±SEM, *p<0.05, **p<0.01). (**D**) ΔZspectra (n=4). (**E**) Correlation between NaSA-CEST and fluorescence intensity of staining for COX1 (left) and Iba1 (right).

**CONCLUSION**: NaSA-CEST MRI shows specific signal enhancement in the inflamed LPS-injected hemisphere, which was not observed in sham control mice, indicating that NaSA-CEST MRI could be used as a new platform for imaging of neuroinflammation.

**REFERENCES:** [1] Rainsford, K.D. et al., Arch. Int. Pharmacodyn. 1981;250:180. [2] Schaffhauser M. et al., WMIC 2016. New York City, P2493111 [3] Song X. et al., J. Cereb. Blood Flow Metab. 2016;36:1186.

## Acidosis imaging of skeletal muscles by chemical exchange saturation transfer (CEST) imaging

Dennis W. Hwang

*Institute of Biomedical Sciences, Academia Sinica, Taipei, Taiwan*

**INTRODUCTION:**

pH value variation has been investigated in the disease lesion regions, such as tumors, stroke and muscle injury. However, to image the change of pH level is a challenge. CEST imaging is one of the possible methods to overcome this problem. CEST can efficiently enhance the contrast for small pH variation between solute and water proton by saturation transfer. In this study, fatigue skeletal muscles model of mice by electrical stimulation was investigated.

**METHODS:**

Two mice models are used, muscle injected with acid buffer and Muscle fatigue model. In the 1st model, male wild-type C57BL/6JNarl mice were used in the muscle acidosis experiment. The right side of gastrocnemius muscle was injected with 20 µl of pH 4.0 MES buffer (10 mM), and the left side was injected with pH 7.4 HEPES buffer (20 mM). For the 2nd model, the needle electrodes were implanted in the proximal portion of the bilateral gastrocnemius muscle of mice and the legs were straightened during electrical stimulation.

All images were acquired with a Bruker 7 T MRI Scanner outfitter with an 16-mm-bore. A $T_2$-weighted imaging (T2WI) and CEST sequence was used to acquire anatomical images for pH analysis with the following parameters: a repetition time (TR) of 2000 ms, an effective echo time (TE) of 56 ms, a RARE factor of 8, a field-of-view (FOV) of 3.5 cm, an acquisition matrix of 256 x 128, a resolution of 0.014x 0.027 cm/pixel.

**RESULTS and DISCUSSION:**

The z-spectra show significant enhancement between the off-resonance frequency of -1 ppm to -2 ppm. CEST images also present a noteworthy contrast in the lesion region while $T_2$ weighed images display a larger lesion which may be due to the temporary increasing blood flow. The pH value in the lesion is believed to be between 6 to 7. According to the magnetic resonance spectroscopy (MRS), main metabolites in the skeletal muscles is creatine. The acidic environment may enhance the proton exchange between water protons and protons on creatine through NOE effect.

**CONCLUSION:**

The detailed chemical compositions and acidity in MR images are still needed to be quantified. It will be correlated with fMRI data to differentiate the sensory pain and soreness.

**Combining GlucoCEST and pH imaging for an improved characterization of tumor metabolism**

Longo D, Anemone A, Capozza M, Bardini P, Arena A, Marini G, Zullino S, Terreno E, Aime S
*Molecular Imaging Center, Department of Molecular Biotechnology and Health Sciences, University of Torino, Via Nizza 52, Torino, ITALY*

**INTRODUCTION:** The majority of cancer cells exhibit increased glucose uptake with a consequent decrease of extracellular pH, an established hallmark of tumor microenvironment[1]. Diagnosis in clinical oncology exploits the elevated glucose uptake of tumors by using Position Emission Tomography (PET) in combination with $^{18}$F-FDG. However, the main issues with $^{18}$F-FDG-PET are its associated radioactivity, cost and availability. For this reason, the development of radiation-free MRI methods based on the CEST technique for the assessment of tumour metabolism has attracted the interest of the medical community. GlucoCEST has been recently proposed for investigating tumour metabolism following the injection of glucose [2]. In addition, our group has proposed pH imaging for monitoring the subsequent acidification of the tumour extracellular-extravascular space (pHe) [3].
Here we investigated the different metabolic properties of two tumour murine models by combining MRI-based GlucoCEST and pHe imaging. The obtained results were compared with the $^{18}$F-FDG-PET uptake.
**METHODS:** 4T1 (mouse mammary carcinoma) and PC3 (human prostate cancer) cells were subcutaneously implanted in both flanks of female BALB/c and male Athymic Nude-Foxn1$^{nu}$ mice, respectively. CEST MRI protocol was performed on a Bruker 7T MRI scanner. Each mouse underwent glucose i.v. injection at dose 5g/kg followed by Iopamidol injection (4gI/Kg) 30 min later. Z-spectra before and after contrast media injections were acquired and CEST contrast was calculated between POST and PRE images. Two days after the MRI acquisition mice were kept fasted overnight injected with $^{18}$F-FDG for PET imaging.
**RESULTS:** As reported in Figure 1, CEST analysis revealed that the PC3 tumour model displayed a lower GlucoCEST contrast in comparison to the 4T1 one (glucose ΔST% = 3.0 and 2.5 for 4T1 and PC3, respectively). Moreover, 4T1 tumour model presented a more acidic pHe than the PC3 model (mean pHe value of 6.7 and 6.8 for 4T1 and PC3, respectively, P<0.05). The evaluation of $^{18}$F-FDG-PET in the tumor model showed a significantly higher uptake in 4T1 (SUV: 0.62, %ID/cc: 3.23) tumours than in PC3 tumours (SUV: 0.32, %ID/cc: 1.15).
**DISCUSSION:** The two tumour models showed a marked different FDG uptake that was lower for the prostate one. Noteworthy, the GlucoCEST signal was also lower in PC3 compared to the 4T1 breast tumour model. Consistently with the higher glucose uptake, the measured tumour extracellular pH was lower in 4T1 compared to PC3, showing an increased tumour acidosis.
**CONCLUSION:** These findings highlight a good characterization of the tumour metabolism by exploiting complimentary MRI-CEST approaches in comparison to PET imaging. Further investigations are needed to better understand the specific metabolic pathways leading to the different glucose uptake and extracellular acidification between the two tumour murine models.

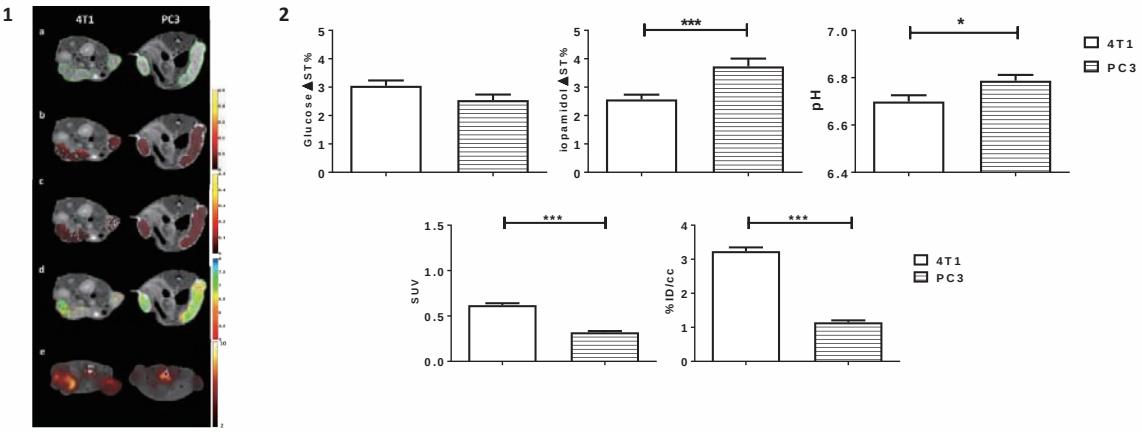



**Figure 1**: a, Anatomical $T_{2w}$ images of representative 4T1 and PC3 tumour bearing mice. b, Representative GlucoCEST map obtained after i.v. injection of D-glucose, 5 g/kg (Data are reported as the difference, ΔST %, between the ST% before and after the iv injection). c, Representative contrast enhanced maps upon i.v. injection of iopamidol as MRI-CEST ΔST% maps. d, pH map overimposed on the anatomical image of each tumour model. e, Fused PET/CT axial view images of representative B16-F10, 4T1 and PC3 tumour bearing mice injected with 18F-FDG. Data are expressed as % ID/cc.
**Figure 2**: Average values calculated for each tumor model of a, GlucoCEST contrast b) Tumor extracellular pH, c $^{18}$F-FDG PET uptake reported as standardized uptake values (SUV). Bar graphs show mean ± SD. *: P <0.05, ***: P<0.0001.

**ACKNOWLEDGMENTS:** European Union's Horizon 2020 research and innovation programme under grant agreement No 667510 (GLINT project).
**REFERENCES:**
1. Robey IF, et al. Cancer research. 2009, 69, 2260
2. van Zijl PC, et al. Magn Reson Med. 2012, 68, 1764; Golay X. et al; Nat Med. 2013, 19, 1067
3. Longo DL, et al.; Cancer Research 2016, 76, 6463

**GluCEST MRI and Glutamatergic System Dysregulation**

*Ravinder Reddy, PhD*
*Center for Magnetic Resonance and Optical Imaging (CMROI), Perelman School of Medicine, Department of Radiology, University of Pennsylvania, Philadelphia, PA 19104*

Glutamatergic system is a fast-signaling system of the brain that enables cells to transmit and receive the excitatory neurotransmitter glutamate. It is crucial for information processing in neuronal networks and plays a key role in the induction and maintenance of long-term potentiation (LTP), and hence the regulation of learning and memory [1]. Dysregulation of glutamatergic system has been linked to disruptions in glutamine-glutamate cycling [2] and glutamate synaptic transmission that can result in excitotoxicity through different routes including stimulation of glutamate release from neurons and astrocytes, inhibition of glutamate uptake, and causing abnormally high extracellular levels of glutamate which alter signaling pathways related to activation of glutamatergic receptors, and eventual loss of neurons. In addition to neurotransmission, glutamate molecule acts as a metabolic intermediate and plays an essential role in synapse formation, dendrite pruning, cell migration, differentiation, and death and is primarily synthesized from glucose through TCA cycle and through recycling of glutamate by the glutamine-glutamate cycle [3]. Glutamate excitotoxicity, has been implicated in many central nervous system (CNS) disorders including acute disorders such as epileptic seizures and traumatic brain injury and in chronic disorders such as Alzheimer's disease (AD), Parkinson's disease (PD), Huntington disease (HD) and amyotrophic lateral sclerosis (ALS) [4]. Taken together, these data suggest that changes in the glutamatergic system, hence in glutamate, potentially serve as a target for understanding the pathogenesis of many CNS disorder and for the development of both early biomarkers as well as disease-modifying therapies. While $^{1}$HMRS is used to measure glutamate in vivo, it is limited by poor spatial resolution.

Glutamate chemical exchange saturation transfer (GluCEST) is a high-resolution MRI method that provides glutamate weighted contrast, which depends both on glutamate concentration and pH[5]. Despite being not fully specific to glutamate in the brain, the method has shown promising results in measuring imaging contrast due to glutamate-mediated changes in preclinical models of AD [6,7], PD [8,9] and in patients with Epilepsy [10] and Schizophrenia [11].

This presentation will begin with a brief outline of the technical requirements, sensitivity advantages and recent optimizations of the GluCEST method as applied to in vivo systems. Then, emerging applications of GluCEST MRI in studying neurodegenerative diseases, epilepsy, and schizophrenia will be presented. The talk will conclude with a summary of advantages and potential challenges of GluCEST MRI in quantifying the glutamate contrast under *in vivo* environments.

**References**

[1] S. Peng, Y. Zhang, J. Zhang, H. Wang, and B. Ren, Mol Biol Rep **38**, 453 (2011).
[2] M. Popoli, Z. Yan, B. S. McEwen, and G. Sanacora, Nat Rev Neurosci **13**, 22 (2011).
[3] N. Agarwal and P. F. Renshaw, AJNR Am J Neuroradiol (2011).
[4] M. P. Mattson, Neuromolecular Med **3**, 65 (2003).
[5] K. Cai *et al.*, Nat Med **18**, 302 (2012).
[6] R. Crescenzi *et al.*, Neuroimage **101**, 185 (2014).
[7] M. Haris *et al.*, NMR Biomed (2012).
[8] P. Bagga *et al.*, J Neurochem **139**, 432 (2016).
[9] P. Bagga *et al.*, Sci Rep **8**, 2883 (2018).
[10] K. A. Davis *et al.*, Sci Transl Med **7**, 309ra161 (2015).
[11] D. R. Roalf *et al.*, Mol Psychiatry (2017).

**Acknowledgements**: This work was supported by NIH grants from NIBIB (P41EB015893S1, P41EB015893) and NINDS (R01NS087516).

## Machine learning with protein-based MRI for predicting IDH1/2 mutation status in diffuse gliomas

Shanshan Jiang
*Department of Radiology, Johns Hopkins University, Baltimore, MD, USA*

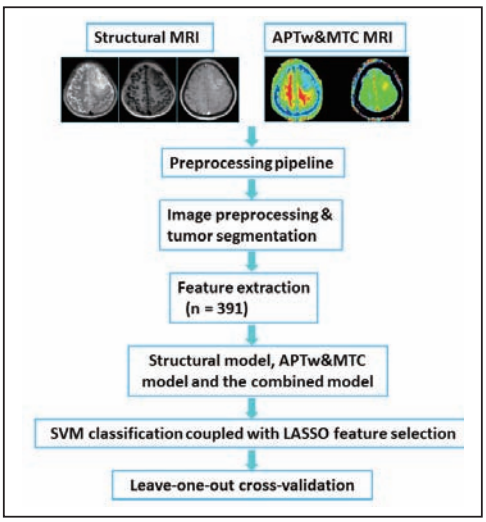
**INTRODUCTION:** The updated 2016 WHO guideline for CNS tumor classification suggests isocitrate dehydrogenase (IDH) mutation status, in addition to histology, to define tumor entities in patients with diffuse gliomas[1,2]. It reveals an unmet radiographic need—the ability to identify genetic biomarkers preoperatively, with invasive methods such as MRI. Amide proton transfer-weighted (APTw) and magnetization transfer (MT) imaging were used to generate contrast dominated by endogenous mobile proteins and semi-solid macromolecules[3]. The goal of this study was to evaluate the power of machine learning using APTw and MTC MRI features in classification for IDH1/2 mutation status in grade II and III gliomas.

**METHODS:**
A total of 105 patients with pathologic confirmed WHO grade II and III gliomas and IDH1/2 mutation status were enrolled. Pre-surgery T1w, T2w, FLAIR, APTw, MTC, and T1w-Gd MR images were collected. APTw images were calculated using the magnetization transfer ratio asymmetry at 3.5ppm[3]. The processing workflow is presented in **Fig. 1.** 391 radiomics features[4] on APTw, MTC and structural MR images were extracted from the tumor ROIs. The support vector machine (SVM) models were built on structural MRI, APTw & MTC MRI and the combined based features, separately. 70 cases were randomly assigned to training set, 25 cases to validation set, and 10 cases to test set. 10-fold cross-validation was used to evaluate the accuracy of the test sets.

**RESULTS:**
The SVM model achieved accuracies of 80.7%, 85.1%, and 89.4% for the structural MRI, the APTw & MTC MRI and the combined models, separately. Features exacted from APTw and MTC MR images combined with age and WHO grade yielded the highest classification performance in IDH genotype.

**DISCUSSION:**
This study represented the first analysis of the ability to use APTw and MTC MRI radiomics to classify IDH1/2 mutation status in grade-II and -III gliomas. Since IDH-gene-encoded enzymes are closely involved in the energy-producing Krebs cycle as catalytic isozymes, mutations in IDH genes may cause widespread disturbances of cellular metabolism, including alteration of amino acid concentrations and enzymatic activity, and raise global DNA hypermethylation and global downregulation of protein expression as well[5].

**CONCLUSION:**
The findings support that the use of textures extracted from APTw and MTC MRI aids the accurate diagnostic classification of IDH genotype.




**ACKNOWLEDGMENTS:**
We thank Jinyuan Zhou, Zhibo Wen, Charles Eberhart, Hye-Young Heo, Qihong Rui, Hao Yu, Peter C.M. van Zijl for the contributions to this project.
NIH: R01EB009731, R01CA166171, R01CA228188, R01 EB015032, P41EB015909.
NSFC: 81171322

**REFERENCES:**

1 Louis, D. N. *et al. Acta Neuropathol.* **131**, 803-820, (2016).
2 Yan, H. *et al. N. Engl. J. Med.* **360**, 765-773, (2009).
3 Zhou, J. et al. *Nature Med.* **9**, 1085-1090, (2003).
4 Aerts, H. J. W. L. *et al. Nat Commun* **5**, (2014).
5 Doll, S. *et al. Mol Cell Proteomics* **16**, 39-56, (2017).

## CEST Imaging of Parkinson's Disease

Chunmei Li[1], Jinyuan Zhou[2], Haibo Chen[3], Min Chen[1]
[1]*Department of Radiology, Beijing Hospital, the National Center of Gerontology, Beijing, China*
[2]*Department of Radiology, Johns Hopkins University, Baltimore, Maryland, USA*
[3]*Department of Neurology, Beijing Hospital, the National Center of Gerontology, Beijing, China*

**INTRODUCTION:**

To assess the clinical value of chemical exchange saturation transfer (CEST) imaging in the detection and disease severity evaluation of Parkinson's disease (PD) at a standard clinical 3T MRI system.

**METHODS:**

CEST MR images of 24 normal controls and 61 idiopathic PD patients were acquired. Magnetization transfer spectra with 31 different frequency offsets (-6 to 6 ppm) were acquired at two transverse slices of the head, including the basal ganglia and midbrain. The CEST signal intensities (including amide proton transfer-weighted or APTw, and total CEST or $CEST_{total}$) of five regions (substantia nigra, red nucleus, globus pallidus, putamen, and caudate of both hemispheres) were measured. Analysis of variance post-hoc tests was used to compare the CEST MRI signal differences between normal controls and PD patients. Correlation analysis was made for the CEST signal of substantia nigra and the severity of disease and disease duration.

**RESULTS:**

The APTw and $CEST_{total}$ in the substantia nigra were significantly lower in PD patients than in normal controls ($P < 0.05$). The APTw in the globus pallidus, putamen, and caudate were significantly increased in PD patients, compared to normal controls ($P < 0.05$). The APTw and $CEST_{total}$ of the substantia nigra in PD patients showed a significantly decreased tendency with PD progression. Both the APTw and $CEST_{total}$ values of PD were significantly correlated with the severity of disease and disease duration.

**DISCUSSION:**

The $MTR_{asym}$(3.5ppm) signal intensities of the globus pallidus, the putamen, and the caudate were higher in PD patients than in normal controls may be associated with increased cytosolic proteins and peptides, as expected (1,2) In contrast, the substantia nigra showed significantly lower total CEST signal intensities in PD patients than in normal controls, which could be attributed to the loss of dopaminergic neurons that may lead to the loss of all water-exchanging chemicals. The progressively reduced CEST signal of the substantia nigra may be ascribed to the gradually decreased dopaminergic cell density in the substantia nigra, which are reflected by the worsening condition of PD patients.

**CONCLUSION:**

CEST imaging signals could potentially serve as imaging biomarkers to aid in the non-invasive molecular diagnosis and disease severity evaluation of PD.

**ACKNOWLEDGMENTS:**

This study was supported by the National Natural Science Foundation of China (81401404 and 81361120392), Beijing Natural Science Foundation (7154235), and the National Institutes of Health (R01EB009731, R01CA166171, and R01NS083425).

**REFERENCES:**

1. Braak H, *et al*. Neurosci Lett 1999;265:67-69.
2. Tong JC, *et al*. Brain 2010;133:172-188.

**CrCEST in the study of creatine metabolism kinetics in Peripheral Arterial Disease**

Helen Sporkin[1], Roshin Mathew[2], Christopher Kramer[2,3], Craig Meyer[1,3]
[1]*University of Virginia, Biomedical Engineering, Charlottesville, Virginia, USA*
[2]*University of Virginia, Cardiac Imaging, Charlottesville, Virginia, USA*
[3]*University of Virginia, Radiology and Medical Imaging, Charlottesville, Virginia, USA*

**INTRODUCTION:** Peripheral arterial disease (PAD) is an atherosclerotic disease characterized by distal artery obstruction leading to lower limb ischemia and resultant claudication. PAD affects over 200 million people globally. The current standard PAD imaging method, $^{31}$P magnetic resonance spectroscopy (MRS), suffers from three orders of magnitude lower signal than CrCEST and cannot be performed with standard proton coils. Creatine chemical exchange saturation transfer (CrCEST) MRI involves selectively saturating creatine-bound protons that are then transferred to free water as creatine metabolism occurs. It can directly image muscle energetics with proton coils. We propose that CrCEST is sufficiently sensitive and fast to distinguish differences in creatine kinetics between PAD patients and aged matched controls.

**METHODS:** We have applied CrCEST in 16 healthy subjects and 5 PAD patients who performed plantarflexion ergometry to exhaustion or claudication. Creatine levels were measured over 8-10 min using a pulse sequence from collaborators at the the Center for MR and Optical Imaging at the University of Pennsylvania in a Siemens 3T Prisma.[1] Water saturation with shift reference (WASSR) and B1 maps were collected for B0 and B1 correction. Six images were acquired over 24 s intervals with saturation frequency offsets of ±1.3, ±1.8, and ±2.3 ppm. The CEST effect from creatine reduces the signal at +1.8 ppm compared to the reference at -1.8ppm, referred to as $CrCEST_{asym}$. A 500 ms saturation pulse train was applied consisting of five 99.6 ms Hanning-windowed pulses with 150 Hz B1 amplitude separated by a 0.4 ms inter-pulse delay. A fat saturation pulse was applied, followed by a single-shot spoiled gradient-echo readout with centric encoding, flip angle 10°, FOV 160x160 mm, matrix 128x128, TR 6.0 ms, TE 3 ms, slice thickness 10mm. An ROI containing the anterior, lateral, and superficial compartments of the calf was drawn by hand for each subject. Values of the mean $CrCEST_{asym}$ signal of the ROI at each acquisition time were fit to a monoexponential with a decay constant $\tau$.

**RESULTS:** Of the 16 healthy volunteers scanned, 3 were excluded due to failure to reach exhaustion within 20 minutes of plantarflexion exercise. The mean $\tau$ of the 13 successful in-bore exercise volunteers was 173.4 ± 50.0 s. All 5 PAD patients were able to reach exhaustion, but had prolonged decays that were not well defined by an exponential. Additionally, all normal decays had a peak $CrCEST_{asym}$ signal at the initial post-exercise time point, while all PAD patients had higher following values or subsequent concentration rises before overall decay was seen. An example is shown in Figure 1.

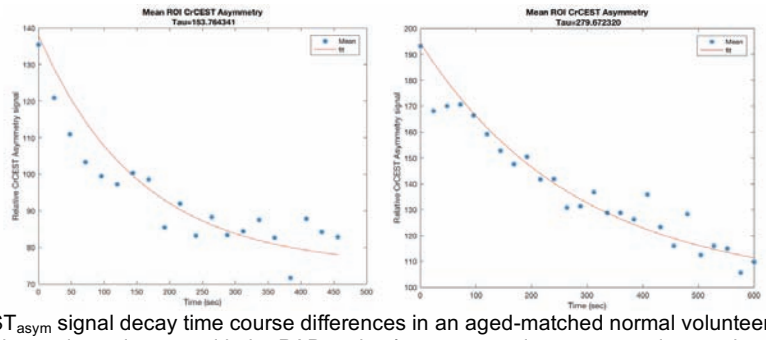



Figure 1: $CrCEST_{asym}$ signal decay time course differences in an aged-matched normal volunteer (right) and a PAD patient (left). A slower decay is seen with the PAD patient's mean creatine concentration as shown by $CrCEST_{asym}$.

**DISCUSSION:** Normal volunteer time course data appears to be well described by a monoexponential, while our PAD data so far shows longer and more variable decay shapes. The long decay constant seen in Figure 1 is indicative of fitting an exponential to non exponential data. Further investigation with this study and subsequent imaging studies are necessary to make firm conclusions from these findings.

**CONCLUSION:** CrCEST is emerging as a useful imaging tool in evaluating metabolism and distinguishing disease from normal function in patients with PAD. Further characterization of PAD with CrCEST may lead to more insight into the metabolic effects of ischemia beyond what is possible with $^{31}$P spectroscopy.

**REFERENCE:**1. Haris M, *et al.* Nature Med 2014; 20,2:209-215.

**Dynamic Glucose-Enhanced Imaging of Mouse Brain with Alzheimer's Disease at 3T MRI**

Jianpan Huang[1], Jiadi Xu[2], Ed. X. Wu[3], Peter C.M. van Zijl[2], Kannie W.Y. Chan[1,2*]

*[1]Department of Biomedical Engineering, City University of Hong Kong, Hong Kong, China*

*[2]Russell H. Morgan Department of Radiology and Radiological Science, Johns Hopkins Medicine, USA*

*[3]Department of Electrical and Electronic Engineering, University of Hong Kong, Hong Kong, China.*

**Introduction**

We and others have demonstrated that glucoCEST[1] or dynamic glucose enhancement (DGE) [2] are capable of detecting glucose uptake and perfusion-related parameters in tumors[3]. However, the current DGE studies are mainly performed at high magnetic fields (≥7T), which hampers a wide application of DGE for routine clinical applications. At the lower MRI fields (3T), acquisition parameters and contributions to the DGE signal can be quite different from those at high field. Here, we aim to characterize glucoCEST or DGE on a 3T animal scanner. We are interested in applying it for the glucose uptake study on a Alzheimer's disease (AD) model, since regional glucose hypometabolism has been found to be one of the early hallmarks of AD[4]. Hence, findings from current study have the potential to assist the diagnosis of AD.

**Methods**

Experiments were carried out on 18-month-old 5xFAD mouse (n=3) and age-matched WT mouse (n=3). MRI acquisition of DGE was performed on a horizontal bore 3T animal scanner (Bruker BioSpec) equipped with a mouse brain surface coil. A continuous wave saturation was applied with a saturation power of 0.4uT and a saturation length of 1s. Images was collected with RARE sequence. DGE images and dynamic curves were acquired by saturating at 1.2 ppm. The formal acquisition scheme is shown in Fig. 1(a). DGE curve and area-under-curve (AUC) values were calculated to evaluate the results quantitatively[3].

**Results**

We can see from Fig. 1(b) and (c) that AD mouse brain showed an apparent lower averaged glucoCEST signal compared to WT (not obvious in T2 weighted images). This result indicates that the glucose uptake in the AD mouse brain was much less than normal brain. The glucose uptake difference can also be seen in the DGE curve shown in Fig. 1(d). After glucose injection, both WT and AD showed a rapid enhancement, while the glucoCEST effect for AD is lower than WT. About 10 minutes later, both curves reached a steady state. Fig. 1(e) shows the regional glucose uptake comparison by calculating AUC values of DGE in the first 5 minutes (build-up period) after glucose injection, the contrast was consistently lower in the studied regions in AD mice. The thalamus was the region with highest AUC compared to cortex and hippocampus in both types of mice.

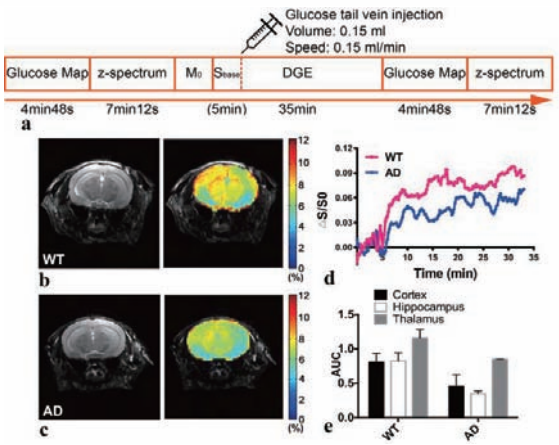



Fig. 1. (a) Flowchart of the glucoCEST study for AD and WT mouse brain. (b), (c) T2 weighted images and glucose enhancing images overlapping on them. (d) DGE curve comparison. (e) Regional AUC values comparison.

**Discussion**

The preliminary results clearly indicated that AD mouse brain had a lower glucoCEST contrast compared to WT mouse, and importantly the regional differences resemble the glucose related neuropathology in AD[4]. The DGE dynamic curves acquired at 3T MRI are very different from those recorded at high fields, where the DGE curves decay rapidly after the initial build up[3]. Hence, further study is necessary to confirm the effects contributing to the DGE signal in addition to the glucoCEST.

**Conclusion**

Dynamic glucoCEST imaging is capable to detect differences in the regional glucose between AD and WT mouse brain at 3T. This encouraging preliminary data demonstrates the possibility of diagnosis AD by glucoCEST at clinical field strength.

**Acknowledgement**

This work was supported by CityU 9610362, 7200516 and 6000612.

**References**

1. Chan, K.W.Y. *et al*. Magn Reson Med 2012;68: 1764-1773; Walker-Samuel, S. *et al.* Nat Med 2013;19: 1067-1072.; 2. Xu. X. *et al*. ISMRM proceedings 2018 #1662.; 3. Xu, X. *et al.* Magn Reson Med 2015;74: 1556-1563; Xu, X. et al. Schuenke, P. *et al*. Sci Rep 2017; #42093.; 4. Luo, F. *et al.* Neurobiol Aging 2012;33: 933-944; Macdonald, I. *et al.* Curr Alzheimer Res 2014;11: 450-460.

## APT imaging in cancer clinical practice

Osamu Togao[1]
[1] *Department of Clinical Radiology, Graduate School of Medical Sciences, Kyushu University, Fukuoka, Japan*

**Introduction:** APT imaging has been developed as one of the endogenous CEST imaging techniques by the group of Drs. Zhou and van Zijl in 2003 [1]. This method exploits the exchange between protons of bulk-water and the amide protons (-NH) of endogenous mobile proteins and peptides in tissue. Amide protons have a chemical shift of 3.5 ppm down field from bulk water corresponding to 8.3 ppm in the NRM spectrum. APT imaging can be implemented on a clinical 3T scanner because of the slow exchange rate and relatively large chemical shift of amide protons. In this session, we would like to review some results in which APT imaging was useful in characterizing and differentiating various types of tumor.

**Results and literature review:** We previously reported that that APT imaging can differentiate low-grade from high-grade glioma with a high sensitivity and specificity [2]. The mean APT-w signal intensity (SI) were 2.1 ± 0.4% in grade II gliomas, 3.2 ± 0.9% in grade III gliomas, and 4.1 ± 1.0% in grade IV gliomas. Significant differences in APT intensity were observed between grades II and III and grades III and IV, as well as between grades II and IV. There were positive correlations between APT SI and Ki-67 LI ($P < .01$, $R = 0.43$) and between APT-w SI and cell density ($P < .05$, $R = 0.38$). We also reported that APT imaging has high diagnostic performance in differentiating HGG from LGG in non-enhancing gliomas [3]. The $APT_{90}$ (2.80 ± 0.59 % in LGGs, 3.72 ± 0.89 in HGGs, $P = 0.001$) and $APT_{mean}$ (1.87 ± 0.49 % in LGGs, 2.70 ± 0.58 in HGGs, $P = 0.0001$) were significantly larger in the HGGs compared to the LGGs. The ADC and rCBV values were not significantly different between the groups. Both the $APT_{90}$ and $APT_{mean}$ showed medium diagnostic performance in this discrimination.

It was also reported that APT imaging was useful in other types of brain tumor. Kamimura et. demonstrated using a histogram analysis that APT-w SIs of enhancing areas in glioblastoma were significantly higher than those of brain metastasis, and APT imaging showed a high diagnostic performance (AUC 0.70-0.85) in this differentiation. Jiang et al. reported that primary central nervous system lymphomas (PCNSLs) showed more homogeneous APT-w SI than HGGs. The APT-w max, APT-w max-min and CEST total signal intensities were significantly lower ($P < 0.05$, 0.001 and 0.05, respectively), while the APT-w min and MTR were significantly higher (both $P < 0.01$) in PCNSL lesions than in HGG lesions [4]. Joo et al. reported that atypical meningiomas exhibited significantly higher APT-w SIs than benign meningiomas. The discriminative value of conventional MRI improved significantly when combined with APT imaging for diagnosis of atypical meningioma [5].

APT imaging can be useful in characterizing and assessing malignancy of extracranial tumors. We previously reported that APT imaging could predict histologic grades of uterine endometrioid endometrial adenocarcinomas (EEA) [6]. The average APT-w SIs were 2.2% ± 0.2 for grade 1; 3.2% ± 0.3 for grade 2; and 3.7% ± 0.3 for grade 3, respectively. The APT-w SIs of grade 3 EEA were significantly higher than those of grade 1 EEA. Takumi et al. reported that APT imaging could differentiate malignant from benign head and neck tumors. Malignant tumors showed higher APT-w signal (2.50 ± 0.72%) than benign tumors (1.76 ± 1.15%).

**Conclusion:** APT imaging is useful in characterizing and differentiating various types of brain tumors as well as extracranial tumors.

**Acknowledgements:** We would like to thank Drs. Yoshiura, Takumi, and Kamimura for providing the clinical data in Kagoshima University, Japan.

**References:**

1. Zhou J, et al. *Nat Med* 2003;9:1085-1090
2. Togao O, et al. *Neuro Oncol* 2014;16:441-448
3. Togao O, et al. *Eur Radiol* 2017;27:578-588
4. Jiang S, et al. *Eur Radiol* 2016;26:64-71
5. Joo B, et al. *Eur Radiol* 2018;28:331-339
6. Takayama Y, et al. *Radiology* 2018;286:909-917

# Predicting Response to Antiangiogenic Treatment for Recurrent GBM Using Amide Proton Transfer-Weighted MR Imaging: Initial Experience

Qihong Rui[1], Hao Yu[1], Xianglong Wang[1], Fanheng Huang[1], Jing Li[1], Shanshan Jiang[2], Jinyuan Zhou[2], Zhibo Wen[1]

1. *Department of Radiology, Zhujiang Hospital, Southern Medical University, Guangzhou, Guangdong Province, China*
2. *Department of Radiology, Johns Hopkins University, Baltimore, MD, USA*

**INTRODUCTION:** Target therapy, especially antiangiogenic therapy, is still the key way to prolong the survival or improve the quality of life. However, not all types of GBM respond to bevacizumab regimen therapy. Currently, on the basis of clinical and imaging criteria, it remains impossible to prospectively predict which patient will respond to such therapy. So, it is urgent to seek a non-invasive imaging modality which can predict response to bevacizumb prior to treatment.

Amide proton transfer-weighted (APTw) MR imaging is a new endogenous molecular imaging technique based on chemical exchange-dependent saturation transfer (CEST). Our previous studies have demonstrated that the intensity of APTw-MR imaging closely relate to cellularity, angiogenesis of glioma. Therefore, APTw-MR imaging may have the potential to reflect the tumor response after target therapy. In this study, we will compare the imaging features and signal intensity changes for recurrent GBM before and after treatment, and determine if APTw value can predict which kind of GBM have a good response prior to treatment with bevacizumb.

**METHODS:** This study was approved by the institutional review board and informed consent was obtained. 15 patients (12 men, 3 women; mean age, 45.3±10.2 [standard deviation]) with recurrent GBM received bevacizumb every 3 weeks (15 mg per kilogram of body weight). Baseline MR Images were acquired, and follow up images were acquired every 6 weeks thereafter until tumor progression or death. Imaging included T1-enhanced imaging and APTw imaging. The volumes of interest were selected as enhancing voxels on T1-weighted images and corresponding areas on APT images. The signal intensity was measured before and after treatment on APTw images. Percent change in signal intensity from baseline to first follow-up was compared.

**RESULTS:** The high signal intensities of baseline on APTw images were significant decreased (Figure 1), while the relative low signal intensities were observed no significant changes after target therapy. The cutoff of APTw signal intensity was greater than 2.2%. On the other hand, there was no therapeutic effect for the cystic parts on T1-enhanced images (Figure 2).

**DISCUSSION:** The high signal intensity on APTw images, corresponding areas on the enhanced parts on T1-weighted images, may represent the cellularity, and angiogenesis of glioma. So, this kind of recurrent GBM may have response to antiangiogenic therapy. The relative low signal intensity on APTw images, or the cystic parts on T1-enhanced images may not response bevacizumab therapy because of no or not enough angiogenesis for this kind of recurrent GBM.

**CONCLUSION:** APTw value, as a biomarker, may predict which kind of recurrent GBM has a good response prior to treatment with bevacizumb.

**REFERENCES:**

1. Rahul N.Sawlani, *et al*. Radiology 2010;255:622-629. 2. Zhibo Wen, *et al*. NeuroImage 2010;51:616-622

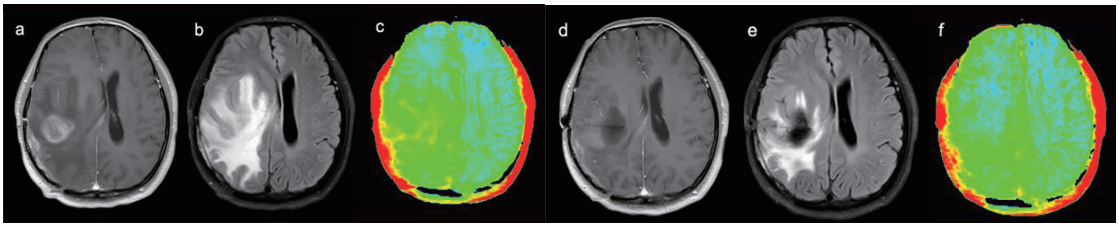



Figure1. A 43-year-male patient with recurrent GBM. (a,b,c) The signal intensity on APTw image was high (2.4%) with obvious enhancement on T1-weighted image and serious edema on Flair image before bevacizumab therapy. (d,e,f) 12 weeks later with treatment of bevacizumab, the signal intensity was decreased on APTw image (1.5%) with slight enhancement on T1-weighted image and less edema on flair image.

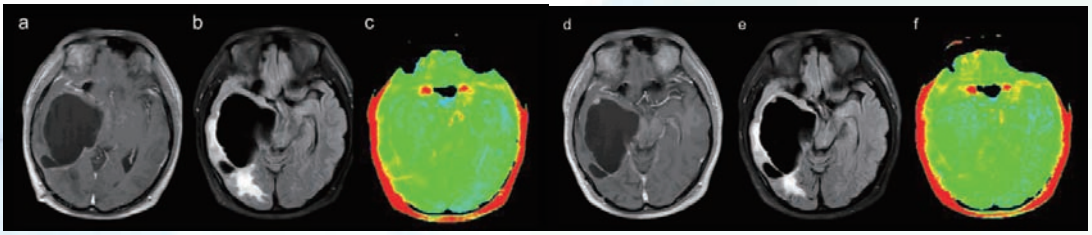



Figure 2. The cystic portion on T1-enhanced image without therapeutic effective with bevacizumab therapy.

**Added Value of Amide Proton Transfer Imaging in Brain Tumors**

Sung Soo Ahn[1]
[1]*Yonsei University College of Medicine, Seoul, Korea*

**INTRODUCTION:** Amide proton transfer imaging (APT), a type of the CEST-based molecular MRI technique, is based on the chemical exchange between free bulk water protons and the amide protons (-NH) of mobile proteins and peptides. It has been shown that APT imaging has values for brain tumor evaluation to enhance the noninvasive identification of brain tumors from peritumoral edema or normal tissue, to differentiate high-grade from low-grade tumors, to separate high- from low-grade tumors that do not show Gd enhancement, or to differentiate treatment-related damage from tumor recurrence. The presentation will provide the added value of APT to the other imaging or clinical features for tumor grading and prediction of survival.

**ADDED VALUE TO CONVENTIONAL IMAGING:** Intracranial meningioma is one of the most common primary brain tumors. Unlike typical meningiomas (WHO grade I) showing good prognosis, atypical meningiomas (WHO grade II) and malignant meningiomas (WHO grade III) can show aggressive biological behaviors and are likely to recur. Therefore. preoperative prediction is important because it influences treatment planning. We investigated the difference in APT-weighted signals between benign and atypical meningiomas and determined the value of APT imaging for differentiating the two. We found that atypical meningiomas exhibited significantly higher APT-weighted signal intensities than benign meningiomas. The discriminative value of conventional MRI improved significantly when combined with APT imaging for diagnosis of atypical meningioma.

**ADDED VALUE TO ADVANCED IMAGING:** The gold standard for glioma grading is surgical sampling, and this invasive procedure carries the risk of sampling from a suboptimal site, due to the intratumoral heterogeneity of gliomas. We evaluated the added value of APT imaging to the apparent diffusion coefficient (ADC) from diffusion tensor imaging (DTI) and the relative cerebral blood volume (rCBV) from perfusion magnetic resonance imaging (MRI) for discriminating between high- and low-grade gliomas. We found that APT imaging may be a useful imaging biomarker that adds value to the ADC for discriminating between low- and high-grade gliomas.

**ADDED VALUE TO CLINICAL FACTORS:** High grade gliomas (HGG, WHO grade III and IV gliomas) are malignant tumors and carry poor prognosis despite aggressive treatment. Age, extent of resection of the tumor, tumor site, and Karnofsky performance status (KPS) score were reported as prognostic factors for HGG. We evaluated the added value of APT imaging to clinical factors and molecular markers for predicting prognosis in high grade gliomas. Our results demonstrated that high APT signal was a significant predictor of a poor prognosis. APT imaging showed the incremental prognostic value over standard clinical prognostic factors. The incremental prognostic value of APT imaging was borderline significant when APT imaging was integrated with both clinical and molecular markers. We believe that preoperative APT imaging is a useful imaging biomarker for predicting prognosis of patients with HGG.

**CONCLUSION:** APT imaging has added values in brain tumors to conventional imaging for meningioma grading, to advanced imaging for glioma grading and prediction of treatment response, and to clinical factors for prediction of prognosis in gliomas.

**ACKNOWLEDGMENTS:** Only include if necessary.

**REFERENCES:**

1. van Zijl, P. C, *et al.* Magn Reson Med 2011;65:927-948
2. Zhou, J., *et al.* Magn Reson Med 2008;60:842-849
3. Joo B, *et al.* Eur Radiol 2018;28:331-339
4. Choi YS, *et al.* Eur Radiol 2017;27:3181-3189
5. Park JE, *et al.* Radiology 2015;277:151-161

## NOE(-1.6ppm) imaging in brain tumor

Zhongliang Zu[1]
[1]*Vanderbilt University Institute of Imaging Science, Nashville, TN, US*

**INTRODUCTION:** Recently, a new relayed nuclear Overhauser enhancement (rNOE)-CEST signal at around -1.6 ppm, termed NOE(-1.6) was reported [1]. This abstract aims to evaluate its application in brain tumors on animal models and provide a pilot study on its contrast mechanism.

**METHODS:** All measurements were made on a Varian 9.4 T magnet with a 38 mm Litz RF coil. CEST Z-spectra were acquired with RF offsets from -10 to 10 ppm and irradiation powers of 0.25μT and 1μT on 6 rat brains bearing 9L tumors. $T_1$ map was also measured using an inversion recovery sequence. Images were acquired with matrix size 64 × 64, FOV 30 × 30, and one average. we performed a multiple-pool Lorentzian fitting approach to process the Z-spectra. Reference signals for quantifying the NOE(-1.6) and another NOE signal at -3.5 ppm, termed NOE(-3.5), were obtained from the sum of all Lorentzians except the corresponding pool. Apparent exchange-dependent relaxation (AREX), which inversely subtracts the reference and label signals with $T_1$ normalization, was applied to quantify the two NOE effects. A ratiometric approach, which uses the ratio of two AREX values acquired at two different RF powers, was also applied to obtain a $AREX_{ratio}$ metric that is more specific to the NOE coupling rate than the NOE signal amplitude.

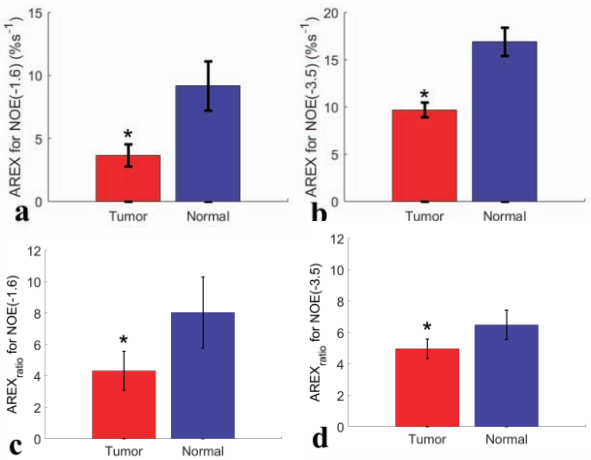



Fig. 1: Statistics of AREX for NOE(-1.6) (a) and NOE(-3.5) (b), $AREX_{ratio}$ for NOE(-1.6) (c) and NOE(-3.5) (d) from tumors and contralateral normal tissues.

**RESULTS:** Fig. 1 shows the statistics of AREX and $AREX_{ratio}$ for the NOE(-1.6) and NOE(-3.5) from tumors and normal tissues. The relative changes of AREX in tumors are -62.2% for NOE(-1.6) and -44% for NOE(-3.5), while the relative changes of $AREX_{ratio}$ in tumors are -50.9% for NOE(-1.6) and -26% for NOE(-3.5). Note that the relative change of $AREX_{ratio}$ is close to that of AREX for NOE(-1.6), suggesting that the change of coupling rate may be a major contributor to the hypointense NOE(-1.6) signal in tumors. Fig. 2 shows the maps of AREX and $AREX_{ratio}$ for the NOE(-1.6) and NOE(-3.5), respectively, from a rat brain.

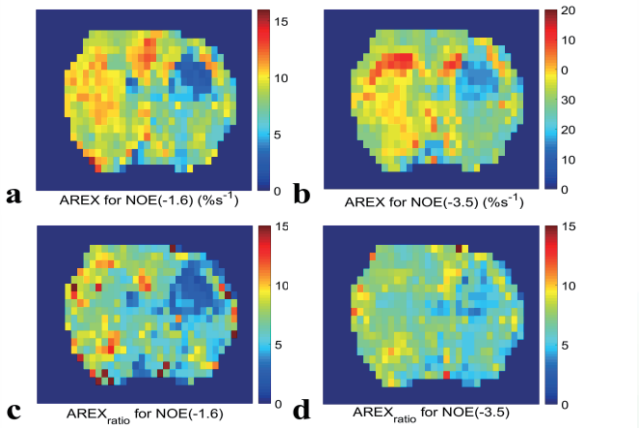



Fig. 2: Maps of AREX for NOE(-1.6) (a) and NOE(-3.5) (b), $AREX_{ratio}$ for NOE(-1.6) (c) and NOE(-3.5) (d) from a representative rat brain bearing 9L tumor.

**DISCUSSION:** All CEST and NOE signals depend on both of the solute concentration and the exchanging/coupling rate. Here, we applied a ratiometric approach to simply isolate a coupling rate-weighted signal. Previously, it was reported that the NOE(-1.6) may arise from the NOE effect between water protons and membrane choline phospholipid head groups [2]. Thus, the hypointense NOE(-1.6) signal in tumors may be due to the change of the mobility of phospholipids which regulate its coupling rate.

**CONCLUSION:** The NOE(-1.6) and the ratiometric NOE(-1.6) may be used to diagnose tumors. A further evaluation of the mechanism for the variation of the NOE(-1.6) coupling rate in tumors is warranted, because it may represent a new biomarker of pathologies and physiologies.

**REFERENCES:** 1. Zhang XY, et al. Magn Reson Imaging 2016;34(8):1100-1106. 2. Zhang XY, et al. Magn Reson Med 2017;78(2):588-597.

**Amide Proton Transfer-Weighted MRI for predicting histological grade of hepatocellular carcinoma: Comparison with Diffusion-Weighted Imaging**

Yue Lin[1], Chunmei Li[1], Jinyuan Zhou[2], Min Chen[1]

[1]Department of Radiology, Beijing Hospital, National Center of Gerontology, Beijing, and China

[2]Department of Radiology, Johns Hopkins University, Baltimore, USA

**INTRODUCTION:** Worse histological grade of hepatocellular carcinoma (HCC) correlates with poor patient. No studies have been reported that were designed to evaluate the potential of Amide Proton Transfer-Weighted (APTw) MRI in predicting histological grade of HCC.

**PURPOSE**: To prospectively evaluate the feasibility and capability of APTw MRI in predicting the histological grade of HCC, compared with diffusion-weighted imaging (DWI).

**METHODS**: Between May 2017 and April 2018, 32 consecutive patients with surgically confirmed HCC were enrolled, who underwent DWI with 2 values (0, 1000s/mm$^2$) and APTw sequence on a 3.0-T MRI scanner. The APTw images were post-processed in an external software. ADC images were automatically generated after DWI images acquisition. Two radiologists drew ROIs independently. APTw values and ADC values were acquired, respectively. Inter- radiologist agreement was assessed by using the intraclass correlation coefficient (ICC). Student *t* test, $x^2$ test, Receiver operating characteristic (ROC) analysis and the Spearman correlation test were used for statistics

**RESULTS**: The ICC values between the two radiologists were 0.856 for APTw and 0.964 for ADC. Significant differences in the APTw and ADC values among the groups were found (*P* = .046; *P* = .027, respectively). The ROC analyses demonstrated that the APTw and ADC values had good diagnostic performance in differentiating the low-grade HCC from the high-grade HCC, with areas under the curve (AUCs) of 0.826 and 0.753. Significant correlations were found between APTw and histological grades (r = 0.555; P = .001), as well as ADC values and histological grades (r = -0.431; P =.014).

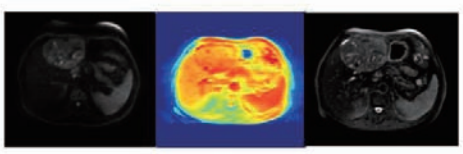
**DISCUSSION:** APTw could provide indirect acquisition of signal intensity through the chemical exchange between amide protons in mobile proteins and peptides and bulk water protons. In high-grade HCC, the mobile proteins and peptides are more abundant than in low-grade HCC.

**CONCLUSION**: The APTw values show better diagnostic performance in differentiating high-grade HCC from low-grade HCC, compared with ADC values.

**REFERENCES:**

1. Wei-Chou Chang, et al. Abdom Imaging 2014; 39(6):1202-1212.

2**.** Shao-Cheng Zhu, et al. *World J Gastroenterol* 2018 ;24(8): 929-940.




A 65-year-old man with a 12-cm surgically verified hepatocellular carcinoma of with low-grade HCC.

## Z-spectral modeling for CEST-MRI of bladder cancer

Xunan Huang[1], Jiaxue Hao[1], Bo Liu[1],Yue Zhao[1], Xianghuai Zhang[1], Guang Jia[1]*
*[1]School of Computer Science and Technology, Xidian University, Xi'an, Shannxi, 710071, China*

### Introduction

Bladder cancer is one of the most common tumors and has a relatively large impact on men's health (1). Incorrect clinical staging and especially understaging is a serious problem in bladder cancer (2). Nneoadjuvant chemotherapy prior to radical cystectomy can improve oncologic outcomes and overall survival (3). Amide-proton-transfer (APT) MRI, has been designed to non-invasively measure a variety of amide protons of endogenous mobile proteins and peptides in clinical imaging (4). This study is to evaluate whether APT-MRI can improve the accuracy of bladder cancer detection, tumor staging, and assessment of bladder tumor response to neoadjuvant chemotherapy.

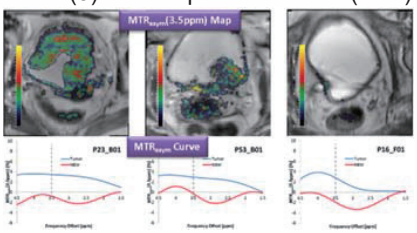



Figure 1. APT-MRI can depict bladder cancer region by mapping the elevated mobile protein level in cancerous tissues.

### Materials and methods

A total of 56 bladder cancer patients were enrolled in this study. 22 patients underwent cystectomy without receiving any neoadjuvant chemotherapy. 34 patients received cisplatin-based therapy. All patient scans were performed on a 3T MRI system (Achieva, Philips Healthcare). APT-MRI was based on 2D single-shot single-slice TSE sequence with the pre-saturation pulse composed of a train of sixteen block pulses ($B_1$ = 4.0 uT, duration = 0.5 sec). Z-spectra with the pre-saturation pulse at 33 frequency offsets (-8 to 8 ppm, interval 0.5 ppm) were acquired in a transverse slice covering suspected bladder tumors. $B_0$ field map was acquired using a dual-echo FFE sequence. $MTR_{asym}$(3.5ppm) based on the asymmetric signal at 3.5 ppm was defined to quantify cellular mobile protein and peptide levels. $\Delta MTR_{asym}$(3.5ppm), defined as $MTR_{asym}$(3.5ppm) in baseline scan (B01) subtracted from $MTR_{asym}$(3.5ppm) in mid-cycle follow-up (F01), was used to differentiate the neoadjuvant chemotherapy responders from non-responders.

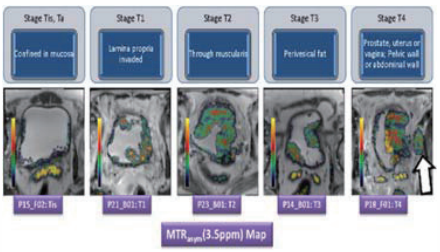



Figure 2. Typical $MTR_{asym}$(3.5ppm) maps from different stage bladder cancers. The metastasized lymph node in P18_F01 showed elevated $MTR_{asym}$(3.5ppm).

### Results

*Tumor detection* A total of 14 APT-MRI scans with little or no motion artifact were analyzed (Figure 1). $MTR_{asym}$(3.5ppm) was 3.2% ± 1.6% in tumor regions (N = 14), -0.13% ± 1.6% in normal bladder wall (NBW, N = 14). Tumor showed significantly higher (3.4% ± 1.6%) in $MTR_{asym}$(3.5ppm) than NBW ($p < 0.001$). Tumor showed significantly lower (-7.3% ± 2.0%) in $MTR_{asym}$(3.5ppm) than SV or Uterus ($p < 0.001$) after adjusting for multiplicity using Bonferroni method.

*Tumor staging* 16 assessable APT-MRI scans with pathological staging results were analyzed (Figure 2). $MTR_{asym}$(3.5ppm) was 1.8% ± 1.5% in tumors <= T2 (N = 9), and 4.6% ± 2.1% in tumors >= T3 (N = 7). Higher stage tumors (>= T3) showed significantly higher $MTR_{asym}$(3.5ppm) than lower stage tumors (<= T2) ($p < 0.01$).

*Therapy response* 12 out of 17 patients were defined as responders. All tumors in baseline imaging were shown to have MRI-detectable cellular protein levels (Figure 3). There was no significant difference in baseline $MTR_{asym}$(3.5ppm) between the responders (4.1 ± 1.5%) and the non-responders (3.3 ± 2.0%, $p = 0.41$). Tumor mobile protein levels in the chemotherapy responders exhibited a decrease from baseline to mid-cycle follow-up scan ($\Delta MTR_{asym}$(3.5ppm) = -2.9 ± 2.2%). The tumors in the non-responders were shown to be stable in mobile protein levels ($\Delta MTR_{asym}$(3.5ppm) = 1.5 ± 1.3%). There was a significant difference in tumor $\Delta MTR_{asym}$(3.5ppm) between the responders and the non-responders ($p < 0.001$).

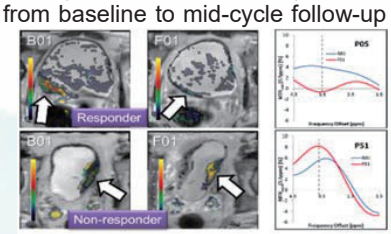



Figure 3. Typical baseline and mid-cycle APT-MRI scans from a chemotherapy responder and a non-responder.

### Discussions

This trial is the first application to clinical bladder cancer patients. APT-MRI revealed increased MRI-detectable mobile proteins in cancerous bladder lesions. Successful neoadjuvant chemotherapy induced decreased protein level detected by APT-MRI. Non-responders showed stable disease with constant or increasing MRI-detectable mobile protein levels.

### Conclusion

The APT-MRI signal-based detection and quantification of endogenous cellular protein concentrations has shown to be a promising marker in improving chemotherapy response assessment. Dedicated Phase II trials to appropriately assess the efficacy of this novel molecular approach should be undertaken.

### References

1. Marko Babjuk. European urology 2018;73(1):51-52. 2. Rajesh A, et al. Clin Radiol 2011;66(12):1140-5. 3. Grossman HB, et al. N Engl J Med 2003;349:859-66. 4. Jia G, et al. J Magn Reson Imaging 2011;33:647-654.

**Lipo-/Cell-CEST: enhanced sensitivity for new applications**

Tripepi M. Ferrauto G., Bennardi P, Delli Castelli D. and Aime S.

*Department of Molecular Biotechnology and Health Science, University of Turin Italy*

**INTRODUCTION:** Some years ago, the issue of overcoming the low sensitivity of CEST contrast agents has been tackles by developing nano-sized vesicles entrapping paramagnetic shift reagents. These systems have been called LipoCEST; their sensitivity was shown to fall in the high pM range[1]. Despite this huge gain in sensitivity, the use of LipoCEST *in vivo* was hampered because these vesicles are easily internalized (and de-assembled) in macrophages or at other target cells. A further development led us to use cells as containers for the paramagnetic shift reagents (SRs). The entrapment of SRs into the cells'cytoplasm (Cell-CEST)[2]. allows the exploitation of the huge amount of mobile water protons belonging to the inner cellular compartment. CellCEST represents a dramatic improvement for the *in vivo* CEST experiments, nevertheless cellular systems lack the versatility of liposomal vesicles (easily loaded with the proper cargo or functionalized with the proper targeting vector). The aim of this study was to merge the characteristics of Cells and Liposomes in order to overcome the *in vivo* drawbacks shown by Lipo-CEST agents in targeting experiments. The idea was to use giant liposomes (GUVs) that were early proposed as cell mimicking systems and never used as therapeutics or diagnostics carriers.

**METHODS:** GUVs have been prepared according to the gentle swelling method reported elsewhere[3].
Briefly: i) the mixture of phospholipids is placed on the bottom of a flask and dried using a nitrogen flow, ii) the hydration solution is gently poured into the flask, iii) the flask is sealed and the lipids are allowed to swell without any mechanic stress at 60°C for 2 hours, iv) once recovered, liposomes are centrifuged at 6500 rpm for 15 minutes in order to retain pelleted giant liposomes and discharge small liposomes or impurities with the supernatant. The hydration solution consisted of a paramagnetic shift reagent (e.g. TmHPDO3A) and a fluorescent dye (carboxyfluorescein). The phospholipidic blend for the membrane was made by DPPC/DSPE-PEG(2000)-Folate/DPPE-Liss Rhod (96.95/3/0.05 molar ratio). MRI-CEST characterization has been performed either at 300 or 600 MHz. Targeting experiments have been performed at 37°C on IGROV-1 cells and the binding has been visualized either by confocal imaging and CEST measurements.

**RESULTS:** GUVs vesicles entrapping shift reagents (GiantCEST) have been successfully prepared and characterized. They showed an analogous magnetic behavior as the one reported for spherical Lipo-CEST vesicles but with a sensitivity enhancement of three order of magnitude (*f*M range). When functionalized with targeting moieties on the external surface, GiantCEST agents bind the target cells without proceeding in an internalization process as nicely shown in the case of the binding to folate receptors. Shrunken vesicles were also prepared and confocal images showed that Giant liposomes react to the osmotic stress in a different way with respect to the smaller ones[1,2]. Peculiar membrane invaginations were observed.

**DISCUSSION:** The obtained results showed that the use of vesicles endowed with a mean diameter ten times greater than those displayed by LipoCEST lead to an increase in CEST-sensitivity of three orders of magnitude. This behaviour is due to an increase of inner water volume of one thousand times. Importantly, functionalized Giant-CEST agents are not internalized into cells even though they can bind to target epitopes on cells' membranes.

**CONCLUSION:** New CEST systems has been developed by using Giant Liposomes as carriers of SRs. These systems showed to be the most sensitive CEST agents ever reported and allow to overcome one of the main drawback encountered from their smaller analogs (LipoCEST) as they do not internalize into cells. Giant-CEST do not de-assemble upon binding to cells'membranes and hence appear good candidates for targeting experiments.

**REFERENCES:**
1. Aime S. *et al* NMR Biomed. 2013, 26, 839-49
2. Aime S. *et al* Wiley Interdiscip Rev Nanomed Nanobiotechnol. 2016, 8, 602-18.
3. Reeves J.P. *et al* J. Cell. Physiol 1968; 73: 49-60

**Highly sensitive CEST MR molecular imaging using natural dextrans**

Guanshu Liu, Ph.D.[1,2]
*[1]F.M. Kirby Research Center, Kennedy Krieger Institute*
*[2]Department of Radiology, Johns Hopkins University School of Medicine)*

**INTRODUCTION:** Albeit CEST agents holds the promise to become the next generation MR molecular imaging agents with great biocompatibility and translatability, their applications are often challenging due to its inherently low detectability. One practical way to improve the sensitivity of CEST MRI is to use polymerized or nanoparticulate agents. Dextran is a widely used clinical agent composed of glucose and abundant in hydroxyl exchangeable protons, making it highly sensitive CEST agents. In the present, we aimed to develop dextran (**Fig. 1a**) as a platform agent for a variety of biomedical applications.

**METHODS:** The *in vitro* CEST contrast of dextran was assessed using a vertical bore Bruker 11.7 T MRI scanner as described previously.[1] *In vivo* MR studies were carried out on a Biospec11.7 T horizontal MRI scanner as described previously.[2] For the dynamic study, CEST images were repetitively acquired at the offsets of ± 0.6, ± 0.8, ± 1.0, and ± 1.2 ppm using a modified fat-suppressed RARE sequence (CW saturation pulse, B1=1.8 μT and 3 seconds, TR/TE=5000/5 ms, RARE factor=10). To correct the $B_0$ inhomogeneity, WASSR scans were acquired before and after the CEST acquisitions.

**RESULTS:**

1. CEST characteristics of dextrans. As shown in **Fig. 1**, we characterized the CEST properties of dextrans. At physiological pH (~7.3) and a $B_1$ of 3.6 μT, a detectability of 5% $MTR_{asym}$ of dexCEST MRI is achieved for 3-mM glucose unit concentration, corresponding to concentrations of 54.0-, 7.7-, 3.6-, and 0.3-mM dextran for sizes of 10, 70, 150, and 2000 kD, respectively[3].

2. Dextran for permeability assessment. As shown in **Fig. 2**, we showed that CEST MRI could be used to assess the differential permeability of the tumor to 9.5 kD dextran (4 nm), and 70 kD dextran (14 nm)[3].

3. Dextran-based diamagnetic agent for PSMA receptor imaging. As shown in **Fig. 3,** we have synthesized a targeted MRI agent for PSMA-targeted imaging, and demonstrated its sensitive detection with CEST MRI in a relevant xenograft model.[4]

**CONCLUSION:** Our results clearly showed that 1) dexCEST MRI provides a natural imaging label approach with great translation potential; 2) Because dextrans are available in a wide size range, it can be used to characterization of the size-dependent tumor vascular permeability; 3) Using dynamic CEST MRI acquisition scheme allows the specific detection of dexCEST in the presence of tissue background; 4) dexCEST MRI is a robust MR molecular imaging approach with greatly improved sensitivity, which allows the detection of disease biomarkers at μM concentration range.

**ACKNOWLEDGMENTS:** Supported by NIH grants R03EB021573, R01CA211087, R21CA215860, and R01EB015032.

**REFERENCES:**

(1) Liu, G., *et al. Contrast Media Mol. Imaging* **2010**, *5*, 162-70.(2) Xu, X., *et al. Magn. Reson. Med.* **2015**, *74*, 1556-63.(3) Li, Y., *et al. Magn. Reson. Med.* **2018**, *79*, 1001-1009. (4) Liu, G., *et al. Nat Biomed Eng* **2017**, *1*, 977-982.

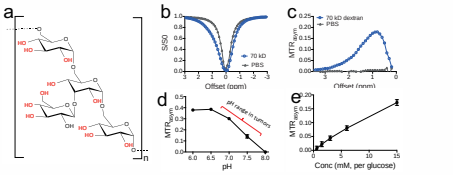



***Fig.1.*** **Dextran and dexCEST a**) Chemical structure of dextrans, **b**) Z-spectra and **c**) $MTR_{asym}$ plots of 70 kD dextran (20 mM, 37 ºC and pH =7.4); d) The pH dependence and **d**) Sensitivity of dexCEST contrast.

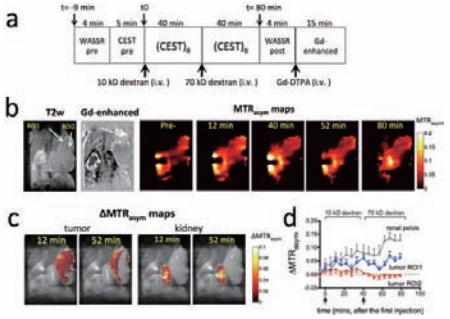



***Fig. 2. In vivo*** **CEST MRI of dextran uptake in tumor and kidney**. **a**) Imaging protocol. **b**) T2-w, Gd-DTPA enhanced T1-w, and CEST contrast maps at different time points. **c**) The $\Delta MTR_{asym}$ maps of only tumor and kidney at 17 minutes and 57 minutes after the experiment started (12 minutes after the injection of 10 kD or 70 kD dextran). **d**) Change of mean ROI CEST contrast in the two tumor ROIs and the renal pelvis. The changes were quantified by $\Delta MTR_{asym}(t)= MTR_{asym}(t)- MTR_{asym}(t0)$.

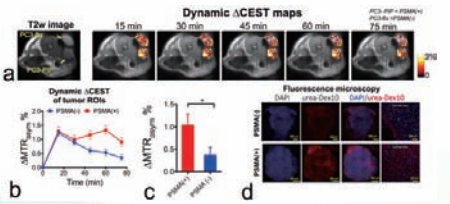



***Fig. 3. In vivo*** **CEST MRI detection of the uptake of urea-Dex10 in PSMA (+) and PSMA (-) tumors. a**) The T2 weighted image and dynamic CEST maps at 1 ppm after the injection of 375 mg/kg urea-10KD-dextran (injection volume =100 μL). **b**) Mean changes in the CEST signal in the PSMA (+) and PSMA (-) tumors. **c**) Comparison of the mean CEST change in the two tumor types. *: P<0.05 **d**) Fluorescence microscopy of nuclei (blue, stained with DAPI) and dextran (red, NIR-600-labeled).

**Evaluations of tumor models with acidoCEST MRI**

Rachel A. High,[1] Leila R. Lindeman,[1] and Mark D. Pagel[3]

1. Cancer Biology Interdisciplinary Program, University of Arizona, Tucson, AZ
2. Department of Cancer Systems Imaging, UT MD Anderson Cancer Center, Houston, TX USA

INTRODUCTION: Solid tumors often exhibit the Warburg effect, whereby upregulated glycolytic metabolism produces excess lactic acid in the extracellular tumor microenvironment, causing tumor acidosis. We have developed a non-invasive imaging method, known as acidoCEST MRI, to evaluate tumor acidosis. We have applied acidoCEST MRI to assess tumor acidosis during the evolution of pancreatitis and pancreatic cancer in mouse models, and to improve the diagnosis of lung cancer vs. lung infection in mouse models.

METHODS: Spontaneous development of pancreatic ductal adenocarcinoma was initiated by administering 14 caerulein injections over a 62 hour period to a KrasLSL.G12D/+; PdxCre mouse model. Mice were imaged 1 hour to 8 weeks after injections. Spontaneous orthotopic lung adenocarcinoma was induced in male A/J mice with a single intraperitoneal injection of 1mg/g of urethane. Lung tumors reached a size of 1 mm at 25-26 weeks of age. A *coccidioides* model was induced by infecting female mice with *Δcps1* spores. Mice were imaged 14-28 days after exposure. All mice were imaged using a CEST-FISP method[1] with respiration-gating and with 3.5 μT saturation applied for 6 sec. Four images were acquired, then 250 μL of 370 mgI/mL iopamidol was injected IV, followed by an IV infusion of 400 μL/hr of iopamidol, and finally six additional images were acquired. AcidoCEST MRI data was processed as previously described.[2]

RESULTS: Pancreatic cancer lesions were found to be more acidic than both healthy and inflammatory pancreatic tissue. Average pHe in healthy pancreatic tissue was 7.02 at 5 weeks as opposed to 6.98 in pancreatitis and 6.79 in cancer lesions. Using murine models of lung adenocarcinoma and coccidoidomycosis, average lesion pHe differed significantly between tumors and granulomas, with $p = 0.0001$ between lung cancer and lung infection cohorts, and with the least acidic tumor showing a lower pHe than the most acidic infectious nodule.

DISCUSSION: These results show that acidoCEST MRI can be applied to evaluate tumor acidosis, which can improve the diagnoses of pancreatic cancer and lung cancer.

ACKNOWLEDGEMENTS: The authors would like to thank Experimental Mouse Shared Resource and Tissue Acquisition and Molecular Analysis Shared Resource at the University of Arizona Cancer Center, as well as The Valley Fever Center for Excellence at the University of Arizona.

REFERENCES:
1. Jones KM, *et al.* Proc SPIE 2016;9788:978815.
2. Shah T, *et al.* Magn Reson Med 2011;65:43-437.

**CEST imaging of hydrogel-based therapy**

X. Han[1], J. Huang[1], J. H. C. Lai[1], K. W. Y. Chan[1,2*]

[1]*Department of Biomedical Engineering, City University of Hong Kong, Hong Kong;*

[2]*Russell H. Morgan Department of Radiology and Radiological Science, Johns Hopkins Medicine, Maryland, USA*

**INTRODUCTION:** Hydrogel has numerous biomedical applications as carriers for drugs or cells. Imaging the interplay of molecules in this matrix has a pivotal role in monitoring pathology and therapeutic outcomes. We have demonstrated that Chemical Exchange Saturation Transfer (CEST) MRI reveals viability of encapsulated cells *in vivo* using pH-nanosensor approach(1), others have showed the imaging of hydrogel compositions and its degradation(2-4). To facilitate applications in the brain, we developed injectable hydrogels with CEST nanosensors to detect changes in the local environment after transplantation. We developed a series of injectable hydrogel formulations based on commonly used natural polymers, and found that the rheological properties were adjustable to fit applications in the brain. These properties include shear stress, viscosity and storage modulus. Its porous structure could facilitate the transport of nutrients and cell migration. Moreover, in addition to the CEST contrast of compounds within liposomes (at 5 ppm), we observed the nuclear overhauser enhancement (NOE) from the phospholipid bilayers at 3T. This could act as an independent contrast to indicate the number of nanosensors presence.

**METHODS:** Liposomes were prepared by using thin film hydration method(1,5,6). In brief, the lipid mixture was dried on a rotary evaporator to form a homogeneous thin film layer. Then, 1 mL barbituric acid solution (25 mg/mL, pH 7.2) was added to hydrate the thin film under 65 $^{o}$C for 1 h. It was then mixed with either alginate or hyaluronic acid methylcellulose(HAMC)(7) injectable hydrogels with minimal dilution of liposome solution. Phantoms were imaged on a horizontal bore 3T preclinical Bruker Avance system (Bruker Biosciences, Billerica, MA) at 37 $^{o}$C. A volume RF coil with an internal diameter of 38 mm was used. The $B_0$ field was shimmed and a modified rapid acquisition with relaxation enhancement(RARE) sequence including a saturation pulse was used to acquire saturation images at different irradiation frequency, which were used to generate the z-spectrum. Images were acquired with the following parameters: Slice thickness=1 mm, field of view(FOV)=20×20 mm, image size=64×64, RARE factor = 32, repetition time/echo time(TR/TE)=6000/4.7 ms. (-7 to + 7 ppm, 0.2 ppm steps or 25.6 Hz offset step) around the water resonance (0 ppm). First, Water Saturation Shift Referencing(WASSR) mapping was employed for $B_0$ correction, for which we used a saturation pulse length of 1000ms, saturation field strength ($B_1$) of 0.2μT, and saturation frequency increment of 0.1 ppm. Secondly, CEST and relayed NOE images of BA-Lipo were acquired at varying saturation pulse($B_1$) amplitudes including 0.2,0.3,0.4 and 0.6μT with 2000 or 3000ms saturation duration to optimize the imaging parameters.

**RESULTS:** We observed that the addition of liposomes to the hydrogels, i.e. alginate and HAMC, resulted in different rheological properties and porosity. In general, liposome-incorporated hydrogels showed slightly increase in viscosity, and their storage modulus was at 10-250 Pa(at 10 Hz) with the pore size of >50 μm. Importantly, all these formulations are injectable. Moreover, we found that both the liposomes and hydrogels showed distinctive contrast at 5 ppm for BA in the aqueous core of liposomes and -3.5 ppm for the phospholipid bilayers at 3T. The contrast at 5 ppm/-3.5 ppm was (1.9%/1.5%) for alginate and (2.2%/2.0%) for hyaluronic acid hydrogels acquired at $B_1$ = 0.4 μT and $_{Tsat}$ = 3000 ms.

**DISCUSSION:** These systemic investigations of the addition of liposomes to the hydrogels allow us to reveal the relationship between the liposomal content to the resulted rheological properties and porosity of the hydrogels for neural applications. The storage modulus was slightly lower than the brain to favor cell survival(8). The resulted macroporous structure(>50 μm) could facilitate the nutrient exchange and cell migration(9). The CEST contrast at 5 ppm indicates the amount of agents within the liposomes and the one at -3.5 ppm indicates the number of liposomes, which are proportional to their relative concentration. This information is useful to monitor the relative amount of encapsulated compounds and number of liposomes in the hydrogel matrix *in vivo*.

**CONCLUSION:** We have developed injectable hydrogels with rheological properties suitable for neural applications and unique dual CEST contrast to facilitate monitoring of the hydrogel compositions, i.e. both compounds encapsulated within liposomes and number of liposomes. We expect these hydrogels could favor the cell/drug delivery to the brain, especially with its injectable hydrogel properties and sustainable drug delivery by liposomes.

**ACKNOWLEDGMENTS:** Authors thanks the funding supports for this work. *CityU: P9610362; P7200516; 6000612*; *RGC: GRF*-9042620; *NSFC*: 81871409.

**REFERENCES:** 1. Chan, K. W. et al. *Nat Mater* 2013:12:268-275. 2. Liang, Y. et al. *Biomaterials* 2015:42:144-150. 3. Jin, T. et al. *Biomaterials* 2017:113:176-190. 4. Shazeeb, M. S. et al. *Biomaterials* 2018:178:326-338. 5. Chan, K. W. et al. *WIREs Nanomed Nanobiotechnol* 2013:6:111-124. 6. Chan, K. W. et al. *J Control Release* 2014:180:51-59. 7. M.D. Baumann et al. / Journal of Controlled Release 138 (2009) 205–213. 8. M.J. Rowland et al. Biomaterials 2018:179:199-208. 9. Majumder, Poulami, et al. Angew. Chem. Int. Ed. 2018, 57, 1-6.

**Hyper-CEST for Molecular Imaging and Lung MRI**

Xin Zhou[1, 2]

*[1]National Center for Magnetic Resonance in Wuhan, Wuhan Institute of Physics and Mathematics, Chinese Academy of Sciences, Wuhan, China, [2]University of Chinese Academy of Sciences, Beijing, China*

Chemical exchange saturation transfer (CEST) imaging is a versatile molecular imaging approach for disease diagnosis and molecular imaging. Hyper-CEST method combines the hyperpolarization and saturation transfer, using highly polarized $^{129}$Xe as abundant pool, offers new possibility for molecular imaging and lung MRI.

Based on Hyper-CEST method, We had developed several kinds of $^{129}$Xe biosensor targeted to ions and biothiols with high specificity and sensitivity [1]. A cryptophane-based clamp probe was designed to detect Mercury ions, the existence of Mercury ions induce the conformational change of the biosensor and result in upfield change of chemical shift of caged $^{129}$Xe. The biosensor we synthesised to detect biothiols can selectively target mitochondria and reacts with free biothiols (As shown in figure 1), leads to the chemical shift of caged $^{129}$Xe by 1.4 ppm upfield. Besides, The detection threshold of the biosensor was found to be 200 pM, makes it promising for biothiols dectection in cells at low concentration.

We also demonstrated the feasibility of the hyperpolarized $^{129}$Xe CEST MRI for evaluating the pulmonary gas exchange function and proposed a new parameter, $T_{app}$, to quantitatively characterize the lung gas exchange function[2] . $T_{app}$ showed a significant difference between COPD and healthy rats (P<0.001) and increased in lung parenchyma of COPD rats compared with healthy rats (As shown in figure 2).

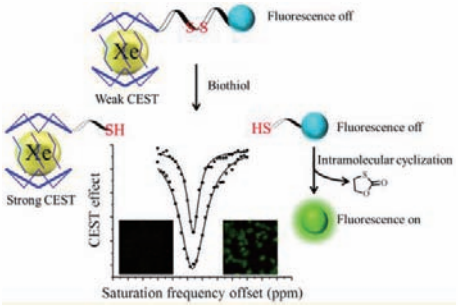



FIGURE 1 schematic representation of the biothiol triggered $^{129}$Xe biosensor

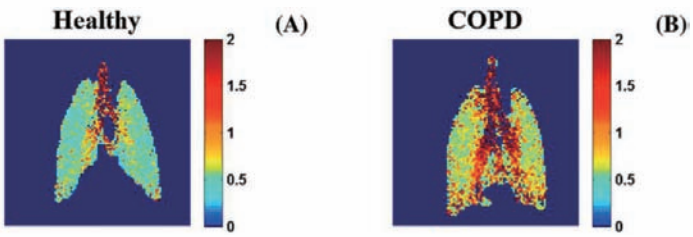



FIGURE 2 $T_{app}$ distributions in healthy rats and COPD rats by hyperpolarized $^{129}$Xe CEST MRI

**REFERENCES:**

1. Qingbin Zeng, *et al.* Analytical Chemistry 2017; 88:2288-2295.
2. Haidong Li, *et al.* NMR in Biomedicine 2017; 31:e3961.

**A Positive Contrast Chemical Exchange Experiment using Refocused Acquisition of Chemical Exchange Transferred Excitation (RACETE)**

Gutjahr FT[1], Munz E[1,2], Jakob PM[1]

[1] Universität Würzburg, Lehrstuhl für Experimentelle Physik 5, Am Hubland, 97074 Würzburg, Germany
[2] Leibniz Institute of Plant Genetics and Crop Plant Research (IPK), Corrensstrasse 3, 06466 Gatersleben, Germany

**INTRODUCTION:**

The standard CEST contrast is negative and requires the detection of small signal changes in the presence of a strong background signal. Recently a new concept for positive chemical exchange contrast imaging has been proposed which can offer some unique advantages over CEST and other chemical exchange approaches. The method dubbed RACETE (=**R**efocused **A**cquisition of **C**hemical **E**xchange **T**ransferred **E**xcitations) allows direct imaging of exchanging protons. This results in a true positive contrast based on chemical exchange with concurrent background suppression.

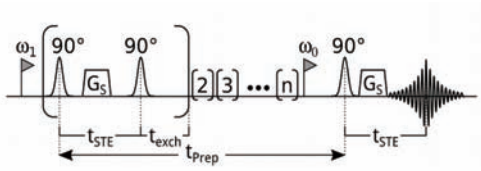



*Fig. 1: Sequence diagram of the RACETE sequence. At the position of the flags the frequency of the excitation and refocusing pulses is set.*

**METHODS & RESULTS:**

The core of the RACETE approach, which is described in full detail in [1], is the direct detection of exchanging protons. This is achieved by transferring excited solute protons to the solvent pool repeatedly followed by a refocused acquisition via selective refocusing of former solute protons now present in the solvent pool. In the original RACETE-technique the excited magnetization is stored as longitudinal magnetization producing a positive contrast image of exchanging spin magnetization, while non-exchanging spins give no background signal. This implementation (see Fig. 1) is based on the stimulated-echo pathway: In difference to the original STEAM implementation, in RACETE, the first two RF pulses are replaced by a train of typically N = 1-500 solute-selective excitation-transfer modules (ETMs), where with each ETM solute protons are excited, prepared and stored as longitudinal magnetization, subsequently transferred to water, and finally detected as stimulated echo (STE). The resulting STE constitutes the sum magnetization resulting from the N ETM-cycles and can be directly used for imaging, see Fig. 2.

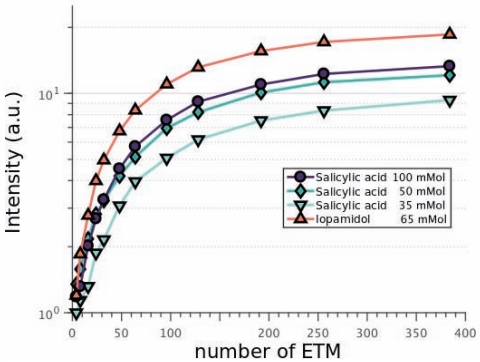



*Fig. 2: Signal dependence on the number of ETM*

As proof-of-concept a kiwifruit injected with two different solutes with labile protons (Salicylic Acid & Iopamidole) was imaged using a 7 T-MR Scanner (BioSpec, Bruker BioSpin, Ettlingen Germany). The measurement (shown in Fig. 3) demonstrates, that in a single experiment excellent water background suppression can be achieved and that only the exchanging solute protons in the injection sites are directly detected and thus exhibit a positive contrast.

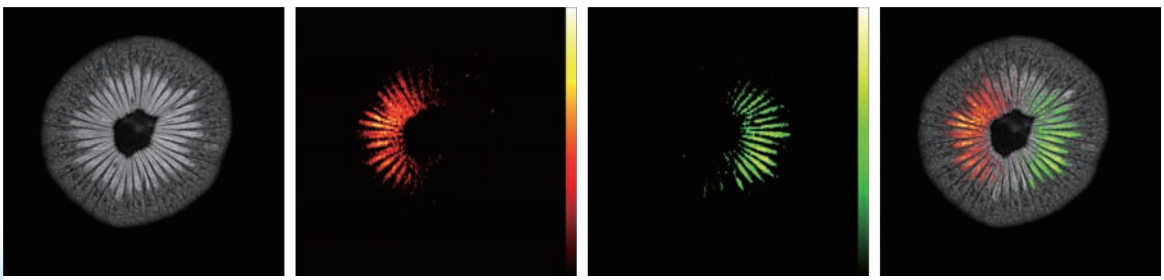


*Fig. 3: Left to right: Anatomical information, RACETE-intensity for Iopamidol (red) and salicylic acid (green), overlay*

**DISCUSSION:**

The obtained experimental results demonstrate the sensitivity of the RACETE-method to chemical exchange, the accumulation of signal strength and the intrinsic background suppression of the positive contrast approach.

**ACKNOWLEDGMENTS:**

This work was supported by grants from the Deutsche Forschungsgemeinschaft (SFB 688 Z2) and the Bundesministerium für Bildung und Forschung (BMBF01 EO1004)

**REFERENCES:**

1. Gutjahr FT, et ak. Z Med Phys. 2018 Epub (10.1016/j.zemedi.2018.05.005.)

## APT Weighted MRI as an Effective Imaging Protocol to Predict Clinical Outcome after Acute Ischemic Stroke

Guisen Lin[1], Caiyu Zhuang[1], Zhiwei Shen[1], Gang Xiao[2], Yanzi Chen[1], Yuanyu Shen[1], Xiaodan Zong[1], Renhua Wu[1, 3]

*1Department of Medical Imaging, The Second Affiliated Hospital, Medical College of Shantou University, Shantou, China*
*2Department of Mathematics and Statistics, Hanshan Normal University, Chaozhou, China*
*3Provincial Key Laboratory of Medical Molecular Imaging, Guandong, Shantou, China*

**INTRODUCTION:** Although magnetic resonance spectroscopy (MRS) has been used to detect the pH change in patients with stroke and to predict the outcome of stroke (Bolas et al., 1988),[1] it suffers from low spatiotemporal resolution which limits its clinical application (Hohn-Berlage et al., 1989).[2] So, it is reasonable that we use a new way to better evaluate stroke (Sun et al., 2012).[3] As a promising contrast mechanism, chemical exchange saturation transfer (CEST) has become an important tool in the field of molecular imaging (Ward et al., 2000).[4] Recently, APTW MRI, one form of CEST technology, has been increasingly applied in capturing tissue acidosis as a research tool based on its capability to detect pH and mobile proteins content (Zhou et al., 2003).[5]Our aim is to explore the capability of the amide proton transfer weighted (APTW) magnetic resonance imaging (MRI) in the evaluation of clinical neurological deficit at the time of hospitalization and assessment of long-term daily functional outcome for patients with acute ischemic stroke (AIS).

**METHODS:**We recruited 55 AIS patients with brain MRI imaging acquired within 24-48 hours of symptom onset and followed up with their 90-day modified Rankin Scale (mRS) score. APT weighted MRI was performed for all the study subjects to measure APTW signal quantitatively in the acute ischemic area (APTWipsi) and the contralateral side (APTWcont). Change of the APT signal between the acute ischemic region and the contralateral side (ΔAPTW) was calculated. In addition, all the patients were divided into 2 groups according to their 90-day mRS score (good prognosis group with mRS score <2 and poor prognosis group with mRS score ≥2). And ΔAPTW of these groups was compared.

**RESULTS:** We found that ΔAPTW was in good correlation with NIHSS score ($R2=0.578$, $p<0.001$) and 90-day mRSscore ($R2=0.55$, $p<0.001$). There was significant difference of ΔAPTW between patients with good prognosis and patients with poor prognosis.

**DISCUSSION:** Previous studies have shown that APT MRI is capable of detecting tissue pH (Song et al., 2017).[6]Moreover, researches performed in animal models with ischemic stroke have indicated that amide proton transfer ratio, which was calculated as MTRasym (3.5ppm), was in good correlation with pH and the concentration of lactic acid (Sun et al., 2011).[7] Since excessive acidosis is one of the key factors to cause neuron death after ischemic stroke, our study had provided insight from a different angle into the pathophysiology of ischemic stroke. In this study, since tissue acidification is closely time-related (Song et al., 2017)[6], we strictly included AIS patients within 24-48 hours of symptom onset to lower the effect of time. Notably, the progression and development of the acute ischemic stroke lesion is nearly complete at the time of imaging (within 24-48 hours after symptom onset). Obviously, the prognosis could be predicted by NIHSS score or the volume of the acute lesion. But the use of APT weighted MRI could better reveal the tissue acidification, which provides insight for better understanding the pathophysiological process of acute stroke lesion in addition to predicting the outcome.

**CONCLUSION:**APT-weighted imaging has the capability to detect pH change in the acute ischemic stroke area and quantitative analysis of APTW signal change could be used to assess stroke severity as well as to predict long term clinical outcome for AIS patients. Therefore, APT-weighted imaging could be a promising MRI method for clinical use.

**REFERENCES:**

1. Bolas NM, et al. Stroke 1988;19(5):608-14.
2. Hohn-Berlage M, et al. NMR in biomedicine1989;2(5-6):240-5.
3. Sun PZ, et al. NeuroImage 2012;60(1):1-6.
4. Ward KM, et al. Journal of magnetic resonance 2000;143(1):79-87.
5. Zhou J, et al. Nature medicine 2003;9(8):1085-90.
6. Song G,et al. Frontiers in neurology 2017;8:67.
7. Sun PZ, et al. Journal of cerebral blood flow and metabolism : official journal of the International Society of Cerebral Blood Flow and Metabolism. 2011;31(8):1743-50.

**Development of Myo-Inositol and Lactate Chemical Exchange Saturation Transfer (MILAC-CEST) MRI for Glioma Grading**

Laurie J. Rich[1], Ravi P.R. Nanga[1], Deepa Thakuri[1], Abigail Cember[1], Hari Hariharan[1], Ravinder Reddy[1]

[1]*Center for Magnetic Resonance and Optical Imaging, Department of Radiology, University of Pennsylvania, Philadelphia, PA, United States.*

**Introduction:** Gliomas are the most common form of malignant brain cancer, affecting ~6 out of 100,000 people worldwide [1]. Overall response of these tumors varies considerably by grade, with poor survival observed in higher grades despite aggressive therapeutic interventions. Accurate grading is therefore important not only to estimate patient prognosis but to select the most appropriate treatment strategy. Previous studies utilizing magnetic resonance spectroscopy (MRS) have found that myo-inositol and lactate metabolite levels differ significantly between low and high grade gliomas [2,3]. Chemical Exchange Saturation Transfer (CEST) MRI also enables the detection of these metabolites, but provides a sensitivity enhancement of two orders of magnitude compared to conventional MRS techniques [4]. Given this, the goal of this work was to explore the potential of combined myo-inositol and lactate CEST (MILAC-CEST) MRI as a tool to assess glioma grade.

**Methods:** Studies were performed *in vitro* in phantoms containing either myo-inositol (20mM), sodium lactate (20mM), or a combination of both (10 mM of each) in PBS at physiological conditions. CEST measurements were acquired on a Siemens 7 T whole-body scanner (Siemens medical systems, Malvern, PA) using a Siemens volume coil transmit/32-channel receive proton head phased-array coil. The sequence parameters were: slice thickness = 10 mm, GRE flip angle=10º, GRE readout TR = 13 sec, TE = 1.73 ms, FOV = 90 x 120 mm, matrix size = 90 x 120. CEST images were collected using a 3 second saturation pulse duration with different peak $B_1$ (50 Hz, 75 Hz, 100 Hz and 125 Hz) from 0.0 to +/- 1.5 ppm, in steps of 0.1 ppm.

**Results:** The chemical shift from hydroxyl (-OH) protons on both sodium lactate and myo-inositol has previously been shown to result in peak CEST contrast at 0.4 ppm and 0.6 ppm downfield [4,5], respectively. Due to the proximity of these two peaks, we performed studies in a phantom containing both lactate and myo-inositol, alone or in combination, and acquired CEST images from 0 to +/- 1.5 ppm at varying peak $B_1$. Consistent with previous findings, peak CEST asymmetry was observed around 0.4 ppm for lactate and 0.6 ppm for myo-inositol, while combination of the two metabolites resulted in a broad peak between 0.4-0.6 ppm. Increasing peak $B_1$ lead to an overall increase in CEST contrast for all three solutions, with greatest CEST contrast obtained at 125 Hz (**Figure 1**). Calculation of CEST contrast at 0.5 ppm revealed that combination of myo-inositol and lactate into a single solution (10 mM of each) produced CEST contrast levels that were almost double that observed from either metabolite alone (at 20 mM).

**Discussion:** Interestingly, we observed that combination of myo-inositol and lactate provides elevated CEST contrast that was greater than either metabolite alone. This enhancement increased at higher peak $B_1$, with CEST asymmetry levels of ~11% observed at 125 Hz. Studies testing the feasibility of MILAC-CEST in animals models of glioma are currently ongoing.

**Conclusions:** MILAC-CEST could be a sensitive tool for detection and grading of gliomas. Future studies will explore the potential of MILAC-CEST in both animal models of glioma and patients.

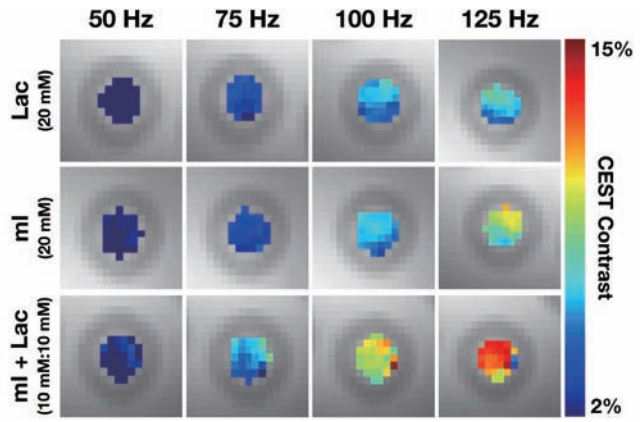



**Figure 1:** Pseudocolorized CEST contrast maps of lactate (Lac), myo-inositol (mI), and a 1:1 solution of both.

**References:**

[1] Robles PD et al. (2015) Neuro Oncol 17(6)
[2] Castillo M et al. (2000) AJNR Am J Neuroradiol 21(9)
[3] Bulik M et al. (2013) Clin Neurol Neurosurg 115(2)
[4] DeBrosse C et al. (2016) Sci Rep 6:19517
[5] Haris M et al. (2011) Neuoimage 54(3)

## Progressive Registration for Dynamic Salicylate Enhancement (DSE) Image in Chemical Exchange Saturation Transfer (CEST) MRI

Chongxue Bie[1], Yuhua Liang[1], Yanrong Chen[1], Lihong Zhang[1], Xiaolei Song[2], Xiaowei He[1]*
[1]School of Information and Technology, Northwest University, Xi'an, China, [2]The Johns Hopkins University, BALTIMORE, MD, United States

**INTRODUCTION:** Increasing interest focus on *in vivo* dynamic imaging of diaCEST agents. For example, dynamic glucose enhancement (DGE) is a feasible technique for detecting malignant brain tumors[1]. Salicylate Analogues (SAA) have shown its potential as contrast agent that can be detect by CEST-MRI, featuring chemical shift far from water (Δω = 8-10 ppm)[2]. However, by subtracting images acquired pre-injection of agents with post-injection ones, the dynamic CEST contrast images can easily corrupted by inevitable motions of animals during the long time in the scanner[3] (e.g. > 30 min). Therefore, the application of proper registration algorithms to correct for motion directly affect the accuracy of dynamic contrast signals following injection of CEST agents. Here, we introduce a novel registration approach for dynamic CEST imaging, termed as Progressive Registration, which uses the neighbor image as a reference to remove motion artifacts and mis-registration.

**METHODS:** To test the proposed method, we used a typical mouse model whose head turned left obviously during scan (Fig .1,Fig .3a). Figure 2 illustrates the flow chart of Progressive Registration. Specifically, CEST signals at Δω (Δω = +9.3ppm) after sodium salicylate (NaSA) injection and the average of pre-injection signals are first obtained (S(Δω,n), S(Δω,pre_avg) respectively). For the total of N post-injection signals, each S(Δω,n) is registered to its previous S(Δω,n-1) by using pairwise registration which is performed using the MATLAB (MathWorks, Natick, MA) built-in-function imregister, presenting a straightforward intensity-based algorithm for rigid image registration, while the first signal, S(Δω,1), is registered to S0 using the same algorithm. DSE signal is quantified as DSE(Δω,n) = [S(Δω,pre_avg) – S(Δω,n)]/S0. We examine the effectiveness of performing the proposed method by comparing with conventional registration method which registers post-injection images to the averaged S0 images[4].

**RESULTS:** DSE-MRI data contain significant regions demonstrating contrast enhancement. Comparing with conventional method, Progressive Registration greatly removed ventricle registration mismatch, and thereby significantly improved the quality of the corresponding DSE images. Although boundary artifacts appeared after NaSA injection, its change was not obvious in the following period, and its area was rather small (Fig .3b,c). What's more, Progressive method provided a smaller mean of Target Registration Error (TRE) with 0.04, while conventional method was 3.55. The performance of progressive method was further evaluated under varied time (Fig. 4). The TRE of progressive method has little change with time and had always been close to 0, much less than that of conventional.

**DISCUSSION:** The results show that it is possible to perform Progressive Registration for removing motion artifacts and registration mismatch. Notably, the conventional method chose a baseline image, S0_avg, as the target image for all post-injection images of the dynamic CEST series. It was considerable risk to register signals after normalization since S0 may with artifacts. In addition, there were large difference between target image, S0_avg , and source image, DSE image, partly caused by motion during acquisition, which would result registered images with motion artifacts and mis-registration (black circle) as shown in Fig. 3c. Progressive Registration first registered S(Δω,n), avoiding the influence of S0, and used the neighbor signal as a reference because time interval between these two signals was short and there was little difference between them, which wouldn't result irrational artifacts and mismatch in registered DSE images (Fig. 3b). We also showed good registration effect by TRE (0.04). The error was mainly caused by the rapid change of intensity over time after NaSA injection. Therefore, we need bear the registration error caused by contrast agent uptake and washout.

**CONCLUSION:** The Progressive Registration method first registers DSE signals before normalization and bases on using the neighbor signal as a reference for registration. It has the ability of removing motion artifacts and registration mismatch, and allows reliable registration with smaller TRE.

**References**

1. Xu X, et al. Magn Reson Med 2015;74:1556–1563.
2. Song X, et al. J Cereb Blood Flow Metab 2016;36:1186-1194.
3. Sundarakumar D K, et al. Ajr Am J Roentgenol 2015;204:287-296.
4. Melbourne A, et al. Lecture Notes in Computer Science 2010;6136:744-751.

**Figures**



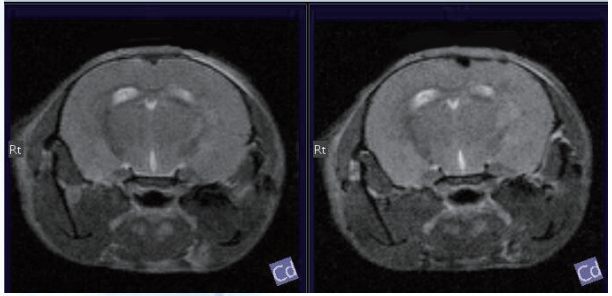



**Figure 1**: (a)Pre and (b) ~30min post NaSA injection T2 images of a typical mouse model whose head turned left obviously during the long time in the scanner.

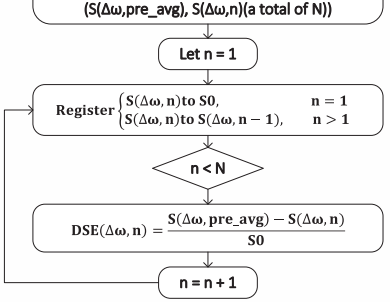



**Figure 2**: Flow chart of Progressive Registration.

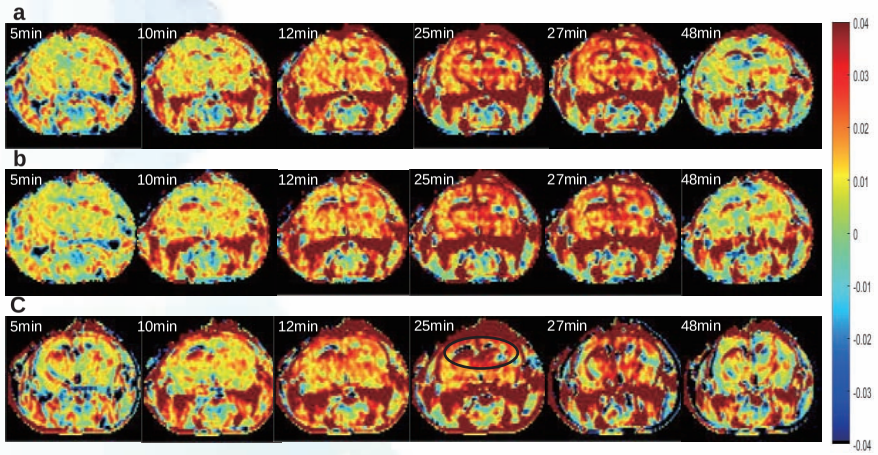



**Figure 3**: DSE images at specific time points of the typical mouse. (a)Non-registration DSE images with obviously skin boundary artifacts. (b)Progressive Registration DSE images. (c)Conventional registration DSE images.

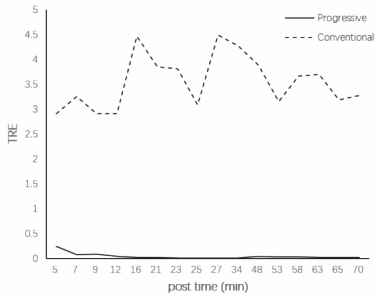



**Figure 4**:Comparison of TRE registration DSE of Progressive Registration and conventional registration method under different time-points.

**Quantitative assessment of CEST effect using a Gaussian-Lorentzian hybrid algorithm (GLHA) for Zspectra-fitting**

Lihong Zhang[1], Yanrong Chen[1], Yingcheng Zhao[1], Chongxue Bie[1], Yuhua Liang[1], Xiaolei Song[2*], Xiaowei He[1*]

*1.School of Information and Technology, Northwest University, Xi'an, China 2.The Johns Hopkins University, BALTIMORE, MD, United States*

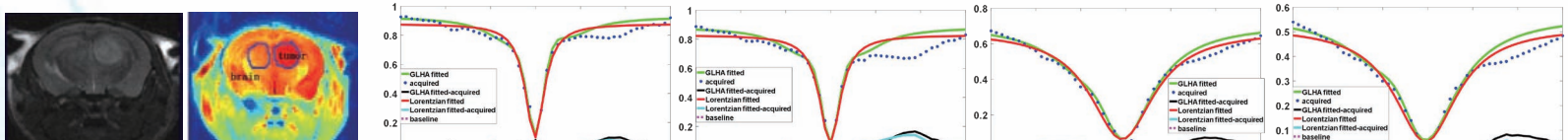
**INTRODUCTION:** The conventional CEST quantification method, termed MT ratio asymmetry (MTRasym) analysis[1], are susceptible to many contaminations including B0 inhomogeneity, semisolid macromolecular magnetization transfer (MT) and nuclear overhauser effect (NOE). To improve *in vivo* CEST quantification, Z-spectral fitting to Bloch-McConnell equation has been used to resolve the independent contributions from multiple origins. But it faces challenges of computational complexity and strong dependence on the initialization and boundaries of fitting parameters. Recently a simplified quantification method is proposed by Lorentzian fitting of Zspectra, working well in more aqueous tissue and with lower irradiation powers (e.g. $\leq 1\mu T$ at 9.4T) [2] . However, in the presence of a fast exchanging CEST species which require higher irradiation powers, the Zspectra exhibit non-Lorentzian lineshape[3]. In this study we develop a more robust CEST quantitative technique with the ability of working for both weak and strong saturation powers.

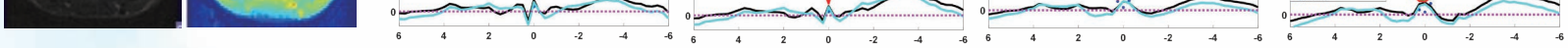
**METHODS:** For a higher saturation power or in the existence of strong MT contrast, Zspectra appears more like a Gaussian lineshape, rather than a Lorentzian shape. We proposed a Gaussian-Lorentzian hybrid fitting algorithm (GLHA) to quantify CEST effect that the best Lorentzian proportionality coefficient and the initial value of the fitting are determined in advance. Specifically, Lorentzian fraction, a, depends on the FWHM (Full width at half maximum) of the Lorentzian and the FWHM of Gaussian[4]. The CEST residual spectra are then created by subtracting the measured Z speactra from the both the GLHA and Lorentzian fitted speactra. For voxel-wise fitting, it uses globally averaged Zspectra for initial fitting of each voxel, the best Lorentzian proportionality coefficient and the best initial value of the fitting are then used as initial values for subsequent fitting of each voxel. The range of frequency offset is increased and fitted with the fitting results from previous fitting as renewed values until the maximum frequency range is reached. To validate the proposed GLHA method, we collected Zspectra of two saturation powers on NOD/SCID mice bearing glioblastoma (GBM) tumors, on a Bruker 11.7 Tesla scanner [5]. The proposed GLHA fitting is carried out and compared with conventional Lorentzian fitting and MTRasym method.

**RESULTS:** The fitting curves for both the ROIs of tumor (Fig. 1c&e) and the ROIs of contralateral normal tissue (Fig. 1d&f) at the same saturation power level, were more relevant to the actual measured points. More specifically, the residual spectra of Lorentzian fitting (cyan curve) have obvious negative values from 4 ppm to 6 ppm for both powers, and for the higher power, are also negative at offsets close to water. While GLHA fitting (black curve) does not show as much negative spectra. (Fig. 1c&d&e&f).The performance of GLHA fitting method was further evaluated by SSE and Rsquare (Fig. 2). The SSE of GLHA fitting method (0.01613) has less than that of Lorentzian fitting (0.08271)(P=0.0328, paired t-test), and the Rsquare of GLHA fitting method (0.9906) has more than that of Lorentzian fitting (0.9296)(P=0.0034, paired t-test). (Fig. 2). For both voxel-wise GLHA fitting and voxel-wise Lorentzian fitting, significant higher APT effect was found in the tumors at two saturation power levels (Fig. 3a&b) , which is consistent with result of MTRasym (Fig. 3g), and significant higher Amine (2ppm) map was also found in the tumors at two saturation power levels (Fig. 3c&d) . While, both the GLHA fitting and the Lorentzian fitting revealed higher NOE effect at 0.8 $\mu T$ (Fig. 3e) than that at 2.4uT (Fig. 3f). Meanwhile, some of the points of voxel-wise GLHA fitting as indicated by the green arrow were lighter than voxel-wise Lorentzian fitting under the same saturation power levels.

**DISCUSSION:** The accuracy of fitting results depends on the applied RF power. It has reported that the multiple-pool Lorentzian fit is accurate only at lower irradiation power ($\leq 1\ \mu T$ at 9.4T)[3], since irradiation power affects exchange rate, and thus affects the shape of Z-spectrum. The acquired curve was close to Lorentzian lineshape at the power 0,8 $\mu T$ (Fig. 1c&d) due to a lower exchanging rate, however, it was a non-Lorentzian lineshape at the power 2.4 $\mu T$ (Fig. 1e&f) of the fast exchanging rate. It can be seen that fitting is better at 2.4 $\mu T$ using GLHA fitting than at 0.8 $\mu T$ using the same fitting method (Fig.1&3). From these results, GLHA fitting is more accurate at relatively bigger power (for example, 2.4 $\mu T$ at 11.7T). However, the results are not exactly same, one possible reason is amide, amine protons and NOE *in vivo* mouse of tumor experience a more complicate environment. One limitation of the GLHA method is that due to prior to voxel-wise fitting using Gaussian-Lorentzian hybrid profile, the best Lorentzian proportionality coefficient and the best initial value of the fitting are determined in advance, so that the time consuming of fitting is increasing, our future work is to improve the efficiency of fitting.

**CONCLUSION:** GLHA fitting potentially is a robust approach for quantifying CEST effect from the Z-spectrum, which is suitable for both lower and higher saturation powers.





(a) (b) (c) (d) (e) (f)

Figure.1 (a) T2w image. (b) The region of interest (ROIs) of the tumor and normal tissue were defined on S0 image without saturation. Comparison of GLHA fitting and Lorentzian fitting between tumor and contralateral normal tissue from a representative mouse as shown in Figure 1 (b) .(c) The regions of interest (ROIs) of the tumor (0.8 $\mu$T ).(d) ROIs of the contralateral normal tissue (0.8 $\mu$T ).(e) ROIs of the tumor (2.4 $\mu$T ).(f) ROIs of the contralateral normal tissue (2.4 $\mu$T )

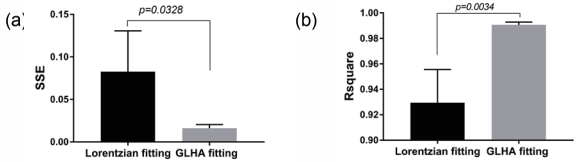
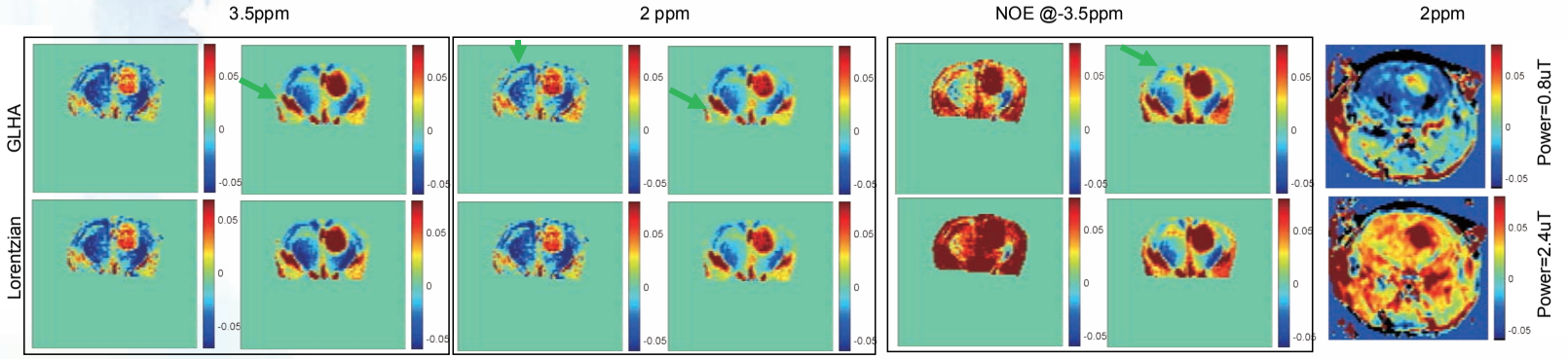



Figure2. Comparison of SSE and Rsquare of Lorentzian fittting and GLHA fitting. (a)SSE (b)Rsquare Paired Student's t-test was performed between the two methods.




(a) Power=0.8uT (b) Power=2.4uT (c) Power=0.8uT (d) Power=2.4uT (e) Power=0.8uT (f) Power=2.4uT (g)

Figure3. Fitted chemical shift maps of the each pool using Voxel-wise Lorentzian fitting and GLHA fitting in a representative rat brain with tumor which T2w image as Figure1(a) and MTRasym at two saturation power levels ($B_1$=0.8 and 2.4 $\mu$T , respectively) at 11.7T.

**References**

1. Song X,et al. Magn. Reson. Med 2012;68:1074-1086. 2. Zhou I,et al.Sci. Rep. 2017;7:84. 3. Zhang X,et al. Magn. Reson. Med 2017;30:n/a-n/a.
4. Roccoa H,et al. ACTA PHYS POL A 2012;122:666-669. 5. Song X,et al. Magn. Reson. Med 2015;73:488-496.

## Assessing Response to Therapy Using Simultaneous PET/MRI in Preclinical Model of Pancreatic Cancer

Joshua M. Goldenberg,[1] Christy M. Howison,[2] Mark D. Pagel[2,3]

1. Department of Pharmaceutical Sciences, University of Arizona, Tucson AZ USA
2. Department of Medical Imaging, University of Arizona, Tucson AZ USA
3. Department of Cancer Systems Imaging, UT MD Anderson Cancer Center, Houston, TX USA

**INTRODUCTION:** [18F]FDG PET is an outstanding method for evaluating response to therapy by monitoring glucose uptake. More recently, acidoCEST MRI has been shown to evaluate drug response by measuring tumor extracellular pH (pHe) caused by lactic acid production.[1] The combination of these two methods can potentially provide a more comprehensive analysis of a drug effect on the glycolysis pathway. We performed simultaneous PET/MRI studies on a mouse model of pancreatic cancer treated with metformin to explore the synergy between these two robust molecular imaging modalities.

**METHODS:** A flank model of MiaPaCa-2 pancreatic cancer was prepared with female SCID mice. Simultaneous PET/MRI was performed with a NuPET™ insert (Cubresa Inc.) in a 7T preclinical MRI scanner (Bruker BioSpin Inc.). 8-10 MBq (0.22-027 mCi) of $^{18}$FDG was injected intravenously and allowed to circulate for 45 minutes before initiating PET acquisition. Four CEST spectra were acquired, and 200 µL of 370 mgI/kg iopamidol was injected intravenously, followed by a 400 µL/hr infusion of agent during acquisition of six CEST spectra. This simultaneous PET/MRI protocol facilitated imaging within 1 hour. PET images were reconstructed using Ordered Subset Maximum A Posteriori One-Step Late (OSMAPOSL) iterative algorithm. Bloch fitting was used to measure concentration of agent (uptake) and acidosis (pH) with Matlab (Mathworks Inc.).[2,3] Post-processing analysis was performed with VivoQuant (inviCRO Inc.) to overlay PET and MR images.

**RESULTS:** MRI acquisition protocols had little effect on the PET count rate, and the PET instrumentation had little effect on image contrast during acidoCEST MRI, verifying that [18F]FDG PET and acidoCEST MRI can be performed simultaneously. The average $SUV_{max}$ of the tumor model had a significant decrease after 7 days of treatment with metformin, as expected. The average tumor pHe decreased after 7 days of metformin treatment, which reflected the inhibition of the consumption of cytosolic lactic acid caused by metformin. However, the average $SUV_{max}$ of the tumor model was not significantly different between the metformin-treated and control groups after 7 days of treatment, and average pHe was also not significantly different between these groups. For comparison, the combination of average $SUV_{max}$ and pHe measurements significantly differed between the treatment group and control group on Day 7.

**DISCUSSION:** [18F]FDG PET and acidoCEST MRI studies can be performed simultaneously. The synergistic combination of assessing glucose uptake and tumor acidosis can improve differentiation of a drug-treated group from a control group during drug treatment of a tumor model.

**REFERENCES:**

1. Chen LQ, Randtke EA, Jones KM, Moon BF, Howison CM, Pagel MD. Evaluations of tumor acidosis within vivo tumor models using parametric maps generated with acidoCEST MRI. Mol Imaging Biol 2015;17(4):488-496. PMID: 25622809, DOI: 10.1007/s11307-014-0816-2.
2. Bos R, van Der Hoeven JJM, van Der Wall E, van Der Groep P, van Diest PJ, Comans EF, Joshi U, Semenza GL, Hoekstra OS, Lammertsma AA, Molthoff CF. Biologic correlates of (18)fluorodeoxyglucose uptake in human breast cancer measured by positron emission tomography. J Clin Oncol 2002;20:379–387.
3. Jones KM, Randtke, EA, Yoshimaru E, Howison CM, Chalasani P, Klein RR, Chambers SK, Kuo PH, Pagel MD. Clinical translation of acidosis measurements with acidoCEST MRI. Molec Biol Imaging 2017;19:617-625.
4. DeFronzo R, Fleming GA, Chen K, Bicsak TA. Metformin-associated lactic acidosis: Current perspectives on causes and risk. Metabolism. 2016 Feb 29;65(2):20-9.

**CEST MRI as new imaging biomarker for acute kidney injury**

Jing Liu[1-3], Zheng Han[3], Yigang Pei[3,4], Peter van Zijl[2,3], Guanshu Liu[2,3]

*[1]Department of Radiology, Guizhou Medical University, Guiyang, Guizhou, China; [2]F.M. Kirby Research Center, Kennedy Krieger Institute, Baltimore, MD, USA; [3]Department of Radiology, Johns Hopkins University School of Medicine, Baltimore, MD, USA; [4]Radiology Department, Xiangya Hospital, Changsha, Hunan, China.*

**INTRODUCTION:** Acute kidney injury (AKI) remains a major complication of renal diseases and is associated with high mortality and rapid progression. Early detection of AKI is challenging as it is generally asymptomatic before severe loss of excretory function or decreased glomerular filtration rate (GFR). In addition, serum biomarkers only become evident after ~50% loss of kidney function[1]. Noninvasive imaging biomarkers for early diagnosis of AKI are urgently needed. In the present study, we aimed to develop a new Magnetic Resonance (MR) imaging biomarker for AKI using the endogenous CEST MR contrast of renal tissues.

**METHODS:** In vivo CEST MRI was conducted on a Bruker Biospec 11.7 T MRI scanner equipped with a mouse brain surface array RF coil using a modified rapid acquisition with relaxation enhancement (RARE) sequence as described previously[3], with $B_1$=1.8 μT, $T_{sat}$=3s, offset ranging from -5ppm to 5ppm, $\Delta\omega$=0.2ppm, TR=5s, TE=6ms, RARE factor=23, slice thickness=1 mm, matrix size=64x64, FOV=22x22 mm. To correct the $B_0$ inhomogeneity, WASSR scans were acquired before and after the CEST acquisitions. AKI mouse models were prepared by i.p injection of 10mg/kg LPS (n=4), i.m injection of 8mL/kg glycerol (50% in saline, n=4) and renal vascular pedicle clamping for 45 min (n=4) respectively in C57BL/6J mice according to standard procedures[1,4]. CEST MRI was performed on day1 after the injection/surgery for LPS-induced AKI model and day 7 for the glycerol-induced and ischemia-reperfusion injury (IRI) models.

**RESULTS:** To investigate whether CEST MRI can be used to detect kidney injuries, we employed three different animal models, *i.e.*, the LPS model for sepsis AKI, glycerol model for rhabdomyolysis AKI, IRI model. The CEST MRI signal in the injured kidneys were characterized using the standard Z-spectral approach[5]. As shown in **Fig. 1A**, injured kidneys showed strikingly decreased CEST contrast (increased normalized water signal $S/S_0$). We then used the CEST contrast at two offsets, 3.5 ppm and -3.5 ppm (**Fig. 1B)**, attributed to Amide Proton Transfer weighted (APTw) effect and relayed Nuclear Overhauser Enhancement weighted (rNOEw) effect respectively, to quantify the extent of impairments. Significant decreases in the endogenous CEST contrast at both offsets were found in all three AKI models (**Fig. 1C)**, indicating CEST MRI has potential as an imaging biomarker for renal injuries.

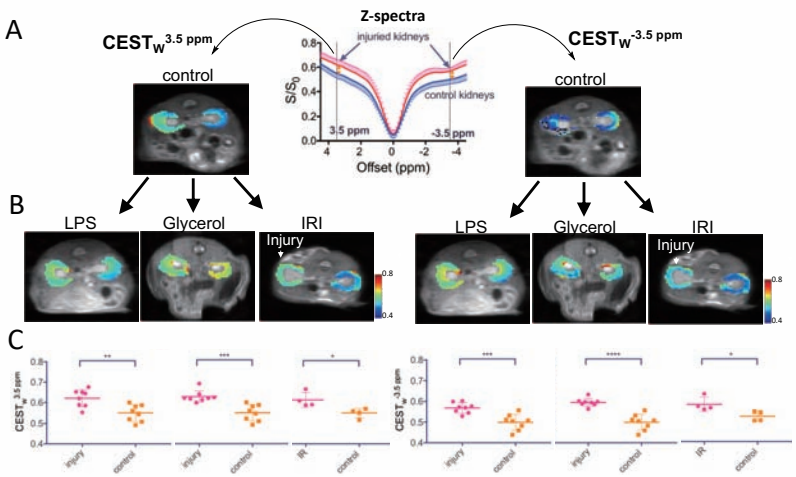



**Fig.1** Illustration of CEST MRI detection of injured kidney. (A) Averaged Z-spectra of LPS-injured and control kidneys and the corresponding CEST-weighted maps. Data is presented as mean±SD. (B) The CESTw maps at 3.5 ppm (left) and -3.5 ppm (right) of kidneys. C statistical analysis revealed the significant difference in the injured kidneys in all three animal models.

**DISCUSSION:** In the present study, we assessed the CEST MRI manifestations quantified by the Z-spectral signal ($S_{sat}/S_0$) at 3.5 ppm (APTw) and -3.5 ppm (rNOEw) in different AKI models. Being sensitive to concentration and exchange rate (and thus pH) of exchangeable protons and aliphatic protons (relayed exchange) in these protein-based signals, CEST MRI was able to assess abnormality on the cellular level[2].

**CONCLUSION:** In summary, the potential of CEST MRI as a new imaging biomarker for acute kidney injuries was proven in three different models. Next, we will continue working on the validation and clinical translation of the developed technology for diagnosing renal diseases.

**ACKNOWLEDGMENTS:** Supported by NIH grants R03EB021573, R01CA211087, R21CA215860, and R01EB015032.

**REFERENCES:** (1) Bellomo, R.*, et al. Crit Care* **2004**, *8*, R204-R212. (2) Liu, G.*, et al. NMR in biomedicine* **2013**, *26*, 810-28. (3) Xu, X.*, et al. Magn. Reson. Med.* **2015**, *74*, 1556-63. (4) Wei, Q.; Dong, Z. *Am J Physiol Renal Physiol* **2012**, *303*, F1487-94.(5) Liu, J.*, et al. NMR in biomedicine* **2018**, 10.1002/nbm.3942, e3942.

# Studies of Chemical Exchange Saturation Transfer on 1.5 T Clinical MRI Scanner

Yong-gui YANG[1], Gang GUO [1]

(1. Dept. of Radiology Imaging, The 2nd Affiliated Hospital of Xiamen Medical College， Xiamen 361021;)

This study aimed to analyze factors affecting the Z spectrum of chemical exchange saturation transfer (CEST). Image acquisitions were carried out in vitro model and clinical cases on a GE Signa HDe 1.5T MRI scanner. The original signal, amide proton transfer (APT) signal and Z spectrum were analyzed from four aspects, including (a) the imaging of tissue, (b) the equipment, (c) the technology, and (d) other factors, respectively. Different imaging parameters including acquisition matrix, number of excitations (NEX), flip angle, CEST flip_remt (the flip angle of magnetization transfer) imaging contrast analysis, and Z flip_remt spectrum were applied respectively. Experimental results show that the signal to noise ratio (SNR) of CEST imaging is relatively low, and the stability and uniformity of the magnetic field, to a certain extent, affect the effect of CEST imaging. The reduction of acquisition matrix, the increase of NEX and flip angle could increase the image SNR. In the case of other parameters unchanged, the CEST effect is the best when the flip angle of magnetization transfer turns at 105º. Also, when NEX=2, the obtained data can basically meet the requirements of the response organization of Z spectrum. Z spectrum model in magnetization transfer frequency ranging -304 to -184 Hz can display 30% Glu, $I_{320}$, $H_2O$, and Cr signal differences. The maximum differences is in the range -244～-214 Hz.The original image signal of 30% $I_{320}$ was significantly higher than that of Glu, $H_2O$, Cr. The signal strength of Cr appears lower than that of Glu, the signal strength of Cr is slightly lower than that of Glu in APT imaging. There were 25 cases of brain tumor amide proton transfer (APT) imaging showing high signal, and 12 cases of cerebral infarction APT imaging showing low signal. Therefore, CEST original imaging can distinguish the lesion area. There were 12 cases of CEST imaging failure due to long acquisition time, patient coordination, environment and room temperature, etc.. In the case of ensuring the stability and uniformity of magnetic field on 1.5 T clinical type MRI scanner, optimal CEST imaging and Z spectral imaging can distinguish the metabolite and its concentration, together with the magnetic transfer frequency range of different metabolites, providing the basis for accurate selection of the magnetization transfer frequency of various metabolites.

**Key words:** Magnetic resonance imaging, Chemical exchange saturation transfer, Amide proton transfer, pH value

**Amide proton transfer imaging in amyotrophic lateral sclerosis patients**

Zhuozhi Dai[1,2], Sanjay Kalra[2], Dennell Mah[2], Peter Seres[2], Hongfu Sun[3], Zhiwei Shen[1], Alan H Wilman[2] and Renhua Wu[1]

*[1]2nd affiliated hospital of Shantou University Medical College, Shantou, Guangdong, China*

*[2]University of Alberta, Edmonton, Alberta, Canada*

*[3]University of Calgary, Calgary, Alberta, Canada*

**INTRODUCTION:** Amyotrophic lateral sclerosis (ALS) is a progressive, fatal disease characterized by the death of neurons controlling voluntary muscle movement. There is lack of objective imaging indicators for ALS diagnosis and assessment. Amide proton transfer (APT) is a versatile imaging technique which can detect amide metabolic changes in brain[1-3]. This study aims to explore the value of APT in the diagnosis of ALS patients and the correlation between APT and diffusion tensor imaging (DTI).

**METHODS:** 32 participants were recruited, including 16 ALS patients and 16 healthy controls. Amide proton transfer imaging and DTI were performed on brain at 3T. Conventional T1- and T2-weighted images as well as radiofrequency and static magnetic field maps were also obtained. Lorentz fitting was introduced to quantify the amide effect. Paired t-tests for APT were calculated between patients and healthy controls, and between different regions within ALS patients. The correlations between APT and diffusion parameters were also measured.

**RESULTS:** In ALS patients, the amide peak is significantly different between motor cortex and control grey matter territories. Compared with healthy controls, the APT signal intensities in ALS were significantly reduced in motor cortex ($P < 0.001$) and corticospinal tract ($P = 0.015$), which was undetectable under routine imaging methods. Compared with the healthy control group, fractional anisotropy (FA) values were declined in both corticospinal tract ($P = 0.024$) and temporal white matter ($P < 0.001$) in ALS patients. While, apparent diffusion coefficient (ADC) was increased in motor cortex ($P = 0.001$), temporal cortex ($P = 0.002$), and corticospinal tract ($P = 0.005$) in ALS patients. In addition, APT was negatively correlated with FA ($r = -0.477$, $P= 0.006$) and positively correlated with ADC ($r = 0.629$ and $P < 0.001$).

**DISCUSSION:** The change of amide peak in APT usually represents the alteration of intracellular protein, which has an intimate relationship with cell activation and proliferation[4]. The alteration of amide may also due to the metabolic reprogramming in ALS.

**CONCLUSION:** This study first detected changes of APT in the motor cortex and corticospinal tract of ALS patients, which has the potential to be an objective imaging biomarker for ALS diagnosis. The combination of APT and DTI can simultaneously detect changes of metabolism and microstructure in ALS patients.

**ACKNOWLEDGMENTS:** Grateful acknowledgment is made to Dr. Mark D Pagel from MD Anderson Cancer Center and Dr. Edward A. Randtke from University of Arizona for technical assistance with pulse sequence implementation. This study was supported in part by grants from Canadian Institutes of Health, the ALS Society of Canada and Brain Canada, and the Natural Science Foundation of China (NSFC 81471730, 31870981).

**REFERENCES:** 1. Zhou J, et al. Nature medicine 2003; 9(8): 1085-90. 2. Jones KM, et al. Journal of Magnetic Resonance Imaging 2018; 47(1): 11-27. 3. Sun PZ, et al. Contrast Media & Molecular Imaging 2014; 9(4): 268-75. 4. Zhou J, et al. Nature Medicine 2010; 17(1): 130-4.

# Amide Proton Transfer-Weighted MRI Signal as a Surrogate Biomarker of Ischemic Stroke Recovery in Patients with Supportive Treatment

Lu Yu[1,2], Yuhui Chen[3], Min Chen[1], Xiaojie Luo[1], Shanshan Jiang[4], Yi Zhang[5], Haibo Chen[3], Tao Gong[3], Jinyuan Zhou[4], and Chunmei Li[1*]

[1] Department of Radiology, Beijing Hospital, National Center of Gerontology, Beijing, China
[2] Graduate School of Peking Union Medical College, Beijing, China
[3] Department of Neurology, Beijing Hospital, National Center of Gerontology, P.R. China, Beijing, China
[4] Division of MR Research, Department of Radiology, Johns Hopkins University, Baltimore, MD, USA
[5] Center for Brain Imaging Science and Technology, Key Laboratory for Biomedical Engineering of Ministry of Education, College of Biomedical Engineering & Instrument Science, Zhejiang University, Hangzhou, Zhejiang, China

**Background:** Amide proton transfer-weighted (APTw) MR imaging has shown great potential in the evaluation of stroke severity because of its sensitivity to acid environments. However, this promising MRI technique has not been used to assess treatment efficacy with regard to stroke recovery.

**Purpose:** To assess the therapeutic effect of supportive treatment in ischemic stroke patients using the pH-sensitive amide proton transfer-weighted (APTW) MRI technique.

**Material and Methods**: Forty-three ischemic stroke patients at an early stage were recruited and scanned with conventional and APTW MRI sequences at 3T before treatment. After treatment, 26 patients underwent a follow-up MRI scan (one to three times on different days). The magnetization-transfer-ratio asymmetry at 3.5 ppm (usually called APTW) was measured. The APTW signal changes following treatment were analyzed.

**Results**: Baseline APTW signal intensities in the infarcted lesions inversely correlated with baseline stroke severity. Lesion APTW values gradually increased with time in 24 cases (92.3%) with a follow-up MRI scan, showing clinical symptom improvements. Two cases (7.7%) showed further decreased APTW signal in the follow-up scan, accompanied by clinical symptom aggravation. Compared to the baseline, significant APTW signal increases were found for all post-treatment patients (efficacious), whether based on post-treatment or on stroke onset times. The increase in APTW signal in the ischemic stroke lesion after treatment was associated with an improvement in clinical symptoms.

**Conclusion**: The APTW signal would be a useful imaging biomarker by which to assess the therapeutic efficacy of ischemic stroke treatment.

**Key words**: Ischemia, Stroke, Infarction, Acidosis, Magnetic resonance imaging

**Chemical Exchange Saturation Transfer MR Imaging of Malignant and Benign Head and Neck Tumors at 3.0T**

Lu Yu[1,2], Min Chen[1,2*], Chunmei Li[1]

[1] Department of Radiology, Beijing Hospital, National Center of Gerontology, No. 1 Da-Hua Road, Dong Dan, Beijing 100730, China

[2] Peking Union Medical College, No. 9 Dong Dan San Tiao, Beijing 100730, China

***Purpose:*** The purpose of this study was to prospectively evaluate the feasibility and capability of chemical exchange saturation transfer (CEST) MR imaging for characterization of head and neck tumors at 3.0T.

***Procedures:*** Twenty-nine consecutive patients with suspected head and neck tumors were enrolled in this study and underwent CEST MRI on a 3.0 T MRI scanner. The patients were divided into malignant (n=16) and benign (n=13) groups, based on pathological results. A map of magnetization-transfer-ratio asymmetry at 3.5 ppm [$MTR_{asym}$(3.5ppm)] was generated for each patient. Interobserver agreement was evaluated and comparisons of $MTR_{asym}$(3.5ppm) were made between the malignant and benign groups. The independent sample Student's t test was performed to evaluate the difference in $MTR_{asym}$(3.5 ppm), MTR(15.6 ppm) and total $MTR_{asym}$ between the malignant and benign groups. Receiver operating characteristic (ROC) analysis was used to determine the appropriate threshold value of $MTR_{asym}$(3.5ppm) for differentiating malignant from benign tumors.

***Results:*** Interclass correlation coefficients (ICC) of malignant and benign groups were 0.96 and 0.90, respectively, which indicated a good interobserver agreement. $MTR_{asym}$(3.5ppm) was significantly higher for malignant group (3.66±1.15%) than for benign group (1.94±0.93%, $P < 0.001$). There was apparent CEST effect from 1ppm to 4ppm both in malignant and benign groups and the total $MTR_{asym}$ signal of malignant group was significantly higher than that of benign group (7.40±2.20% vs 3.92±2.70%, P=0.001). However, there was no significant difference of MTR(15.6 ppm) between malignant and benign group (18.4±3.55% vs 18.11±9.41%, P=0.91). $MTR_{asym}$(3.5ppm) in discriminating these two groups revealed an area under curve (AUC) of 0.904, with a sensitivity of 81.3%, a specificity of 92.3%, and an accuracy of 86.2%, at the threshold $MTR_{asym}$(3.5 ppm) of 2.62%.

***Conclusion:*** CEST MRI is feasible for use in the head and neck tumors and is a valuable imaging biomarker for distinguishing malignant from benign lesions.

## Artifacts in dynamic CEST MRI due to motion and field shifts.

Moritz Zaiss[1], Kai Herz[1], Anagha Deshmane[1], Mina Kim[2], Xavier Golay[2], Tobias Lindig[3], Benjamin Bender[3], Ulrike Ernemann[3], Klaus Scheffler[1,4]

*[1]High-field Magnetic Resonance Center, Max Planck Institute for Biological Cybernetics, Tübingen, Germany.*
*[2] Brain Repair & Rehabilitation, Institute of Neurology, University College London, United Kingdom*
*[3]Department of Diagnostic and Interventional Neuroradiology, University Tübingen, Tübingen, Germany.*
*[4]Department of Biomedical Magnetic Resonance, University Tübingen, Tübingen, Germany.*

**INTRODUCTION:** Dynamic CEST studies such as dynamic glucose enhanced imaging, have gained a lot of attention recently, as it monitors the uptake and wash-out of glucose shown in tumor models in animals (1,2) and patients with glioblastoma (3,4). The expected CEST effects after injection are rather small in tissue especially at clinical field strengths (1-2 %). Small movements during the dynamic CEST measurement together with a subtraction-based evaluation can lead to pseudo CEST effects of the same order of magnitude. These artifacts are studied herein.

**Methods:** A 3D snapshot-CEST acquisition (5) optimized for 3T consisted of a pre-saturation module of 5 s followed by a readout module of duration $T_{RO}$ = 3.5 s. (FOV=220x180x48 mm$^3$, 1.7x1.7x3mm$^3$, TE=2 ms, TR=5 ms, BW=400 Hz/pixel, 18 slices, FA=6° and elongation factor E=0.5 (rectangular spiral reordered). The CEST saturation period consists of 1 Gaussian-shaped RF pulse, using a pulse duration of $t_{pulse}$ = 100 ms, and mean $B_1$ = 3 µT.A separate WASABI measurement was acquired for $B_0$ and $B_1$ mapping (6). A brain tumor patient 3D-CEST baseline scan without glucose injection performed at 3T is used to generate a virtual dynamic measurement introducing different kinds of simulated motion and $B_0$ shifts. All subject measurements were performed after informed written consent and fulfilling all institute policies.

**Results:** Virtual difference images after the rigid body transformations were calculated (not shown here) for translations only, rotations only and B0 shifts only. Typical motion artifacts visible as bright-dark patterns are observed in healthy and tumorous tissue. In a worst case scenario such minor motion (0.6 mm translations) and B0 artifacts (7 Hz shift) can lead to pseudo effects in the order of 1% in dynamic CEST imaging (Figure 1), despite no glucose was injected at all.

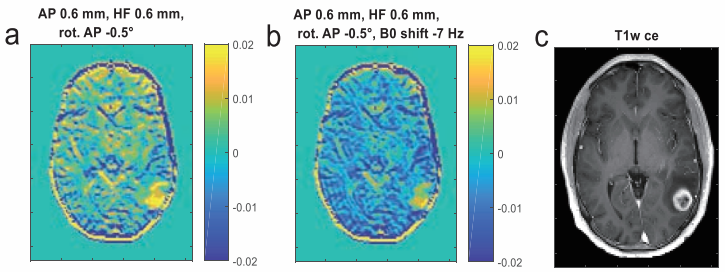



Figure 1: Difference of the saturated image before and the same image after virtual rigid body transformation. (a,b) Worst case scenarios for difference images of a dynamic CEST contrast (a,b) showing signal in the tumor region similar to the gadolinium contrast-enhancement (c). Abbreviations: RL left-right, AP anterior-posterior, HF head-foot.

**Discussion**: Especially around tissue interfaces such as CSF borders or tumor affected areas, the pseudo CEST effect patterns are non-intuitive and can be mistaken as dynamic agent uptake. Mitigation and correction strategies are discussed.

**Conclusion:** Correction or mitigation even of small motions is crucial for dynamic CEST imaging, especially in subjects with lesions.

**REFERENCES**

(1) Walker-Samuel et al. Nat Med 2013;19:1067–72.
(2) Xu X, et al Magn Reson Med 2015;74:1556–63.
(3) Xu X, et al Tomography 2015;1:105–114.
(4) Schuenke P et al Scientific Reports 2017;7:42093.
(5) Zaiss et al. NMR Biomed 2018;31:e3879.
(6) Schuenke P et al. Magnetic Resonance in Medicine 2017;77:571–580.

**Investigation of Anterior Cingulate Cortex APT values in patients with obsessive-compulsive disorder**

Yan Li[1], Naying He[1], Chencheng Zhang[2], Yi Zhang[3, 4], Jinyuan Zhou[4] , and Fuhua Yan[1]

*1 Department of Radiology, Ruijin Hospital,Shanghai Jiao Tong University School of Medicine, Shanghai, People's Republic of China 2 Department of Functional Neurosurgery, Ruijin Hospital,Shanghai Jiao Tong University School of Medicine, Shanghai, People's Republic of China 3 College of Biomedical Engineering and Instrument Science, Zhejiang University, Hangzhou, Zhejiang, People's Republic of China 4 Department of Radiology, Johns Hopkins University School of Medicine, Baltimore, MD, United States*

**INTRODUCTION:** Obsessive-compulsive disorder (OCD) is a neuropsychiatric disease characterized by obsessive thoughts and compulsive behaviors [1]. The prevailing model of OCD pathophysiology focuses on the cortico-striato-thalamo-cortical circuits, and anterior cingulate cortex (ACC) is a critical region in the circuit [2, 3]. The present study aimed to investigate changes in endogenous mobile proteins and peptides in the ACC using Amide Proton Transfer Weighted (APTW) imaging technique in OCD.

**METHODS:** Twenty-two OCD patients (age: 29.0±8.2, M/F: 16/6) and twenty-five healthy controls (HC, age: 29.4±5.9, M/F: 16/9) were recruited for this study. All subjects provided written informed consent. MR scanning was performed on a 3.0 T Ingenia MRI scanner (Philips, Best, the Netherlands), using a fifteen-channel head coil. APTW imaging was based on a single-shot, turbo-spin-echo readout sequence with the following parameters: TR=3000 ms, TE=5.6 ms, turbo factor=54, field of view=256 × 256 mm, matrix size=100 × 100, slice thickness= 4.4mm, acquisition time =192 s. We used four 200ms continuous RF saturation pulses (inter-pulse delay=10 ms, power level=2 μT). The axial scanning plane was parallel to the anterior commissure-posterior commissure (AC-PC) line, superior to the level of anterior cingulate cortex, and 5 continuous slices were acquired in the inferior-superior direction. Each ROI (ACC region, as shown in Figure 1) was carefully drawn and measured three times and the averaged values were analyzed for group comparison using independent samples t-test analysis. The relevance between APT values and patients' age of onset and clinical symptoms of OCD (as assessed by Y-BOCS, HAMD and HAMA Scales) were analyzed by Pearson correlation. The statistical significance level was set at $p<0.05$.

**RESULTS:** We found that APT values in ACC were increased in OCD patients compared to controls (OCD: 0.33±0.20, NC: 0.17±0.11, p=0.002, Table 1). APT values and age of onset were positively correlated ($p< 0.05$), but there was no significant correlation between APT values and Y-BOCS, HAMA or HAMD-17, as shown in Table 2.

**DISCUSSION:** ACC is intricately connected to the basal ganglia via the cortico-basal ganglia-thalamo-cortical loops, our results are consistent with current theories suggesting that OCD results from an imbalance between the "direct" and "indirect" pathways through the basal ganglia [4-6]. Our findings show increased endogenous mobile proteins and peptides of ACC in the patients with OCD. This suggests that the concentration of endogenous mobile proteins has some relationship with the process of OCD, partially support the prevailing CSTC models of OCD. APTW may offer additional insight into investigating signal changes in patients with OCD and help guide our understanding of the circuits involved.

**CONCLUSION:** In conclusion, APTW imaging, as a noninvasive MRI method, can show abnormal metabolite levels based on increased proteins and peptides in the ACC in OCD, indicating it may be a promising diagnostic and monitoring tool for OCD.

**REFERENCES:**

1. American Psychiatric Association. 2013.
2. Menzies L, et al. Neuroscience & Biobehavioral Reviews, 2008, 32(3):525-549.
3. Milad M R, et al. Trends in Cognitive Sciences, 2012, 16(1):43-51.
4. Fitzgerald K D, et al. Biological Psychiatry, 2010, 68(11):1039-47.
5. Schlösser R G M, et al. Human Brain Mapping, 2010, 31(12):1834-1850.
6. de Wit S J, et al. American Journal of Psychiatry, 2013, 171(3):340-349.

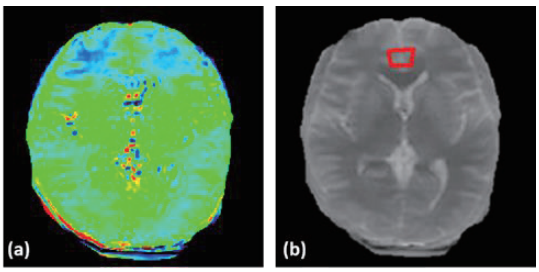



**Figure 1** (a) In pseudo-color APTW images, the signals were displayed as red-to-blue in a descending sequence; (b) Examples of the definition of regions of interest for quantitative analysis: ACC

**Table 1. ACC APT values in OCD and HC groups**

| | OCD (n=22) | HC (n=25) | | |
|---|---|---|---|---|
| ***MRS metabolite*** | ***Mean ± SD*** | ***Mean ± SD*** | ***t(df)*** | ***P*** |
| GABA+ | 0.33± 0.20 | 0.17 ± 0.11 | -3.458(32.283) | **0.002*** |

**p < 0.05.*

**Table2 Correlational analysis between APT values and demographic variables in the OCD patients**

| ***Substances*** | ***Age of Onset*** | ***Y-BOCS*** | ***HAMA*** | ***HAMD-17*** |
|---|---|---|---|---|
| APT values | 0.476 | 0.159 | 0.299 | 0.180 |
| *P* | **0.029*** | 0.481 | 0.177 | 0.422 |

**p < 0.05.*

**Prediction Grades and proliferation activity in meningioma using Amide proton transfer-weighted MRI**

Hao Yu[1,2], Yueqin Chen[2], Xianlong Wang[1], Guqing Zhang[2], Shanshan Jiang[1,3], Jinyuan Zhou[3], and Zhibo Wen[1]

[1]Department of Radiology, Zhujiang Hospital of Southern Medical University, Guangzhou, Guangdong, China, [2]Department of Radiology, Affiliated Hospital of Jining Medical University, Jining, Shandong, China, [3]Department of Radiology, Johns Hopkins University School of Medicine, Baltimore, MD, United States

**Introduction**

Meningioma constitute approximately 36.7% of all primary central nervous system neoplasms[1]. Its therapeutic method and prognosis was related to tumor grade and proliferation[2-5]. Conventional MRI is not enough to reflect the pathology character deeply. APT imaging is used to detect the amide protons of endogenous, low-concentration mobile proteins and peptides in tissue[6]. We aimed to explore if this technique was useful in comprehensive evaluation the meningioma.

**Methods**

79 patients performed conventional and APTw sequence on a 3.0 T MRI system preoperatively. APTwmax, APTwmin, APTwmax-min and APTwmean were recorded from the solid component at the maximal slice of the tumor. Independent-Samples T test followed by the Levene test was used to compare differences of 4 parameters between WHO grade I and WHO grade II meningioma group. Pearson's correlation coefficient was used to analyze the association between APTwmax and Ki-67 index. $P<0.05$ was considered to be a statistically significant difference for all tests.

**Results**

The APTwmin value for grade II meningiomas was higher (2.84%±0.56% vs. 2.48%±0.50%, P=0.005) and the APTwmax-min value was lower (0.68%±0.22% vs. 0.93%±0.31%, P<0.001) than the same parameters for grade I tumors (Fig.1,2 ). By using APTwmax-min as a discriminative index, the sensitivity and specificity were 64.2% and 88.5%, the accuracy was 72.2%, respectively. The regression equation for the Ki-67 index (Y) and APTwmax (X) was Y=0.063X-0.161 (F=77.598, P<0.001, $R^2$=0.502) .

**Discussion**

According to the technologic of APTw, the tumor core of WHO grade II meningiomas had greater cell densities and mobile protein and peptide content than WHO grade I meningiomas, and the different architectural and cytologic features result in different distribution of protein between different grade of meningiomas.

**Conclusion**

APTw MRI could assess meningioma on the level of cell and molecule, and provide more precise and microscopic of functional diagnostic information.

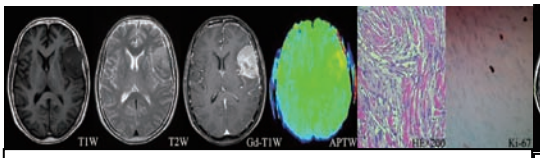



Fig.1: A 39-year-old male with fibroblastic meningioma (WHO grade I)
. APTwmax=3.18%, APTwmin= 2.06% APTwmax-min= 1.12%, APTwmean= 2.63%, Ki-67=3%

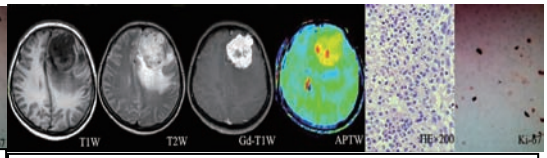



Fig.2: A 49-year-old female with atypical meningioma (WHO grade II)
APTwmax=4.02%, APTwmin= 3.31% APTwmax-min= 0.71%, APTwmean= 3.87%, Ki-67=10%

1 Louis DN et al Acta neuropathologica 131:803-820
2 Lin Z et al. World neurosurgery 100:395-406
3 Marciscano AE et al. Journal of neurosurgery 124:106-114
4 Romani R et al. Acta Neurochir (Wien) 156:1837-1845
5 Santelli L et al Acta Neurochir (Wien) 152:1315-1319; discussion 1319
6 Zhou Jet al Magn Reson Med 50:1120-1126

## The Histogram Analysis of Amide Proton Transfer-Weighted (APTw) Imaging for Differential Diagnosis of Prostate Cancer

Yue Lin[1], Chunmei Li[1], Jinyuan Zhou[2], Min Chen[1]

[1]Department of Radiology, Beijing Hospital, National Center of Gerontology, Beijing, and China

[2]Department of Radiology, Johns Hopkins University, Baltimore, USA

**INTRODUCTION:** Prostate cancer (PCa) is the second most common cancer and the sixth leading cause of cancer deaths in men. Amide Proton Transfer-weighted (APTw) imaging based on histogram analysis can provide more quantitative information for differentiating prostate cancer.

**PURPOSE:** To prospectively evaluate the feasibility of APTw imaging based on histogram analysis in differentiating prostatitis and PCa.

**METHODS:** A total of 36 patients pathologically confirmed (including 14 foci of PCa and 27 foci of prostatitis) underwent preoperative APTw-MRI. Histogram metrics including standard deviation (Std), skewness, kurtosis, minimum (Min), maximum (Max), and percentiles (10, 25, 50, 75, 90th) were extracted from APTw maps. All histogram metrics between PCa and prostatitis were compared using Student *t* test. For significant parameters, receivers operating characteristic curve (ROC) analyses were further performed for prostate cancer.

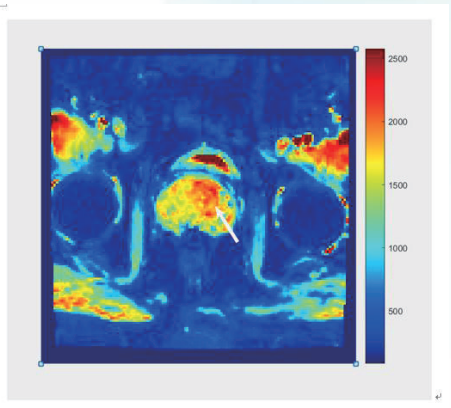
**RESULTS:** The Std, Max, percentiles (25, 50, 75, and 90th) of APTw maps between the groups were significant differences (all $P < 0.05$). Area under the ROC curve (AUC) of the Std, Max, range, 25, 50, 75, and 90th percentile of APTw maps for identifying prostate cancer was 0.75,0.81, 0.698, 0.742,0.788 and 0.815 (all $P < 0.05$), respectively;

**DISCUSSION:** APTw could provide indirect acquisition of signal intensity through the chemical exchange between amide protons in mobile proteins and peptides and bulk water protons. In PCa, the mobile proteins and peptides are more abundant than in prostatitis.

**CONCLUSION:** Histogram analysis of APTw map can be used to differentiate prostatitis and PCa and provide more quantitative information.

**REFERENCES:**

1. Suo S, et al; Magn Reson Imaging 2014;32(5):421-427.
2. Zhang YD, et al; Eur Radiol 2015;25(4):994-1004.




APT

A 78-year-old man with surgically verified prostate cancer

## Amide Proton Transfer Imaging of the Recurrent Malignant Gliomas: Possible Feasibility Assessing Chemotherapy Response

Qihong Rui[1], Hao Yu[1], Yaoming Qu[1], Xianlong Wang[1], Yingjie Mei [2], Shanshan Jiang[3], Jinyuan Zhou[3], and Zhibo Wen[1]

1 Department of Radiology, Zhujiang Hospital of Southern Medical University, Guangzhou, China,

2 *Philips Healthcare, Guangzhou, Guandong, China*

*3* Division of MR Research, Department of Radiology, Johns Hopkins University School of Medicine, Baltimore, MD, United States

**INTRODUCTION:**

Bevacizumab was approved by the FDA for the treatment of recurrent or progressive glioblastoma (GBM). Although imaging responses are typically assessed by gadolinium-enhanced MRI, studies[1,2] have revealed that linear GBCA gadopentetate dimeglumine prone to deposit in the denate nucleus and the globus pallidus. APT is a novel functional modalities without GBCA, used to detect the amide protons of endogenous, mobile proteins and peptides in tissue. In this study, we sought to demonstrate preliminary results on APT changes in recurrent gliomas after treatment with bevacizumab.

**METHODS:**

Local Ethics Committee approved the study, and informed consent was obtained from all patients. Patients with recurrent malignant glioma were included. Routine MRI scan as well as APT were underwent before and every 4 weeks after bevacizumab treatment. All MR scans were performed on a clinical 3.0T scanner (Ingenia, Philips). APT imaging was implemented using a 3D_TSE_DIXON sequence[3] with following parameters: TR\TE: 4600\6ms; FOV: 212×212×83.6mm$^3$; voxel size: 1.53×1.77×4.4mm$^3$; saturation power: 2μT; RF saturation of 2 seconds was achieved by using multi-transmit techniques; frequency offsets: ±2.7ppm, ±3.5ppm; ±4.28ppm and -1540ppm; scan duration: 4:20min. B0 correction was performed with intrinsic B0 mapping. APT value was calculated automatically on console. The regions of interst (ROI) were manually circumscribed in APTw image around the largest crosssectional area of the tumour, according to the Gd-T1w image or FLAIR image.

**RESULTS and DISCUSSION:**

Fine patients with recurrent glioma were studied. APT value increased in the three patients with progressive disease and decreased in the two patients with a partial or complete response (Figure 1 and 2).

**CONCLUSION:**

Amide proton transfer imaging may have the potential for assessing the effect of therapy on recurrent malignant gliomas treated with bevacizumab. However more patients need to be included in the study for statistical analysis.

**REFERENCES:**

1. Kanda, T., et al. High Signal Intensity in the Dentate Nucleus and Globus Pallidus on Unenhanced T1-weighted MR Images: Relationship with Increasing Cumulative Dose of a Gadolinium-based Contrast Material. RADIOLOGY 2014; 270(3): 834-841.

2. Ramalho, J., et al. High Signal Intensity in Globus Pallidus and Dentate Nucleus on Unenhanced T1-weighted MR Images: Evaluation of Two Linear Gadolinium-based Contrast Agents. RADIOLOGY 2015. 276(3): 836-844.

3. Jochen Keupp, Jinyuan Zhou, and Osamu Togao. 3D Clinical APTw MRI with Improved Contrast Homogeneity. #1506, 2016 ISMRM.

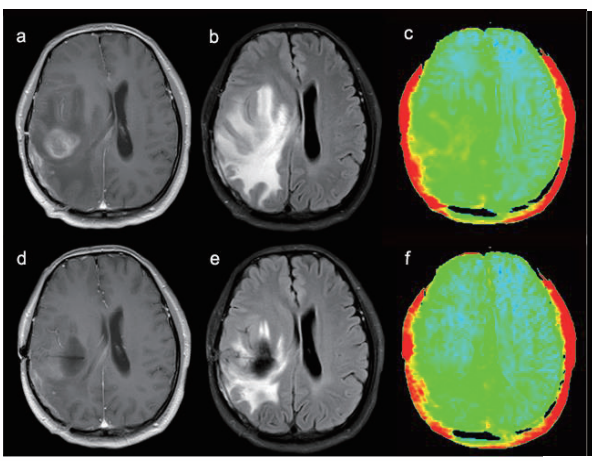



Figure 1: A 42-year-old male with recurrent glioma sarcomatosum (WHOⅣ) in the right temporal lobe. Images before( a, b, c) and after ( d, e, f) three times bevacizumab chemotherapy for a patient achieving complete response.

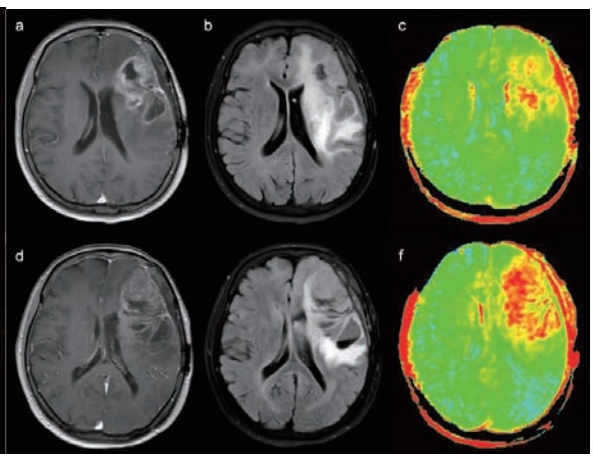



Figure 2: A 58-year-old female with recurrent oligodendroglioma in the left frontal lobe. Images before (a, b, c) and after (d, e, f) two times of bevacizumab chemotherapy for a patient with progressive disease.

# An overview of CEST sequence on GE MR platform

Bing Wu
GE Healthcare, Waukesha, USA

The realization of CEST pulse sequence mainly consists of two parts: saturation and acquisition. In this brief overview, introduction will be given on the currently available options of saturation and acquisition on GE MR platform.

## RF saturation

The preferred CEST saturation length lies within the range of seconds and the strength used is in the order of micro-tesla. Long and strong RF have impacts on both the RF transmission or amplifier and the specific absorption rate (SAR) limits. Instead of simply stretching the saturation pulses, many RF designs have been proposed and tested on scanners in order to best meet the needs of CEST saturation while stay within the safe constraints of RF transmission and SAR. There are currently three main types of saturation implementation on GE platform: continuous saturation, pulsed saturation and pseudo-continuous saturation. Flexible design of the RF length, strength and inter-pulse gap is offered in continuous and pulsed saturation implementation.

## Data acquisition

A distinctive requirement of CEST is the series of acquisitions at a range of different frequency offsets. Typically, somewhat 20 ~ 50 saturation frequency offsets are acquired. This place a practical constrain in the clinical acquisition and the total scan time would be what is needed for single acquisition times total number of saturation frequencies.

Different types and methods of acquisitions have been experimented and implemented. Different acquisition types could be mainly categorized by 2D or 3D acquisitions. 2D acquisitions including FGRE, FSE, gradient echo EPI, spin echo EPI and single shot FSE have been implemented. Whereas 2D single slice acquisition is most time efficient, it limits the scan coverage and requires the user to carefully select the plane to imaged. 3D acquisition is clearly more desirable; it however significantly lengthens the scan time. Currently, time efficient acquisition strategies such as 3D spiral, reduced filed-of-view 3D FSE, 3D radial acquisitions have been realized and attempted on GE platform.

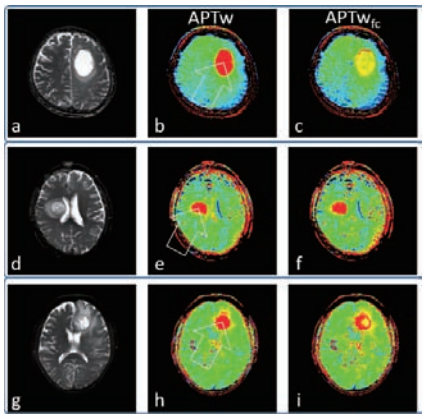
The search for an optimal combination between saturation and acquisition strategy is continually being conducted. Strong clinical evidence would drive efforts in improving the overall realization efficiency of CEST.

**A review of APTw pulse sequences and experimental results on Philips MRI scanners**

Jochen Keupp
*Philips Research, Hamburg, Germany*

**INTRODUCTION:** Amide Proton Transfer weighted (APTw) MRI is based on tissue endogenous protein levels with a large potential for tumor tissue characterization and treatment follow-up assessment. Here, acquisition sequences, RF saturation settings and standardized visualization of APTw contrasts are reviewed, as used in the 3D APT neuro oncology solution for Philips MRI systems. Furthermore, a research metric for APTw imaging is discussed, which suppresses fluid areas based on the background magnetization transfer ratio.

**METHODS:** APTw MRI parameter choices for neuro oncology comprise: 3D fast spin echo sequences (TSE), using Cartesian radial-out phase encoding steps and driven equilibrium refocusing (max.120°), FOV 230×180 $mm^2$ , 10 slices, voxel 1.8×1.8×6 $mm^3$, TR/TE = 6s/7.8ms, SENSE R=1.6, SPIR fat suppression, 9 Z-spectral images S[ω] with volumes at +3.5ppm (3 echo shifts ±0.4ms) additionally used for intrinsic Dixon-type $B_0$ mapping [1], acquisition time 3min 45s. RF saturation ($T_{sat}$=2s) at an RF duty-cycle (RF-DC) of 100% and a power level of $B1_{rms}$=2.0 μT is imposed by alternation of two independent RF transmission channels [2]. 3.0T MRI scanners (Achieva TX/Ingenia, Philips Healthcare, Netherlands) with 2-channel body coil transmission and 8-channel head coil reception are used. APTw images are displayed on the console in a rainbow-type color scale ranging from green to red, which is standardized across all APTw images (±5% max.). For fluid suppression, the following research metric is used [3]: $APTw_{fc} = MTR_{asym}[\Delta\omega] \times \varepsilon \times (MTR[\Delta\omega] + MTR[-\Delta\omega])$ , with Δω=3.5ppm and ε=1.0 chosen for the current saturation settings. In the retrospective study [3], data from N=12 brain tumor patients were processed, acquired with 2D single-shot TSE, 25×S[ω] (ω=−6…6ppm), SENSE R=2, TR/TE = 5s/6.2ms, acquisition time 2½ min.




**RESULTS:** With the 3D APT protocol, low APTw values (close to 0%, green/blue) and low standard deviation around 0.5% was obtained over normal brain areas, while high grade tumors show strong contrast (>2%, yellow/red). Examples for the fluid suppression are shown in Fig.1: Tumor with large central fluid content (a/b/c) with thin rim enhancement after fluid correction; solid tumor (d/e/f) with no apparent contrast change by fluid correction; confirmed glioblastoma (g/h/i) with a fluid portion (necrosis) at the tumor center, which shows reduced contrast when applying the metric. Cystic/necrotic areas are suppressed (6.4±1.8%⇒3.4±1.5%, $P<10^{-4}$) while solid tumor values are very similar (4.5±1.3%⇒4.8±1.1%, P=0.06).

**DISCUSSION:** An evaluation of different $T_{sat}$ in APTw clinical brain tumor imaging showed, that the tumor tissue contrast ($\Delta MTR_{asym}$) is enhanced with increasing $T_{sat}$ from 0.5 s up to 2 s [4]. Long $T_{sat}$, limited by water relaxation $T1_w$, allows the contribution of multiple exchange processes to the APTw contrast, as long as the RF saturation is quickly reinstated after each exchange process, when the NH group has received an unsaturated proton from water. Thus, 100% RF-DC (no gaps) is favorably used, enabled by alternated transmission via 2 amplifiers. Tumor tissue contrast $\Delta MTR_{asym}$ has been shown to be almost constant in the range of $B_{1,rms}$=1 to 3 μT [5]. Advantages of choosing a saturation power level of $B_{1,rms}$ =2 μT are: (1) Close to 0% APTw contrast in normal brain tissue with APTw hyper-intensity in high-grade tumors and (2) minimized NOE effects at 3.0 T [6,7]. The standardized color coded APTw reading allows straightforward integration into routine radiology procedures. All acquired image contrasts are viewed in concert, aiding to identify potential solid tumor areas via anatomical T1w/T2w or fluid enhanced FLAIR images that can be scored for APTw hyper-intensity (yellow/red) to assist tumor grading. The fluid suppressing $APTw_{fc}$ metric may further aid to selectively visualize solid tumors. It conserves numerical values of APTw in solid tissues, as in Fig1.d/e/f. No extra acquisition time is needed, because the metric can be computed from the minimum Z-spectral data required for standard APTw MRI.

**CONCLUSION:** The proposed APTw MRI parameters and visualization may serve as a standard for neuro oncology.

**ACKNOWLEDGMENTS:** Osamu Togao (Kyushu University Hospital), Kim van de Ven (Philips Healthcare).

**REFERENCES**: *[1] Togao O et al. MRM 77, 2272 (2017). [2] Togao O et al. Neuro Oncol 16, 441 (2014); [3] Keupp J, Togao O. ISMRM 26, 3156 (2018) 3156; [4] Togao O et al. PLoS One 11, e0155925 (2016); [5] Zhao X et al. MRM 66, 1033 (2011); [6] Keupp J et al. ISMRM 23, 1001 (2015); [7] Zhou J et al. MRM 70, 320 (2013)*

**A review on CEST pulse sequences and experimental results on Siemens MRI scanners**

Yi Zhang[1,2]
[1]Deparmtent of Biomedical Engineering, Zhejiang University, Hangzhou, Zhejiang, China
[2]Department of Radiology, Johns Hopkins University, Baltimore, Maryland, USA

**Purpose:** Amide Proton Transfer (APT) MRI[1] is a type of Chemical Exchange Saturation Transfer (CEST)[2] imaging that shows promise in applications including cancer[3, 4] and stroke[5]. However, routine APT MRI is limited by its relatively long scan times since APT MRI typically requires multiple image acquisitions. Currently, the only available approaches for accelerating APT imaging on commercial scanners are parallel imaging techniques[6-8], such as SENSE[7]. However, in practice conventional SENSE can accelerate APT imaging by only a factor of about 2[3, 9], due to the reconstruction accuracy and underlying signal-to-noise ratio (SNR) of the APT signal. SENSE reconstruction depends critically on the accuracy of the sensitivity maps used for unfolding. The standard way to generate sensitivity maps (preset by the scanner manufacturer) is to acquire a separate reference scan using a different MRI protocol and geometric offsets than those used for the APT scans. This introduces errors in the standard sensitivity maps which manifest as unfolding artifacts that limit the acceleration factor. Here, a novel acquisition and reconstruction method, vSENSE[10], is applied to accelerate APT source images up to 8-fold.

**Methods:** Pathology-confirmed brain tumor patients were studied on a 3T MRI scanner with a 32-channel head coil. APT contrast was achieved using 0.8s saturation duration, 2μT saturation power, and turbo-spin-echo (TSE) readout. The vendor-preset sensitivity reference scan was also implemented with raw k-space data saved. Standard SENSE reconstruction was first performed by: (A1) interpolating sensitivity maps from the vendor's preset reference scan; (A2) undersampling the full k-space by increasing the phase-encoding (PE) gradient step size for every APT saturation frame, resulting in folded images; and (A3) unfolding images using the SENSE method[7].

vSENSE reconstruction was next performed as follows: (B1) One of the APT saturated frames was selected to retain a substantial portion of k-space data (typically the saturated 3.5ppm frame). (B2) Accurate sensitivity maps were generated from the selected frame and reference scan using the self-consistent incoherence absorption or artifact suppression strategy[10]. (B3) The other saturated frames were variably-undersampled for different acceleration factors (R=2 at ±3.5ppm, R=4 at the other frequencies) by increasing the step size of the PE gradient steps. (B4) The sensitivity maps from step B2 were then applied to the variably-undersampled datasets to reconstruct vSENSE images.

**Results and Discussion:** Fig. 1 from a brain tumor patient shows a conventional R=4 SENSE APT-weighted (APTw; part c) and source (part e) images, that are corrupted vs. the standard full k-space result (part b). The R=4 vSENSE APTw (part d) and source (part f) images are uncorrupted and consistent with the full k-space ones. Even when conventional SENSE is implemented using the same variable undersampling of frames as vSENSE, the resultant z-spectrum (part g, dashed red) is error prone ($\leqslant$ 9.4%) compared to the standard full k-space z-spectrum (parts g and h, solid blue), and the vSENSE method (part h, dashed red), which are indistinguishable (part h).

The proactive application of vSENSE to 3D CEST imaging on a healthy volunteer is shown in Fig. 2, which signifies the importance of using the vSENSE method for generating APTw images. vSENSE removed the significant artifacts on APTw maps from SENSE reconstruction using identical k-space data (Figs. 2c vs. 2b), and supported acceleration factors up to 8 for different frames of source images.

**Conclusion:** The vSENSE method variably undersamples the multiple images of data sets that are commonly needed to quantify various MRI parameters. Here, an up to 8-fold acceleration was demonstrated for APT imaging. By using one substantially-sampled image frame acquired under the appropriate scan conditions from each set, the vSENSE method guarantees more accurate sensitivity maps and unfolded images than those using conventional SENSE implementation.

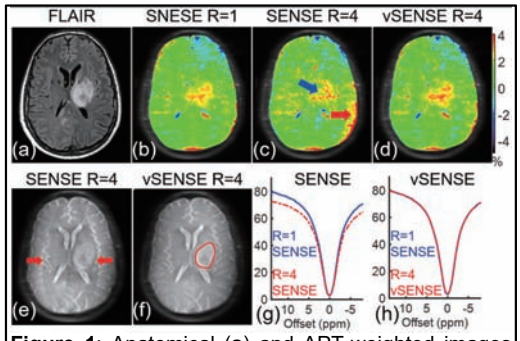



**Figure 1**: Anatomical (**a**) and APT-weighted images (**b-d**) from a brain tumor patient. APT-weighted images from SENSE (**c**) and vSENSE (**d**) were calculated from raw images shown in (**e**) and (**f**), respectively. SENSE (**g**) and vSENSE (**h**) z-spectra from the selected region (red circle in **f**) were compared to full k-space spectra. Blue arrows indicate tumor region. Red arrows indicate SENSE-reconstruction artifacts.

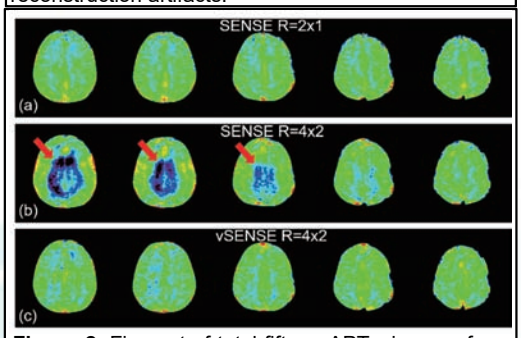



**Figure 2**: Five out of total fifteen APTw images from a normal volunteer using reference SENSE with R=2x1 (a), proactive SENSE with R=4x2 (b), and proactive vSENSE with R=4x2 (c). The reference SENSE reconstruction used an R factor of 2x1 for all frames (a). Both proactive SENSE and vSENSE used R factors of 4x2 for the $S_0$, ±3ppm, ±4ppm and the first set of ±3.5ppm frames, and of 2x1 for the second set of ±3.5ppm frames. The CEST data was acquired with a 3D TSE sequence using slice-selective refocusing pulses.

**References**: 1. Zhou J, et al. Nat Med. 2003;9(8):1085-90. 2. Ward K, et al. J Magn Reson. 2000;143(1):79-87. 3. Zhou J, et al. J Magn Reson Imaging. 2013;38(5):1119-28. 4. Jia G, et al. J Magn Reson Imaging. 2011;33(3):647-54. 5. Sun PZ, et al. J Cereb Blood Flow Metab. 2007;27(6):1129-36. 6. Sodickson DK, et al. Magn Reson Med. 1997;38(4):591-603. 7. Pruessmann KP, et al. Magn Reson Med. 1999;42(5):952-62. 8. Griswold MA, et al. Magn Reson Med. 2002;47(6):1202-10. 9. Zhu H, et al. Magn Reson Med. 2010;64(3):638-44. 10. Zhang Y, et al. Magn Reson Med. 2016. doi: 10.1002/mrm.26307.

## Clinical APTw MRI at 3T: Technique Review and Recommendations

Jinyuan Zhou

*Division of MR Research, Department of Radiology, Johns Hopkins University, Baltimore, Maryland, USA*
*F.M. Kirby Research Center for Functional Brain Imaging, Kennedy Krieger Institute, Baltimore, Maryland, USA*

Amide proton transfer-weighted (APTw) imaging is a novel molecular MRI technique that generates image contrast based predominantly on the amide protons in mobile cellular proteins and peptides that are endogenous in tissue. The technique, a specific type of chemical exchange saturation transfer imaging, has successfully been used for imaging of protein content and pH, the latter being possible due to the strong dependence of the amide proton exchange rate on pH. APTw MRI is showing promise especially for characterizing brain tumors and distinguishing recurrent tumor from treatment effects.

Even though promising, there are several challenging issues for clinical APT-based imaging. These issues include scanner RF amplifier constraints, SAR requirements, long scan time, complicated contrast mechanism with multiple contributions, data interpretation depending on the APTw pulse sequences and parameters used, and the possibility of $B_0$ inhomogeneity artifacts and lipid artifacts. In addition, differences in data processing strategies may complicate the reproducibility and comparison of results between hospitals.

For APTw imaging on animal systems, RF saturation is typically applied using a CW block pulse of several seconds to maximize effects. However, clinical MRI systems generally have limited amplifier duty-cycles and saturation pulse lengths, especially due to the use of large body coils for transmit.[1-8] This has been addressed by three different methods: pulse-train pre-saturation,[3-8] pulsed steady-state,[9] or time-interleaved parallel RF transmission (pTX).[10]

Clinical application of the APTw MRI approach will be more feasible if fast volumetric imaging, either multi-slice or three-dimensional (3D), can be achieved. Of these, 3D acquisition is preferred so that differences in saturation losses caused by $T_{1w}$ relaxation between slices can be minimized.[3] Recently, several methods have been developed to accelerate CEST/APT acquisitions, including various conventional fast imaging techniques and reduced k-space acquisition techniques (including keyhole[11] and compressed sensing[12]) that require more advanced data processing.

Due to a lack of agreed upon standards between the research community and manufacturers, current APTw and other CEST imaging protocols vary substantially among different institutes, far from being optimized, and the results acquired from different research centers are often difficult to compare to one another. Currently, our recommended RF power for APTw imaging of brain tumors is about 2 μT with a total RF saturation time of about 0.8-2 sec (possibly with inter-pulse delays) to generate a homogeneous background signal for normal brain tissue.[13] Without this, the proper APTw contrast may not be obtained, and results may vary strongly with respect to published literature.

The APTw imaging sequence is now becoming available commercially on some 3T clinical MRI scanners. Thus, more medical centers will soon be able to utilize the technique in daily clinical practice and to explore new applications on all fronts. The ultimate goal for APT-based imaging is reproducible clinical use on a variety of MRI systems from different vendors. Thus, there is an urgent need for industry and academia to work together to develop this emerging technology into a clinically viable, easy-to-use, optimized, and standardized approach.

This work was supported in part by grants from the NIH (R01EB009731, R01EB015032, R01CA166171, and P41EB015909).

1. Dixon, W.T.*, et al. Magn. Reson. Med.* **63**, 253-256 (2009).
2. Scheidegger, R., et al. *NeuroImage* **99**, 256-268 (2014).
3. Zhu, H., et al. *Magn. Reson. Med.* **64**, 638-644 (2010).
4. Dula, A.N.*, et al. Magn. Reson. Med.* **70**, 216-224 (2013).
5. Mehrabian, H., et al. *Clin. Cancer Res.* **23**, 3667-3675 (2017).
6. Sun, P.Z., et al. *Magn. Reson. Med.* **60**, 834-841 (2008).
7. Schmitt, B., et al. *Magn. Reson. Med.* **65**, 1620-1629 (2011).
8. Tee, Y.K.*, et al. NMR Biomed.* **27**, 1019-1029 (2014).
9. Jones, C.K.*, et al. Magn. Reson. Med.* **67**, 1579-1589 (2012).
10. Keupp, J., et al. in *Proc. 19th Annual Meeting ISMRM* 710 (2011).
11. Varma, G., et al. *Magn. Reson. Med.* **68**, 1228-1233 (2012).
12. Heo, H.Y.*, et al. Magn. Reson. Med.* **77**, 779-786 (2017).
13. Zhou, J.*, et al. J. Magn. Reson. Imaging* **38**, 1119-1128 (2013).

**Addressing the unmet needs of non-ischemic heart disease patients using cardiac CEST as an all-in-one tool**

Moriel Vandsburger[1]
[1]*Department of Bioengineering, U.C. Berkeley, Berkeley, CA, USA*

CEST-MRI is rapidly emerging as a molecular MRI tool with broad application to stationary organs and tumors, but with limited application in the heart. Many CEST approaches ranging from imaging of endogenous metabolites such as creatine, to tracking the expression patterns of genetically encoded CEST reporter genes are directly applicable to unmet needs in cardiovascular imaging, particularly in the setting of non-ischemic cardiomyopathy. However, rapid and variable cardiac motion and respiratory intervals that are inconsistent across species mean that conventional CEST-MRI approaches can not be easily used. In addition, important concerns including B1/B0 inhomogeneity can lead to false contrasts. With changes to pulse sequence design, and with analysis that accounts for signal evolution during the cardiac cycle, cardiac CEST approaches can be developed to address unmet needs in cardiology. The goals of this presentation are to discuss existing approaches for cardiac CEST MRI and to highlight early applications in both pre-clinical and clinical settings for multi-scale cardiac imaging. Finally, potential applications and remaining challenges will be discussed as a framework for the development of cardiac CEST as a comprehensive tool for unlocking the complex changes in the setting of heart disease.

**Acknowledgements:** NIH 1R01HL28592, NIH P20GM103527-07sub5039, Slomo and Cindy Sylvian Foundation

# CEST imaging of liver and lumbar intervertebral disc: looking into the future

Yi-Xiang Wang

The Chinese University of Hong Kong, Shatin, N.T. Hong Kong SAR, China

Chemical exchange saturation transfer (CEST)-MRI exploits a specific MR frequency (chemical shift) of molecules while generating images with good spatial resolution, therefore combines the specificity of MR spectroscopy with the spatial resolution of imaging and offers great potential for *in vivo* biochemical composition characterization of tissues. The clinical value of CEST-MRI for brain tumors have been recognized and utilized. The feasibility of in vivo CEST-MRI for liver [1, 2] and lumbar intervertebral disc [3-7] in human subjects has been reported. It can be hypothesized that CEST-MRI can detect early stage liver fibrosis and differentiate liver simple steatosis vs. steatohepatitis, and diagnose back pains of discogenic origin, these are issues of great clinical importance but currently there is not established non-invasive diagnostics available. While it has been demonstrated that CEST-MRI is highly sensitive to liver tissue composition changes [1,2], for clinical liver imaging CEST-MRI is currently limited by its long scan time and liver's susceptibility to respiration motion, its rescan-rescan reproducibility remain unsatisfactory. Techniques for fast CEST-MRI and motion corrections are essential for translating liver CEST-MRI to clinical application. Intervertebral disc is not susceptible to physiological motion, thus long scan time would be less of an issue. However, the diagnostic value of CEST-MRI still remains to be demonstrated. While most CEST-MRI validated known phenomena such as age associated disc degeneration, there is no systematic study looked at CEST-MRI readouts' association with pathophysiological mechanism of discogenic pain. Recent small cohort reports suggested that patients with low back pain (LBP) had lower CEST effect than subjects without LBP [8, 9], however, the conclusion should be interpreted with great caution, as the association with disc degeneration and LBP is poor and majority of LBP are probably associated with lumbar strain/sprain rather than being discogenic [10]. Additionally, group-wise statistical difference does not necessarily suggest satisfaction diagnostic performance with the latter being much more demanding. To demonstrate the ability of identifying discogenic pain would be vital for CEST-MRI's clinical utilization for disc imaging. It has been noted that changes in posterior annulus fibrosus are probably more associated with LBP [11]. Notably, the inner annulus fibrosus, which shows bright signal on T2 weighted imaging, has been incorrectly regarded as part of nucleus pulposus in many publications [12]. Comparative studies of CEST-MRI with faster techniques such as T1rho imaging will be of interests and are still being awaited [7].

References

[1].Deng M, et al. *Mol Imaging Biol*. 2016;18:274-82. [2].Chen SZ, et al. *Eur Radiol.* 2016;26 :1792-800 [3].Kim M, et al. *NMR Biomed.* 2011;24:1137-44. [4].Müller-Lutz A, et al. *Magn Reson Imaging.* 2016;34:271-5. [5].Müller-Lutz A, et al. *J Magn Reson Imaging.* 2015;42:1517-23. [6].Schleich C, et al. *Spine* 2016;41:146-52. [7].Deng M, et al. *Biomed Environ Sci.* 2016;29:47-55. [8].Wada T, et al. J *Magn Reson Imaging.* 2017;45:863-871. [9].Liu Q, et al. *Magn Reson Med.* 2015;73:1196-205. [10].Wang YX, et al. *J Orthop Translat.* 2018;15:21-34. [11].Ogon I, et al *J Orthop Sci* 2015;20:295-301. [12].Mok GS, et al. *J Orthop Translat* 2016;6:34-41.

**Using pH and perfusion imaging to detect progression in renal disease**

KowsalyaDevi Pavuluri[1], Irini Manoli[2], Alexandra Pass[2], Irene Ginty[2], Darwin Romero[2], Charles P. Venditti[2], and Michael T McMahon[1,3*]

[1]The Russell H. Morgan Department of Radiology and Radiological Science, Division of MR Research, The Johns Hopkins University School of Medicine, Baltimore, MD, USA; [2]Center Genetics and Molecular Biology Branch, National Human Genome Research Institute, National Institutes of Health (NIH), Bethesda, MD, USA; [3]F.M. Kirby Research Center for Functional Brain Imaging, Kennedy Krieger Institute, Baltimore, MD, USA

**INTRODUCTION:** "Methylmalonic acidemia (MMA) is an organic acidemia characterized by defects in the metabolism of methylmalonic acid. This creates an inability to digest certain fats and proteins, and leads to a toxic buildup of methylmalonic acid which produces a predictable evolution to chronic kidney disease (CKD). Unfortunately, current diagnostics for MMA patients such as blood tests of creatine, blood nitrogen urea and serum albumin leave much to be desired. Measurement of GFR is an additional screening tool, however GFR is difficult to routinely measure on children and doesn't provide a complete picture of kidney health. We are exploring administration of pH sensitive MRI contrast agents as a new diagnostic. In this study, we evaluate iopamidol as a CEST pH sensorto determine iopamidol renal perfusion and create concentration independent pH maps. To accomplish this, we developed a CEST MRI protocol to detect changes in filtration fraction (FF) and pH.

**METHODS:** Experiments were performed on male C57BL/6 mice with altered expression of methylmalonyl-CoA-mutase (Mut)$^{-/-}$ under control of the albumin promoter (Mut$^{-/-}$; Tg$^{INS\text{-}Alb\text{-}Mut}$ and a control Mut$^{+/-}$. The mice were further subdivided by placing half on a regular diet (RD) and on a high protein diet (HP). Iopamidol was injected through the tail vein and CEST images acquired using a CEST-RARE pulse sequence. 2 saturation offsets (4.2, 5.5 ppm) and $M_0$ images were collected. The FF was calculated by determining the percentage of pixels in the kidneys with contrast > 20% of maximum contrast. Furthermore, the ST ratio for offsets 4.2 and 5.5 ppm was calculated using $R_{ST} = \frac{\left(100 - ST_{4.2\ ppm}\right).ST_{5.5\ ppm}}{\left(100 - ST_{5.5\ ppm}\right).ST_{4.2\ ppm}}$ where $ST = 1 - \frac{M_z}{M_0}$ and used to prepare pH maps.

**RESULTS:** The FF was found to be significantly different between the groups of mice (**Fig.1**) with this metric comparable for all +/- control animals. FF was vastly different for the two -/- groups and reduced to as low as 19% in the -/- HP mice which had the worst kidney function. The decrease in FF was also associated with animal weight, a secondary indicator of health. Decrease in pH was in accordance with the decrease in weight of the mice with the progress of disease. pH was distributed over a narrow range of 6.50±0.02 for RD and HP *(+/-)* mice. The range of pH distribution was observed to increase with the severity of the disease. The pH distribution ranges of RD *(-/-)* mice was ~ ±0.15 pH units, whereas this range was further increased to ~ ± 0.30 pH units along with a decrease in pH for HP *(-/-)* mice.

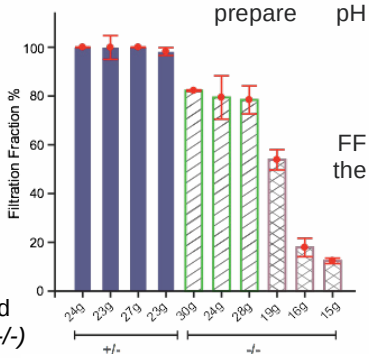



**Fig.1:** Filtration fraction The decrease in FF was in accordance with a decrease in weight of the mice which is a secondary indicator of disease

**DISCUSSION:** We have successfully developed a CEST MRI protocol based on administration of iopamidol and using a 2 frequency acquisition scheme to characterize the perfusion and pH changes observed in mice with differences in renal function. The MRI results showed that, compared to healthy controls, the FF displayed an ~20% reduction for moderate renal disease mice and an over 50% reduction in severe renal disease mice. This metric was more sensitive than pH mapping, with the range in pH values more sensitive to differences in renal function more than average pH.

**CONCLUSION:** CEST MRI using iopamidol displays promise as a diagnostic for detecting progression towards CKD progression in a mouse model.

**ACKNOWLEDGMENTS:** This project was supported by the Maryland Stem Cell Research Foundation MSCRF#2829

## Functional renal imaging with MRI-CEST

Dario Livio Longo[1]

[1]*Molecular Imaging Center, Department of Molecular Biotechnology and Health Sciences, University of Torino, Via Nizza 52, Torino, ITALY*

Several functional parameters can be non-invasively assessed by using MRI approaches for the evaluation of renal physiology and function in kidney diseases [1]. An important parameter is renal perfusion that can be measured throughout the acquisition of dynamic contrast-enhanced images (DCE-MRI) upon the injection of a Gd-based contrast agent (CA) by following its transit through the kidney region [2]. Furthermore, iopamidol, a MRI-CEST pH-responsive contrast agent has also been shown to be able to report on renal pH values [3] and to assess the longitudinal evolution of renal pH homeostasis and renal filtration in murine models of kidney ischemia reperfusion injury and of acute tubular necrosis [4,5].

However, methods able to provide multiple information following a single CA injection would be of great interest for an improved and multiparametric characterization of renal functionality. We will present a dynamic CEST acquisition for the simultaneous assessment of renal perfusion and pH by using iopamidol. A simple procedure for the semiquantitative determination of renal perfusion, coupled to functional pH mapping, using a single pH-responsive CEST tracer, has been set up and applied for the assessment of renal function in mice exposed to unilateral ischemia-reperfusion injury (Acute Kidney Injury, AKI). The capability of this combined approach to report on kidney damage has been validated and compared with the DCE-MRI assessment of renal perfusion following Gd-based agent injection in the same mice.

In addition, renal pH mapping can be exploited to assess renal functionality following sepsi-induced damage. Sepsis is a state of systemic inflammation to a suspected infection that leads to multiorgans failure, including acute kidney injury, with dramatic clinical outcomes [6]. We will show how pH-CEST mapping can detect organ dysfunctional changes by significantly measuring increased extracellular pH values upon LPS administration in the whole kidney section and in both renal compartments (cortex and medulla).

Overall these studies show that a single MRI-CEST contrast agent can provide multiple information related to renal function and can discern healthy kidneys from pathological ones combining perfusion measurements with renal pH mapping.

**ACKNOWLEDGMENTS:** Support from Compagnia San Paolo project (Regione Piemonte, grant #CSTO165925), European Union's Horizon 2020 research and innovation programme under grant agreement No 667510 (GLINT project) and EU COST action PARENCHIMA (CA16103).

**REFERENCES:**

[1] N. Grenier, et al., Eur J Radiol. 2006
[2] F. G. Zollner, et al., Z Med Phys, 2014
[3] D. L. Longo, et al, Mag Reson Med 2011
[4] D. L. Longo, et al., Mag Reson Med, 2013
[5] D. L. Longo, et al., NMR Biomed, 2017
[6] Zarjou et al., J am Soc Nephrol 2011

**Recent advances in the study of non-invasive MR pH imaging using chemical exchange saturation transfer**

Renhua Wu

*Department of Medical Imaging, Shantou University Medical College, Shantou, P.R. China*

Alteration in tissue pH is an indicator of many pathological processes. Noninvasive MR pH imaging will be much helpful for disorder characterization and therapy, even monitoring cell viability. Noninvasive brain pH measurements have routinely relied on $^{31}$P magnetic resonance spectroscopy techniques which require additional hardware, take too long to be clinically useful, and provide very limited spatial resolution. Chemical exchange saturation transfer (CEST) is a versatile technique for MR molecular imaging, which has widely be used for non-invasive pH imaging and low-concentration biomolecule detection. For example, the potential of amide proton transfer (APT) had been proved for imaging pH effects in ischemic rat brain noninvasively [1].

A lot of important studies of non-invasive MR pH imaging using CEST have been published by different labs in recent years. With combination of amide and guanidyl CEST, the sensitivity of pH-weighted MR imaging can be enhanced for ischemic rat brain in a recent study [2]. Iopamidol, as a chemical exchange-dependent saturation transfer contrast medium, has been used to measure extracellular pH (pHe) [3]. A single dose of cariporide can induce a rapid change of intracellular pH (pHi) in animal glioblastoma multiforme, which is observed by using amine/amide concentration-independent detection (AACID) CEST MR imaging [4]. It was also found that the major contributors to in vivo $T_1$ -normalized $MTR_{asym}$(3.5 ppm) contrast between white and gray matter in normal brain are pH-insensitive macromolecular magnetization transfer (MT) and nuclear Overhauser enhancement. The pH-sensitive amine and amide effects account for nearly 60% and 80% of the $MTR_{asym}$ changes seen in white and gray matter, respectively, after global ischemia, indicating that $MTR_{asym}$ is predominantly pH-sensitive [5]. Clinical translation of pH-weighted MR imaging has been conducted for diagnosing human brain tumors [6].

In our most recent studies, *in vivo* gas challenge in an experimental glioma model in rats showed that enhanced pH-weighted MR imaging can more effectively localize tumor periphery. In addition, ioversol (a clinical CT contrast medium) CEST MR imaging can be exploited to achieve pHe mapping of human liver cancer microenvironment.

References

[1] Zhou J, et al. Nat Med. 2003; 9:1085-90.
[2] Jin T, et al. Neuroimage. 2017; 157:341-350.
[3] Sun PZ, et al. Phys Med Biol. 2014; 59:4493-504.
[4] Albatany M, et al. Int J Clin Oncol. 2018. doi: 10.1007/s10147-018-1289-0.
[5] Zhou IY, et al. Magn Reson Med. 2018. doi: 10.1002/mrm.27385.
[6] Shen Y, et al. NMR Biomed. 2017; 30(9). doi: 10.1002/nbm.3735.

## Furin-Mediated Intracellular Self-Assembly of Olsalazine Nanoparticles Enhances MR Imaging and Tumor Therapy

Yue Yuan[1], Jia Zhang[1], Xiaoliang Qi[1], Shuoguo Li[2], Guanshu Liu[1,3], Xiaolei Song[1], Michael T. McMahon[1,3], and Jeff W.M. Bulte[1,3]

*[1]The Russell H. Morgan Department of Radiology and Radiological Science, Division of MR Research, The Johns Hopkins University School of Medicine, Baltimore, MD; [2]Center for Biological Imaging, Institute of Biophysics, Chinese Academy of Sciences, Beijing, PR China; [3]F.M. Kirby Research Center for Functional Brain Imaging, Kennedy Krieger Institute, Baltimore, MD, United States*

INTRODUCTION: A strategy to enhance tumor retention of imaging agents or anti-cancer drugs is rational design of probes that undergo a tumor-specific enzymatic reaction which prevents them from being pumped out of the cell. Cell-specific intracellular nanoparticles can be expected to increase the overall intracellular concentration of CEST contrast agents, increasing sensitivity while minimizing non-target toxicity. The potential benefits of intracellular assembly prompted us to develop an enzyme-responsive theranostic platform for tumor imaging and therapy.

METHODS: The cancer clinical prodrug olsalazine (Olsa) was conjugated to the cell-penetrating peptide RVRR. Taking advantage of a biologically compatible condensation reaction, single Olsa-RVRR molecules were self-assembled into large intracellular nanoparticles (Olsa-NP) by the tumor-associated enzyme furin (**Fig. 1**). Nude mice were s.c. injected with $1\times10^6$ HCT116 (furin-overexpressing) or $1\times10^6$ LoVo (low furin-expressing) human colon carcinoma tumor cells. *In vivo* CEST MRI was performed at different time points following i.v. injection of substrates using a 11.7 T Bruker horizontal scanner. Animals were randomly divided into three groups (n=4 for each group), and 0.1 mmol/kg Olsa-RVRR, 0.1 mmol/kg Olsa, or PBS only (as control) was injected 8 times with 3-day intervals.

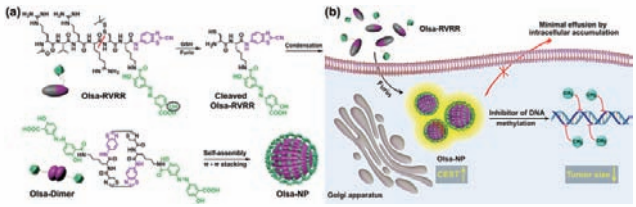



**Figure 1:** (a) Chemical and (b) biological scheme for the formation of Olsa-NP by furin-mediated intracellular reduction and condensation of Olsa-RVRR.

RESULTS: Both Olsa-RVRR and Olsa-NP could be readily detected with chemical exchange saturation transfer magnetic resonance imaging (CEST MRI) by virtue of exchangeable Olsa hydroxyl protons. *In vivo* studies using HCT116 and LoVo murine xenografts showed that the OlsaCEST signal and anti-tumor therapeutic effect were 6.5-fold and 5.2-fold increased, respectively, compared to Olsa without RVRR modification, with an excellent "theranostic correlation" ($R^2$ =0.97) between the magnitude of the imaging signal and therapeutic response (normalized tumor size) (**Fig. 2**).

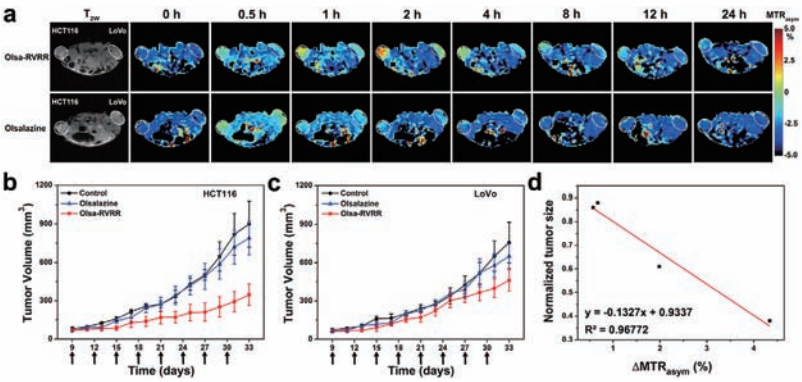



**Figure 2:** (**a**) Dynamic T2-weighted and OlsaCEST serial MRI of tumor-bearing mice after i.v. injection of 0.2 mmol/kg Olsa-RVRR or olsalazine (left: HCT116; right: LoVo). (**b, c**) Anti-tumor effects of olsalazine and Olsa-RVRR for HCT116 (**b**) and LoVo (**c**) tumors. Arrows indicate time points of repeated drug administration (QD3x8) after tumor cell injection. Data are shown as mean±SD (n=4 each group). (**d**) Theranostic correlation between tumor OlsaCEST signal at 2h and normalized tumor size at day 33.

CONCLUSION: This new furin-targeted theranostic platform has potential for imaging tumor aggressiveness, drug accumulation, and therapeutic response. Since olsalazine has been approved by the FDA in 1990 for treatment of inflammatory bowel disease, our approach may be clinically readily translatable.

**Clinical CEST MRI studies at Ultra-high B0 field (7T and 9.4T)**

Moritz Zaiss[1]

[1]*Magnetic resonance center, Max-Planck institute for biological cybernetics, Tübingen, Germany*

**INTRODUCTION:**

CEST benefits of ultra-high fields due to the better frequency separation(1,2). However, is this just a benefit for the interested MR scientist or is this also of use to address clinical questions? This can only be answered if CEST measurements of humans are performed at 7T or even 9.4T both available for human scans. While judgment about clinical benefits require larger studies, CEST in humans at UHF brings interesting preliminary insights and strong hypothesis generation.

**METHODS:** 3D low power snapshot-CEST(3) at 3T, 7 T and 9.4 T scanners (Siemens Healthcare) were acquired in healthy volunteers and brain tumor patients (after informed written consent). Post-Processing included B0, B1 and motion correction, and subsequent Lorentzian line fit analysis.

**RESULTS & DISCUSSION:**

Correction steps are very important at UHF due to larger field inhomogeneities. Spectral resolution clearly improves going from 3 T to 7T and 9.4T (Figure 1). Additional peaks can be found and interesting behavior in tumor areas is observed. Most interesting at 7T is until now the downfield-NOE suppressed amide signal, that very nicely correlates with Gadolinium uptake areas and might show extra cellular proteins. At 9.4T additional peaks at 2 ppm, 2.7 ppm and -1.6 ppm could be detected and created novel imaging contrasts (Figure 2). In addition, several unassigned spectral features were observed in spectra of tumor ROIs. Clinically several interesting features could be evaluated so far: such as survival prediction, identification of early progression (4), or characterization of mutations (5) making isolated CEST MRI at UHF a generator of novel non-invasive MR biomarkers. Translation of UHF prior-knowledge to clinical field strength is possible using the neural network approach deepCEST (data not shown).

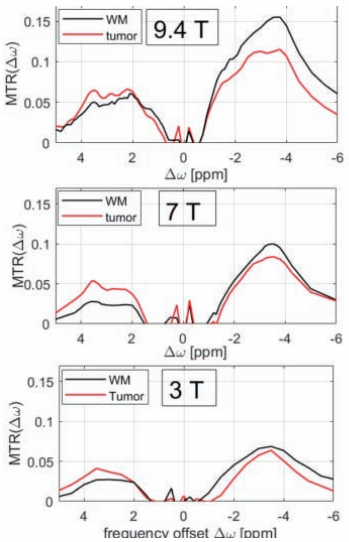



*Figure 1: Low power Z-spectra in human brain WM and tumor at 9.4T, 7T and 3T.*

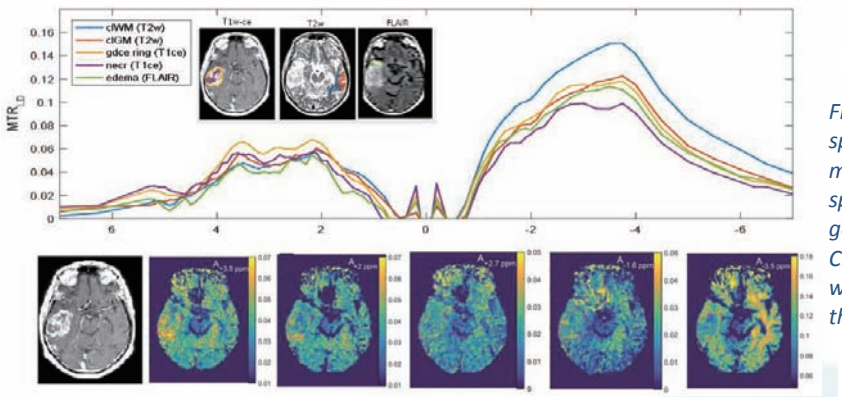



*Figure 2: ROI-averaged MTR-spectra of a tumor patient measured at 9.4T. High spectral selectivity allows generation of several new CEST contrasts (bottom row) with different correlations in the tumor area.*

**CONCLUSION:** Clinical CEST studies at UHF yield new insights in the Z-spectrum and helps generating hypotheses. Separation of many effects allow more flexible combination to create novel biomarkers. Novel machine learning techniques are able to translate this information to 3T.

**ACKNOWLEDGMENTS:** MPG, DFG Grant No. ZA 814/2-1, EU Horizon 2020 Grant No. 667510

**REFERENCES:**

(1) van Zijl et al. Neuroimage 2017,DOI10.1016/j.neuroimage.2017.04.045.
(2) Zaiss and Bachert. Physics in medicine and biology 2013;58:R221–R269.
(3) Zaiss M et al., NMR Biomed 2018;31:e3879.
(4) Regnery S et al, Oncotarget 2018;9:28772–28783.
(5) Paech D et al., Neuro-Oncology 2018;Epub ahead,DOI10.1093/neuonc/noy073.

## Rapid and Quantitative CEST Imaging with Magnetic Resonance Fingerprinting

*Or Perlman[1], Ouri Cohen[1], Inge Mulder[2], Cenk Ayata[2], Taylor Kimberly[2], Matthew S. Rosen[1], Christian T. Farrar[1]*

*[1]Athinoula A. Martinos Center for Biomedical Imaging, Department of Radiology, and [2]Department of Neurology, Massachusetts General Hospital and Harvard Medical School, Charlestown, MA, USA*

**INTRODUCTION:** While Chemical Exchange Saturation Transfer (CEST) MRI has proven to be a powerful tool for imaging a wide range of disease pathologies, clinical translation of CEST-MRI has been hindered by the qualitative nature of the image contrast, the long image acquisition times, and the complex data processing required. Here we build on the recently developed Magnetic Resonance Fingerprinting (MRF) (1) and deep learning neural network (NN) MRF parameter map reconstruction (2) techniques and report the use of a fast CEST fingerprinting method for generating quantitative T1, T2, and amide and semi-solid proton chemical exchange rate and concentration maps of normal and stroke rat models.

**METHODS:** CEST-MRF Echo Planar images were acquired on a 4.7 T MRI scanner as described previously (3) using an acquisition schedule that either varied only the saturation power or that varied the saturation power, time, and frequency offset as well as the repetition time (TR) and the excitation pulse flip angle (FA). Reconstruction of the tissue parameter maps was performed with either dictionary matching or Deep Learning Reconstruction neural network (DRONE) approaches. For dictionary-based reconstruction, a 6.5 million entry dictionary with different combinations of water T1 and T2 and amide and semi-solid proton exchange parameters was simulated. For the Deep Learning parameter reconstruction, a 4-layer, fully connected neural network (NN) was used. The NN was defined using the TensorFlow framework and consisted of a 30 node input layer, two 300 node hidden layers and a 6 node output layer (2). Training of the NN was performed with a sparse MRF dictionary with 1 million entries. The different methods were tested in a rat stroke model consisting of 2-hour middle cerebral artery occlusion (MCAO) followed by reperfusion. Rats were imaged 48-hours post reperfusion.

**RESULTS AND DISCUSSION:** Recently, we and others have demonstrated a rapid MR Fingerprinting (MRF) based CEST technique that enables accurate quantification of proton exchange rates and volume fraction maps in a fraction of the time required by conventional pulse sequences (3,4). The exchange rates and volume fractions obtained were validated in phantoms and in comparison to literature values in a healthy rat brain. However, the *in vivo* studies matched only the amide and semi-solid proton pool exchange parameters and kept the water T1 and T2 fixed. In disease pathologies the chemical exchange and water T1 and T2 relaxation parameters will all vary and need to be included in the matching dictionary. However, matching of highly multi-parametric data is quite challenging and the accuracy of the parameter maps is limited by the resolution of the dictionary. This is demonstrated in Figure 1 where very poor exchange and relaxation parameter map reconstructions are observed for dictionary matching of a MCAO-reperfusion rat stroke model. Improved exchange parameter maps are obtained with the DRONE neural network, but poor T1 and T2 accuracy is still observed due to the fixed TR and FA used in the saturation power acquisition schedule. Improved T1 and T2 accuracy can be achieved by varying the TR and FA. For the saturation/TR/FA acquisition schedule, good agreement was observed between T1 and T2 maps generated by CEST-MRF and by T1 saturation recovery and T2 multi-echo spin-echo methods, respectively. Further optimization of the CEST-MRF acquisition schedule is underway and should provide further improvements in the accuracy of the reconstructed tissue parameter maps.

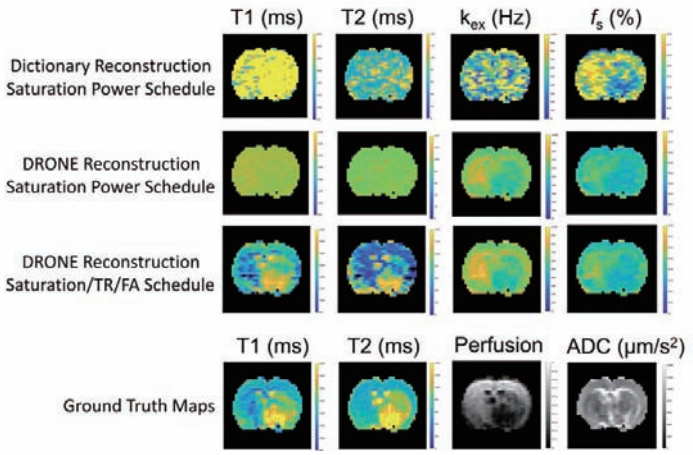



***Figure 1:*** *Water T1 and T2 relaxation and amide proton chemical exchange rate and volume fraction maps reconstructed using either dictionary matching or a DRONE neural network along with the ground truth T1 and T2 maps generated from saturation recovery and multi-echo spin-echo sequences, respectively.*

**CONCLUSION:** Deep CEST-MRF provides a method for fast, quantitative CEST imaging. The deep learning NN allows for rapid reconstruction of multiple parameter maps with continuous instead of discrete parameter map values thereby improving the accuracy and efficiency.

**REFERENCES:**

1. Ma D, Gulani V, Seiberlich N, Liu K, Sunshine JL, Duerk JL, et al. Nature. 2013 Mar 14;495(7440):187–92.
2. Cohen O, Zhu B, Rosen MS. Magn Reson Med. 2018 Sep;80(3):885–94.
3. Cohen O, Huang S, McMahon MT, Rosen MS, Farrar CT. Magn Reson Med. 2018 May 13.
4. Zhou Z, Han P, Zhou B, Christodoulou AG, Shaw JL, Deng Z, et al. Magn Reson Med. 2018 May 30.

**Chemical Exchange Saturation Transfer MR Fingerprinting by Subgrouping Proton Exchange Models**

Hye-Young Heo

*Division of MR Research, Department of Radiology, Johns Hopkins University, Baltimore, Maryland, USA*

**INTRODUCTION:** Current chemical exchange saturation transfer (CEST) neuroimaging protocols typically acquire CEST-weighted images, and, as such, do not essentially provide quantitative proton-specific exchange rates and concentrations. Finding a unique (or sparse) solution (CEST parameters) in an ill-posed inverse problem is always challenging, particularly when multiple components for CEST MRI are considered. To overcome this issue, we shrank the exchange model and reduced fitting parameters by subgrouping proton exchange models. Additional information/constraints, such as different RF saturation powers, saturation times, and frequency offsets were added to find a unique solution (1, 2). Here, we developed a novel MR fingerprinting (MRF) technique to allow CEST parameter quantification with a reduced data set. This was accomplished by subgrouping proton exchange models (SPEM), taking amide proton transfer (APT) as an example, into two-pool (water and semisolid macromolecules) and three-pool (water, semisolid macromolecules, and amide protons) models. A pseudo-randomized RF saturation scheme was used to generate unique signal evolutions for different tissues, reflecting their CEST parameters.

**METHODS:** In the MRF-SPEM framework, RF saturation frequency offset, power, duration, and TR were varied in a pseudorandom fashion throughout the saturation and acquisition. CEST-SPEM images consisted of two distinct datasets: (i) two-pool MTC data with far off-resonance frequency offsets between 10 ppm and 50 ppm to avoid possible downfield CEST signal contributions; and (ii) three-pool APT data with saturation frequency offsets between 3 ppm and 4 ppm. The two-pool parameters were incorporated into the three-pool model as prior known information, reducing the number of parameters and fitting uncertainty errors. The proposed CEST-SPEM was first tested on Bloch equation-based digital phantoms with appropriate SNR levels mimicking APT experiments and ammonium chloride phantoms. For in-vivo studies, five healthy volunteers were scanned on a Philips 3T MRI scanner after informed consent was obtained in accordance with the IRB requirement. To compare the proposed MRF-SPEM with conventional CEST measurements as a standard for validation of in-vivo CEST parameter quantification, Z-spectra were synthesized using estimated parameters from MRF-SPEM and compared with experimentally measured Z-spectra with three different RF saturation powers (1, 1.5, and 2 μT).

**RESULTS&DISCUSSION:** Numerical phantom studies demonstrated that MRF-SPEM can enable a high degree of accuracy and precision in absolute CEST quantification at 3T magnetic field strength. In addition, we compared MRF-SPEM with a conventional Bloch equation fitting method with high-resolution Z-spectra using ammonium chloride-agarose phantoms and observed great agreement between the two measurements for the proton quantification. For human studies, using CEST parameters estimated from MRF-SPEM, synthetic Z-spectra were reconstructed with saturation/imaging parameters identical to those used in the standard scan (**Fig. 1**). Synthesized and experimentally measured signals were in excellent agreement at positive frequency offsets. The semisolid macromolecular proton exchange rates for gray and white matter were ~40 Hz and ~29 Hz, respectively, and the concentrations of ~6 M and ~11 M, respectively, were in good agreement with previous observations (3-5). The amide proton concentration in gray matter (~265 mM) was somewhat higher than that of the white matter (~212 mM). In addition, the amide proton exchange rate (~365 Hz) of gray matter was significantly faster than that of white matter (~162 Hz). A previous human study at 7T (6) measured the amide proton exchange rate of ~280 Hz, which is comparable to that measured here. A human study using the frequency labeled exchange approach measured a rate on the order of 350-400 Hz (7). Another human study (8) measured the amide proton concentration of 220 mM, which is consistent with that measured in this work.

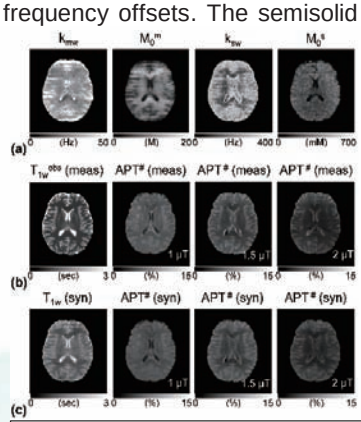



**Fig. 1** (a) MTC (*m*) and APT (*s*) parameter maps obtained from MRF-SPEM. (b) experimentally measured $T_1$ map and APT$^{\#}$ images (9). (c) Synthetic $T_1$ map and APT$^{\#}$ images.

**CONCLUSION:** We have developed a quantitative CEST-SPEM technique under the assumption of a single CEST pool at a certain frequency. The present CEST-SPEM scan took just 2 min 50 sec (including $B_0$ and $B_1$) to obtain apparent APT exchange rate and concentration maps, which may be applicable to many clinical applications. Furthermore, this quantitative approach could provide some insight into the origin of the APTw image contrast in malignant gliomas showing abundant intracellular mobile proteins and a reversed pH gradient between alkaline intracellular and acidic extracellular compartments.

**REFERENCES:** (1) Zhou Z, *et al*. Magn. Reson. Med 2018;80:1352-1363. (2) Cohen O, *et al*. Magn. Reson. Med 2018;doi/10.1002/mrm.27221.(3) Sled J and Pike G, Magn. Reson. Med 2001;46:923-931. (4) Stanisz G, *et al*. Magn. Reson. Med 2005;54:507-512. (5) Mougin O, *et al*. Neuroimage 2010;49:272-281. (6) Liu D, *et al*. Magn. Reson. Med 2013;70:1070-1081. (7) Yadav N, *et al*. Magn. Reson. Med 2013;69:966-973. (8) Geades N, *et al*. Magn. Reson. Med 2017;78:645-655. (9) Heo H-Y, et al. Magn. Reson. Med 2016;75:137-149.

## Quantitative tissue pH MRI in an experimental model of acute ischemic stroke

Enfeng Wang[1], Yin Wu[1], Jerry S Cheung[1], Takahiro Igarashi[1], Limin Wu[2], Phillip Zhe Sun[1,3,4]

*[1]Martinos Center for Biomedical Imaging, MGH and HMS. [2]Neuroscience Center and Department of Pediatrics, MGH and HMS. [3]Department of Radiology, Emory Univ. [4]Yerkes National Primate Research Center, Emory Univ.*

**INTRODUCTION:** Amide proton transfer (APT) MRI is sensitive to tissue pH change during acute ischemia, yet the commonly used pH-weighted magnetization transfer (MT) ratio asymmetry ($MTR_{asym}$) analysis is of limited pH specificity. To overcome this, MT and relaxation normalized APT (MRAPT) analysis has been developed that provides highly pH specific measurement[1]. Our study aimed to calibrate MRAPT MRI toward absolute tissue pH mapping and determine regional pH changes during acute stroke.

**METHODS:** The study has been approved by the local IACUC. Rats were imaged using a 4.7T MRI scanner with multi-slice EPI. We collected water-suppressed single voxel point resolved spectroscopy (PRESS), relaxation, diffusion, APT and perfusion MRI. Fifteen acute stroke rats underwent multi-parametric MRI and lactate MRS for pH calibration. Two rats were excluded due to failed stroke surgery. Another group of twenty acute stroke rats underwent multi-parametric MRI (without lactate MRS).

**RESULTS:** We calibrated $MTR_{asym}$ and ΔMRAPTR indices toward tissue pH (Fig. 1). Specifically, pH was derived from the lactate content according to pH=-0.0335*[Lac]+6.83 [2, 3]. $MTR_{asym}$ and ΔMRAPTR were numerically fit with respect to pH. For $MTR_{asym}$, we had $pH=\log10((100*MTR_{asym}-C_2)/C_0)/C_1$, with $C_0$, $C_1$ and $C_2$ being 0.46, 0.19 and -13.9 ($R^2$=0.45, P<0.05). For ΔMRAPTR, we had $pH=7.05+\log10(\Delta MRAPTR/ C'_0+1)/C_1$, with $C'_0$ and $C_1$ being 5.04 and 0.25, respectively ($R^2$=0.70, P<0.001).

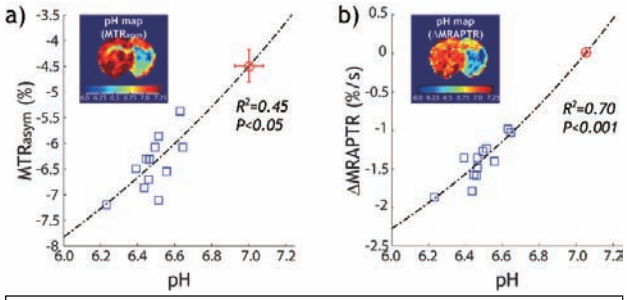



Figure 1, Calibration of pH-sensitive APT MRI indices toward absolute tissue pH. a) MTRasym vs. pH, and b) ΔMRAPTR vs. pH.

Fig. 2 shows perfusion, diffusion and pH images from a representative acute stroke rat. There was noticeable mismatch among perfusion (Fig. 2a), diffusion (Fig. 2b) and pH lesions (Fig. 2c). Whereas the diffusion lesion core showed the worst pH drop, the peri-infarct perfusion/diffusion lesion mismatch appears to have mild pH change. Fig. 2d shows perfusion/pH lesion mismatch (red, benign oligemia), pH/diffusion lesion mismatch (green, metabolic penumbra) and diffusion lesion (black, ischemic core), being 21±12%, 34±18% and 44±16% of the hypoperfusion lesion, respectively.

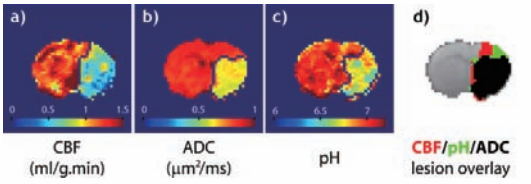



Figure 2, Multiparametric MRI of a representative stroke rat. a) Perfusion map. b) Diffusion map. c) pH map. d) Refined mismatch paradigm.

**DISCUSSION:** Our study calibrated pH-specific MRAPT MRI for mapping absolute tissue pH. Since the early work of Zhou et al., persistent progress has been achieved in CEST MRI quantification and optimization, yet in vivo tissue pH quantification has been challenging [4-6]. MRAPT pH mapping is of adequate pH specificity and sensitivity yet relatively straightforward to implement.

**CONCLUSION:** Non-invasive tissue pH mapping provides a metabolic imaging biomarker for the identification of heterogeneous ischemic tissue injury.

**ACKNOWLEDGMENTS:** This study was supported in part by grants from R01NS083654 and R21NS085574.

**REFERENCES:**

1. Guo et al. Neuroimage 141, 242-249 (2016). 2. Katsura et al. Eur. J. Neurosci. 4, 166-176 (1992). 3. Jokivarsi et al. MRM 57, 647-653 (2007). 4. Zhou et al. Nature medicine 9, 1085-1090 (2003). 5. Liu et al. NMR Biomed 26, 810-828 (2013). 6. Jones et al. JMRI 47, 11-27 (2018).

## Fat corrected APT-CEST in the human breast

Ferdinand Zimmermann[1], Andreas Korzowski[1], Patrick Schuenke[1], Johannes Breitling[1], Moritz Zaiss[2], Daniel Paech[1], Mark E. Ladd[1], Peter Bachert[1], and Steffen Goerke[1]
[1]*German Cancer Research Center (DKFZ), Heidelberg, Germany*
[2]*Max-Planck-Institute for Biological Cybernetics, Tübingen, Germany*

**INTRODUCTION:** CEST in the mammary gland is affected by lipid signals[1-5] not only causing strong pseudo rNOE artifacts[4], but also leading to an incorrect normalization of the Z-spectrum in the spectral region of the amide proton transfer (APT) signal. Here, we propose to approximate the total fat signal by the residual magnetization at Δω = 0 ppm. This enables the correction of Z-spectra for fat signal induced artifacts without any additional measurements and thus fat independent quantitative APT-CEST imaging.

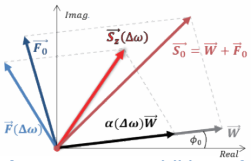



**Fig. 1:** Vector addition of lipid signals F and water W in the unsaturated ($S_0$,$F_0$ & W) and saturated ($S_z$, F & $\alpha$W) case.

**METHODS:** The total fat signal $\vec{F_0}$ contributing to the acquired fully relaxed image $\vec{S_0}$ can be formulated as a vector sum of multiple lipid resonances: $\vec{F_0} = \sum_m \vec{F_m}$ [Eq.1]. The conventional Z-normalization is given by: $Z_{conv.} = \frac{|\vec{S_z}(\Delta\omega)|}{|\vec{S_0}|} = \frac{|\alpha(\Delta\omega)\vec{W} + \sum_m \beta_m(\Delta\omega)\cdot\vec{F_m}|}{|\vec{W_0}+\vec{F_0}|}$ [Eq.2], where $\alpha, \beta$ describe the actual CEST effect on water $\vec{W}$ and saturation of lipid resonances, respectively (cf. Fig.1). This normalization leads to fat fraction and echo time (TE) dependent artifacts[2, 4]. Under the assumption of a total water signal saturation (i.e. $\alpha = 0$) without saturation of lipid resonances ($\beta_m = 1 \; \forall \; m$) one can estimate the collective fat signal at $\Delta\omega = 0\,ppm$ by: $\vec{S_z}(0\,ppm) = \vec{F_0}$ [Eq. 3]. Access to complex valued image data allows correction of offsets in the spectral region of the APT ($\beta_m = 1$): $Z_{corr.} = \frac{|\vec{S_z}(\Delta\omega) - \vec{S_z}(0\;ppm)|}{|\vec{S_0} - \vec{S_z}(0\;ppm)|} = \frac{|\vec{S_z}(\Delta\omega) - \vec{F_0}|}{|\vec{S_0} - \vec{F_0}|} = \alpha$ [Eq. 4] and thus enables obtaining the isolated CEST effect $\alpha$.

**Phantom experiment:** A 300 mM carnosine solution was topped with sunflower oil. A tilted imaging plane placed along the intersection created a fat fraction gradient[2]. Pre-saturation ($t_{sat}$ = 10s) was achieved by a train of Gaussian-shaped pulses ($t_p$ = 100 ms, DC 95%, $B_1$ = 0.6 & 0.8 µT). The experiment was repeated for various echo times: TE = {1.9, 2.04, 2.17, 2.43, 2.55, 2.65} ms. **In vivo measurement:** A 30y healthy woman was examined. Sat. parameters: $t_{sat}$ = 5.6 s, $t_p$ = 15 ms, DC = 80%, $TE_{in\text{-}phase}$ = 2.04 ms, $B_1$ = 0.6 & 0.9 µT. All experiments were performed on a 7T MR scanner (Siemens Magnetom) employing a bilateral breast coil (Rapid Biomedical). A Lorentzian function was fitted to the APT signal and AREX = $1/T_1 \cdot (1/Z_{lab} - 1/Z_{ref})$ was calculated[6] and corrected for $B_1$ inhomogeneities (reconstructed $B_1$ = 0.8 & 0.9 µT for phantom and in vivo measurement, respectively)[7].

**RESULTS & DISCUSSION:** Conventionally calculated Z-spectra (Eq. 2) show TE and fat fraction dependent artifacts at 0 ppm and in the NOE region[4,2] and a dispersion of the APT signal (Fig. 2A). The CEST contrast, $AREX_{APT}$, is strongly affected as well (Fig. 2C). After correction of Z-spectra (Eq.4), APT signals in Z-spectra overlay (Fig. 2B) and $AREX_{APT}$ does not correlate with TE and fat fraction. The correction method enables robust AREX quantification in the range of 0-50% fat fraction for arbitrary phase relations of water. Applied to a healthy volunteer, corrected $AREX_{APT}$ contrast appears more homogenous in the mammary gland of the healthy volunteer (Fig. 2E&F). This is to the extent of our knowledge the first APT-CEST contrast in the human breast at 7T corrected for fat signal contribution, spillover, $B_1$ field inhomogeneities and $T_1$ relaxation.

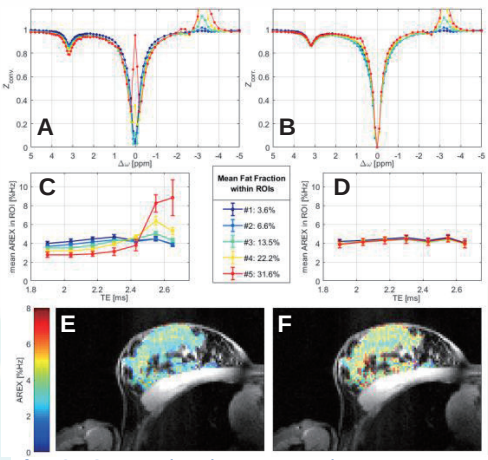



**Fig. 2:** Conventional Z-spectra ($TE_{opposed\text{-}phase}$ = 2.55 ms) of carnosine show a dispersion of the APT signal (A) and $AREX_{APT}$ is strongly dependent on TE and fat fraction (C). Z-spectra calculated by the proposed approach (Eq.4) overlay in the APT regime (B) and corresponding $AREX_{APT}$ is independent of TE and fat fraction (D). Applied to a healthy volunteer, the corrected APT contrast in the mammary gland (F) appears more homogenous compared to the uncorrected contrast (E).

**CONCLUSION:** The proposed method increases the specificity of APT-imaging in tissues with varying fat content without the need for any additional acquisitions and presents a SAR and time efficient alternative to fat saturation schemes and water-fat separation approaches.

**REFERENCES:** [1] Schmitt B, et al. Fortschr Röntgenstr 2011;183:1030–1036. [2] Zhang S, et al. Magn. Reson. Med. 2018;79:2731–2737. [3] Krikken E, et al. Breast Cancer Res. 2018:1–9. [4] Lu J, et al. Magn. Reson. Med. 2015;73(4):1615–1622. [5] Zhang S, et al. Magn. Reson. Med. 2018;80:895–903; [6] Zaiss M, et al. NMR Biomed 2014;27:240-52. [7] Windschuh J, et al., NMR Biomed 2015;28(5):529-537.



# The 7th International Workshop on Chemical Exchange Saturation Transfer Imaging

第七届化学交换饱和转移成像国际专题研讨会